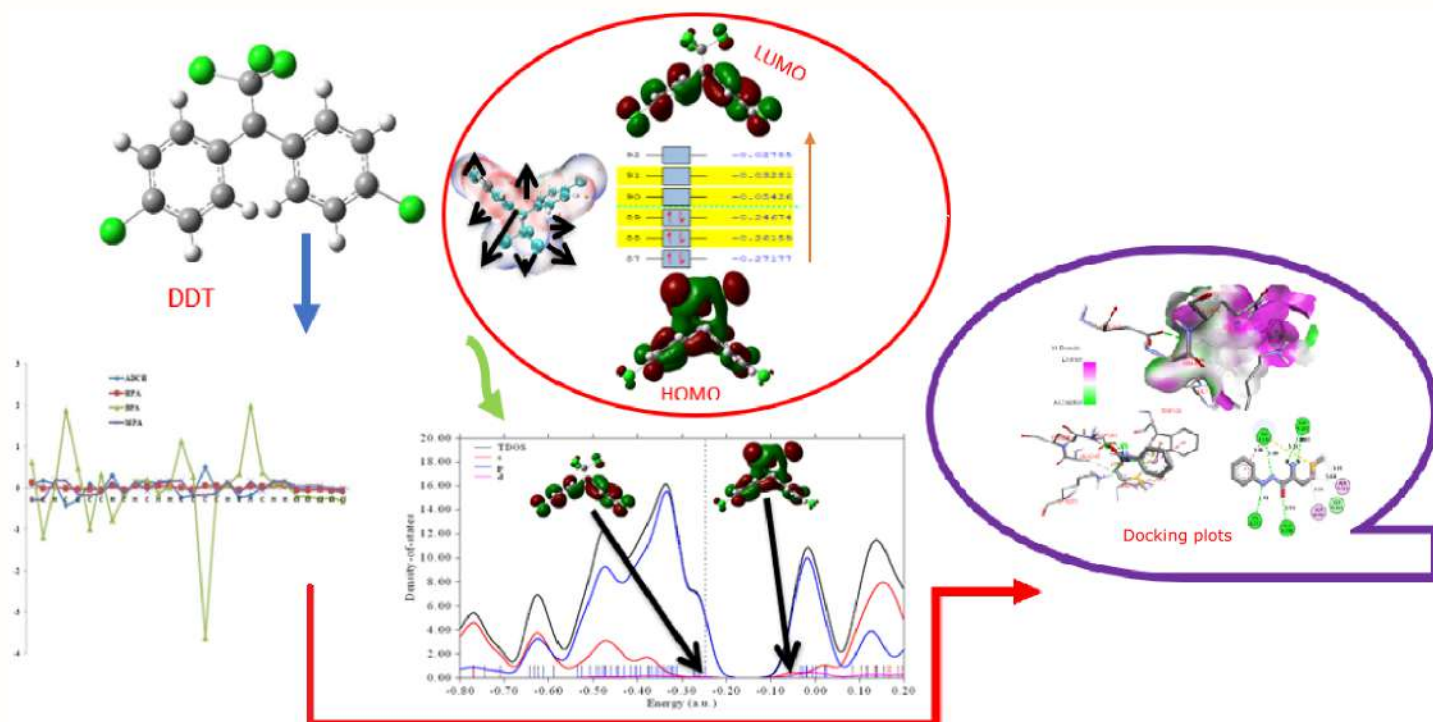


Eclética Química Journal

Volume 47 • number 3 • year 2022



Electrochemistry

Voltammetric glassy carbon sensor approach for the extended stability studies of doxorubicin in lyophilized dosage form

Molecular docking

Experimental, DFT study, and in silico molecular docking investigations of dichlorodiphenyltrichloroethane against human estrogen receptor alpha

Density functional

Influence of structural disorder on the photocatalytic properties of ZnS nanocrystals prepared by the one-pot solvothermal approach

Corrosion tests

On-site weld quality assessment and qualification for stainless steels tanks



UNIVERSIDADE ESTADUAL PAULISTA

Reitor

Pasqual Barretti

Vice-Reitora

Maysa Furlan

Pró-Reitora de Graduação

Celia Maria Giacheti

Pró-Reitora de Pós-Graduação

Maria Valnice Boldrin

Pró-Reitor de Pesquisa

Edson Cocchieri Botelho

Pró-Reitor de Extensão Universitária e Cultura

Raul Borges Guimarães

Pró-Reitor de Planejamento Estratégico e Gestão

Estevão Tomomitsu Kimpara



INSTITUTO DE QUÍMICA

Diretor

Sidney José Lima Ribeiro

Vice-Diretora

Denise Bevilaqua

Editorial Team

Editor-in-Chief

Prof. Assis Vicente Benedetti, São Paulo State University, Institute of Chemistry, Araraquara, Brazil

Editors

Prof. Antonio Eduardo Mauro, São Paulo State University, Institute of Chemistry, Araraquara, Brazil

Prof. Horacio Heinzen, University of the Republic, Faculty of Chemistry, Montevideo, Uruguay

Prof. Marcos Carlos de Mattos, Federal University of Ceará, Center of Sciences, Fortaleza, Brazil

Prof. Maria Célia Bertolini, São Paulo State University, Institute of Chemistry, Araraquara, Brazil

Prof. Patrícia Hatsue Suegama, Federal University of Grande Dourados, Faculty of Exact and Technological Sciences, Dourados, Brazil

Prof. Paulo Clairmont Feitosa Lima Gomes, São Paulo State University, Institute of Chemistry, Araraquara, Brazil

Editorial Board

Prof. Bayardo Baptista Torres, University of São Paulo, Institute of Chemistry, São Paulo, Brazil

Prof. Enric Brillas, University of Barcelona, Faculty of Chemistry, Barcelona, Spain

Prof. Francisco de Assis Leone, University of São Paulo, Faculty of Philosophy, Sciences and Literature, Ribeirão Preto, Brazil

Prof. Ivano Gerardt Rolf Gutz, University of São Paulo, Institute of Chemistry, São Paulo, Brazil

Prof. Jairton Dupont, Federal University of Rio Grande do Sul, Institute of Chemistry, Porto Alegre, Brazil

Prof. José Antônio Maia Rodrigues, University of Porto, Faculty of Sciences, Porto, Portugal

Prof. Lauro Kubota, University of Campinas, Institute of Chemistry, São Paulo, Brazil

Prof. Massuo Jorge Kato, University of São Paulo, Institute of Chemistry, São Paulo, Brazil

Prof. Roberto Santana da Silva, University of São Paulo, Faculty of Pharmaceutical Sciences, Ribeirão Preto, Brazil

Prof. Verónica Cortés de Zea Bermudez, University of Trás-os-Montes and Alto Douro, School of Life and Environmental Sciences, Vila Real, Portugal

EDITORIAL PRODUCTION

Ctrl K Produção Editorial – Araraquara, Brazil

digite@ctrlk.com.br

Editorial

The Eclética Química Journal's team proudly announces the third issue of vol. 47 of 2022nd year desiring to all a continue and fruitful scientific research. The first article focuses on the impact of the sulfur vacancies on the photocatalytic response of the ZnS nanocrystals synthesized by solvothermal method varying the concentration of the precursors zinc acetate and thiourea. The obtained products have hexagonal structure with different degrees of crystallinity and a comparison of experimental results and theoretical calculations revealed the formation of intermediate levels inside the bandgap due to structural polarization. The bandgap engineering has a significant impact on the photocatalytic response of these samples and the mechanism investigation confirmed the formation of the reactive oxygen species, usually responsible for methylene blue dye degradation. Sequentially, an electroanalytical method based on differential pulse voltammetry with glassy carbon electrode is described for analysis of doxorubicin (DOX), an anthracycline antibiotics widely used in the clinical treatment of cancer patients. It was performed the DOX stability after reconstitution and determined the correct time for safe administration to patients in hospitals, allowing application in the drug quality control with low-cost methodology and with similar results to those obtained using high-performance liquid chromatography analysis of pharmaceutical samples containing DOX. Follows an experimental and theoretical study of a pure commercial sample of dichlorodiphenyltrichloroethane (DDT) and its application for molecular docking against human estrogen receptor alpha is presented. The DDT molecule was experimentally characterized by means of FT-IR and GC-MS and the results compared to those obtained from theoretical molecular calculations. According to molecular docking investigation, the only interaction found in the complex after docking was steric interaction and the most reactive sites in the compound and its overall reactivity were identified. Closes this issue a case study of 2101 duplex stainless steel tank applying a portable electrochemical microcell system for *on-site* weld inspection and corrosion monitoring from the manufacturing until 12 months of operation. The double loop electrochemical potentiokinetic reactivation technique was used to evaluate the sensitization degree on the welded regions during the tank manufacturing and a passivation treatment was applied to improve the passivation level, confirmed by on-site cyclic polarization tests. After 12 months of operation the passivation level decreased, new passivation treatment was applied and evaluated. Final, an acceptance criterion to passivation level was proposed.

The Editor and members of Editorial Board of Eclética Química Journal want to thank the great effort developed by the Authors and Reviewers making possible this publication.

Assis Vicente Benedetti
Editor-in-Chief of EQJ

Citation databases: Eclética Quim. J. is indexed



*Click on the images to follow the links.

EBSCO has no link available. The address is for subscribers only.

INSTRUCTIONS FOR AUTHORS

BEFORE YOU SUBMIT

1. Check *Eclét. Quim. J.*'s focus and scope

Eclética Química Journal is a peer-reviewed quarterly publication of the Institute of Chemistry of São Paulo State University (UNESP). It publishes original researches as articles, reviews and short reviews in **all areas of Chemistry**.

2. Types of papers

- a. Original articles
- b. Reviews
- c. Short reviews
- d. Communications
- e. Technical notes
- f. Articles in education in chemistry and chemistry-related areas

Manuscripts submitted for publication as full articles and communications must contain original and unpublished results and should not have been submitted elsewhere either partially or whole.

a. Original articles

The manuscript must be organized in sections as follows:

1. Introduction
 2. Experimental
 3. Results and Discussion
 4. Conclusions
- References

Sections titles must be written in bold and sequentially numbered; only the first letter should be in uppercase letter. Subsections, numbered as exemplified, should be written in normal and italic letters; only the first letter should be in uppercase letter.

Example:

1. Introduction

1.1 History

2. Experimental

2.1 Surface characterization

2.1.1 Morphological analysis

b. Reviews

Review articles should be original and present state-of-the-art overviews in a coherent and concise form covering the

most relevant aspects of the topic that is being revised and indicate the likely future directions of the field. Therefore, before beginning the preparation of a Review manuscript, send a letter (one page maximum) to the Editor with the subject of interest and the main topics that would be covered in the Review manuscript. The Editor will communicate his decision in two weeks. Receiving this type of manuscript does not imply acceptance to be published in **Eclét. Quím. J.** It will be peer-reviewed.

c. Short reviews

Short reviews should present an overview of the state-of-the-art in a specific topic within the scope of the Journal and limited to 5,000 words. Consider a table or image as corresponding to 100 words. Before beginning the preparation of a Short Review manuscript, send a letter (one page maximum) to the Editor with the subject of interest and the main topics that would be covered in the Short Review manuscript.

d. Communications

Communications should cover relevant scientific results and are limited to 1,500 words or three pages of the Journal, not including the title, authors' names, figures, tables and references. However, Communications suggesting fragmentation of complete contributions are strongly discouraged by Editors.

e. Technical notes

Descriptions of methods, techniques, equipment or accessories developed in the authors' laboratory, as long as they present chemical content of interest. They should follow the usual form of presentation, according to the peculiarities of each work. They should have a maximum of 25 pages, including figures, tables, diagrams, etc.

f. Articles in education in chemistry and chemistry-correlated areas

Research manuscript related to undergraduate teaching in Chemistry and innovative experiences in undergraduate and graduate education. They should have a maximum of 25 pages, including figures, tables, diagrams, and other elements.

3. Special issues

Special issues with complete articles dedicated to Symposia and Congresses and to special themes or in honor of scientists with relevant contributions in Chemistry and correlate areas can be published by **Eclét. Quím. J.** under the condition that a previous agreement with Editors is established. All the guides of the journal must be followed by the authors.

4. Approval

Ensure all authors have seen and approved the final version of the article prior to submission. All authors must also approve the journal you are submitting to.

ETHICAL GUIDELINES

Before starting the submission process, please be sure that **all ethical aspects mentioned below were followed.** Violation of these ethical aspects may preclude authors from submitting or publishing articles in **Eclét. Quím. J.**

a. Coauthorship: The corresponding author is responsible for listing as coauthors only researchers who have really taken part in the work, for informing them about the entire manuscript content and for obtaining their permission to submit and publish it.

b. Nonauthors: Explicit permission of a nonauthor who has collaborated with personal communication or discussion to the manuscript being submitted to **Eclet. Quím. J.** must be obtained before being cited.

c. Unbiased research: Authors are responsible for carefully searching for all the scientific work relevant to their reasoning irrespective of whether they agree or not with the presented information.

d. Citation: Authors are responsible for correctly citing and crediting all data taken from other sources. This requirement is not necessary only when the information is a result of the research presented in the manuscript being submitted to **Eclet. Chem. J.**

e. Direct quotations: The word-for-word reproduction of data or sentences as long as placed between quotation marks and correctly cited is not considered ethical deviation when indispensable for the discussion of a specific set of data or a hypothesis.

f. Do not cite: Master's Degree dissertations and PhD theses are not accepted; instead, you must cite the publications resulted from them.

g. Plagiarism: Plagiarism, self-plagiarism, and the suggestion of novelty when the material was already published are unaccepted by **Eclet. Quím. J.** Before reviewing a manuscript, the **Turnitin antiplagiarism software** will be used to detect any ethical deviation.

h. Simultaneous submissions of the same manuscript to more than one journal is considered an ethical deviation and is conflicted to the declaration has been done below by the authors.

i. Studies with humans or other animals: Before submitting manuscripts involving human beings, materials from human or animals, the authors need to confirm that the procedures established, respectively, by the institutional committee on human experimentation and Helsinki's declaration, and the recommendations of the animal care institutional committee were followed. Editors may request complementary information on ethical aspects.

COPYRIGHT NOTICE

The corresponding author transfers the copyright of the submitted manuscript and all its versions to **Eclet. Quím. J.**, after having the consent of all authors, which ceases if the manuscript is rejected or withdrawn during the review process.

When a published manuscript in **Eclet. Quím. J.** is also published in other Journal, it will be immediately withdrawn from **Eclet. Quím. J.** and the authors informed of the Editor decision.

Self-archive to institutional, thematic repositories or personal webpage is permitted just after publication. The articles published by **Eclet. Quím. J.** are licensed under the [Creative Commons Attribution 4.0 International License](#).

PUBLICATION CHARGES

Eclética Química Journal is supported by the Institute of Chemistry/UNESP and publication is free of charge for authors.

MANUSCRIPT PREPARATION

COVER LETTER

We provide a template to help you prepare your cover letter. To download it, click [here](#).

The cover letter **MUST** include:

1. Identification of authors

- a. The authors' full names (they must be written in full and complete, separated by comma)

João M. José	Incorrect
J. M. José	Incorrect
João Maria José	Correct!

- b. E-mail addresses and affiliations (**neither more nor less than two instances**) of all authors;
- c. ORCID ID links;
- d. A plus sign (+) indicating the corresponding author.

Example:

Author Full Name¹⁺, Author Full Name²

1. University, Faculty or Institute, City, Country.
2. Company, Division or Sector or Laboratory, City, Country.

+ Author 1: address@mail.com, ORCID: <https://orcid.org/xxxx-xxxx-xxxx-xxxx>

Author 2: address@mail.com, ORCID: <https://orcid.org/xxxx-xxxx-xxxx-xxxx>

2. Authors' contribution

We request authors to include author contributions according to CRediT taxonomy standardized contribution descriptions. [CRediT \(Contributor Roles Taxonomy\)](#) is a high-level taxonomy, including 14 roles, that can be used to represent the roles typically played by contributors to scientific scholarly output. The roles describe each contributor's specific contribution to the scholarly output.

- a. Please, visit this link (<https://casrai.org/credit/>) to find out which role(s) the authors fit into;
- b. Do not modify the role names; do not write "all authors" in any role. Do not combine two or more roles in one line.**
- c. If there are any roles that no author has engaged in (such as funding in papers that were not funded), write "Not applicable" in front of the name of the role;
- d. Write the authors' names according to the [American Chemistry Society \(ACS\) citation style](#).

Example:

Conceptualization: Foster, J. C.; O'Reilly, R. K.

Data curation: Varlas, S.; Couturaud, B.; Coe, J.; O'Reilly, R. K.

Formal Analysis: Foster, J. C.; Varlas, S.

Funding acquisition: Not applicable.

Investigation: Foster, J. C.; O'Reilly, R. K.

Methodology: Coe, J.; O'Reilly, R. K.

Project administration: O'Reilly, R. K.

Resources: Coe, J.

Software: Not applicable.

Supervision: O'Reilly, R. K.

Validation: Varlas, S.; Couturaud, B.

Visualization: Foster, J. C.

Writing – original draft: Foster, J. C.; Varlas, S.; Couturaud, B.; Coe, J.; O'Reilly, R. K.

Writing – review & editing: Foster, J. C.; Varlas, S.; Couturaud, B.; Coe, J.; O'Reilly, R. K.

4. Indication of reviewers

We kindly ask the authors to suggest **five** suitable reviewers, providing full name, affiliation, and email.

5. Other information

- a. The authors must write one paragraph remarking the novelty and relevance of the work;
- b. The corresponding author must declare, on behalf of the other authors, that the manuscript being submitted is original and its content has not been published previously and is not under consideration for publication elsewhere;
- c. The authors must inform if there is any conflict of interest.

6. Acknowledgements and funding

Acknowledgements and funding information will be requested after the article is accepted for publication.

7. Data availability statement

A data availability statement informs the reader where the data associated with your published work is available, and under what conditions they can be accessed. Therefore, authors must inform if:

Data will be available upon request;

All dataset were generated or analyzed in the current study; or

Data sharing is not applicable.

MANUSCRIPT

We provide a template to help you prepare your manuscript. To download it, click [here](#).

1. General rules

Only manuscripts written in English will be accepted. British or American usage is acceptable, but they should not be mixed. Non-native English speakers are encouraged to have their manuscripts professionally revised before submission.

Manuscripts must be sent in editable files as *.doc, *.docx or *.odt. The text must be typed using font style Times New Roman and size 12. Space between lines should be 1.5 mm and paper size A4, top and bottom margins 2.5 cm, left and right margins 2.0 cm.

All contributions must include an **abstract** (170 words maximum), **three to five keywords** and a **graphical abstract** (8 cm wide × 8 cm high).

Supplementary information: all type of articles accepts supplementary information (SI) that aims at complementing

the main text with material that, for any reason, cannot be included in the article.

TITLE

The title should be concise, explanatory and represent the content of the work. The title must have only the first letter of the sentence in uppercase. The following are not allowed: acronyms, abbreviations, geographical location of the research, en or em dashes (which must be replaced by a colon). Titles do not have full point.

ABSTRACT

Abstract is the summary of the article. The abstract must be written as a running text not as structured topics, but its content should present background, objectives, methods, results, and conclusion. It cannot contain citations. The text should be written in a single paragraph with a **maximum of 170 words**.

KEYWORDS

Keywords are intended to make it easier for readers to find the content of your text. As fundamental tools for database indexing, they act as a gateway to the text. The correct selection of keywords significantly increases the chances that a document will be found by researchers on the topic, and consequently helps to promote the visibility of an article within a myriad of publications.

FIGURES, TABLES AND EQUATIONS

Figures, tables and equations must be written with initial capital letter followed by their respective number and period, in bold, without adding zero “**Table 1**”, preceding an explanatory title. Tables, Figures and Equations should appear after the first citation and should be numbered according to the ascending order of appearance in the text (1, 2, 3...).

Figures, tables, schemes and photographs already published by the same or different authors in other publications may be reproduced in manuscripts of **Eclet. Quim. J.** only with permission from the editor house that holds the copyright.

Nomenclature, abbreviations, and symbols should follow IUPAC recommendations.

DATA AVAILABILITY STATEMENT

The data availability statement informs the reader where the data associated with your work is available, and under what conditions they can be accessed. They also include links (where applicable) to the data set.

- a. The data are available in a data repository (cite repository and the DOI of the deposited data);
- b. The data will be available upon request;
- c. All data sets were generated or analyzed in the current study;
- d. Data sharing is not applicable (in cases where no data sets have been generated or analyzed during the current study, it should be declared).

GRAPHICAL ABSTRACT

The graphical abstract must summarize the manuscript in an interesting way to catch the attention of the readers. As already stated, it must be designed with 8 cm wide × 8 cm high, and a 900-dpi resolution is mandatory for this journal. It must be submitted as *.jpg, *.jpeg, *.tif or *.ppt files as supplementary file.

We provide a template to help you prepare your GA. To download it, click [here](#).

SUPPLEMENTARY INFORMATION

When appropriate, important data to complement and a better comprehension of the article can be submitted as Supplementary File, which will be published online and will be made available as links in the original article. This might include additional figures, tables, text, equations, videos or other materials that are necessary to fully document the research contained in the paper or to facilitate the readers' ability to understand the work.

Supplementary material should be presented in appropriate .docx file for text, tables, figures and graphics. All supplementary figures, tables and videos should be referred in the manuscript body as "Table S1, S2...", "Fig. S1, S2..." and "Video S1, S2 ...".

At the end of the main text the authors must inform: This article has supplementary information.

Supplementary information will be located following the article with a different DOI number from that of the article, but easily related to it.

CITATION STYLE GUIDE

From 2021 on, the **Eclet. Quim. J.** will follow the [ACS citation style](#).

Indication of the sources is made by authorship and date. So, the reference list is organized alphabetically by author.

Each citation consists of two parts: the in-text citation, which provides brief identifying information within the text, and the reference list, a list of sources that provides full bibliographic information.

We encourage the citation of primary research over review articles, where appropriate, in order to give credit to those who first reported a finding. Find out more about our commitments to the principles of [San Francisco Declaration on Research Assessment \(DORA\)](#).

What information you must cite?

- a. Exact wording taken from any source, including freely available websites;
- b. Paraphrases of passages;
- c. Summaries of another person's work;
- d. Indebtedness to another person for an idea;
- e. Use of another researchers' work;
- f. Use of your own previous work.

You do not need to cite **common knowledge**.

Example:

Water is a tasteless and odorless liquid at room temperature (common knowledge, no citation needed)

In-text citations

You can choose to cite your references within or at the end of the phrase, as showed below.

Within the cited information:

One author: Finnegan states that the primary structure of this enzyme has also been determined (2004).

Two authors: Finnegan and Roman state that the structure of this enzyme has also been determined (2004).

Three or more authors: Finnegan *et al.* state that the structure of this enzyme has also been determined (2004).

At the end of the cited information:

One author: The primary structure of this enzyme has also been determined (Finnegan, 2004).

Two authors: The primary structure of this enzyme has also been determined (Finnegan and Roman, 2004).

Three or more authors: The primary structure of this enzyme has also been determined (Finnegan *et al.*, 2004).

If you need to cite more than one reference in the same brackets, separate them with semicolon and write them in alphabetic order:

The primary structure of this enzyme was determined (Abel *et al.*, 2011; Borges, 2004; Castro *et al.*, 2021).

Bibliographic references

Article from scientific journals

Foster, J. C.; Varlas, S.; Couturaud, B.; Coe, J.; O'Reilly, R. K. Getting into Shape: Reflections on a New Generation of Cylindrical Nanostructures' Self-Assembly Using Polymer Building Block. *J. Am. Chem. Soc.* **2019**, *141* (7), 2742–2753. <https://doi/10.1021/jacs.8b08648>

Book

Hammond, C. *The Basics of Crystallography and Diffraction*, 4th ed.; International Union of Crystallography Texts on Crystallography, Vol. 21; Oxford University Press, 2015.

Book chapter

Hammond, C. Crystal Symmetry. In *The Basics of Crystallography and Diffraction*, 4th ed.; International Union of Crystallography Texts on Crystallography, Vol. 21; Oxford University Press, 2015; pp 99–134.

Book with editors

Mom the Chemistry Professor: Personal Accounts and Advice from Chemistry Professors Who Are Mothers, 2nd ed.; Woznack, K., Charlebois, A., Cole, R. S., Marzabadi, C. H., Webster, G., Eds.; Springer, 2018.

Website

ACS Publications Home Page. <https://pubs.acs.org/> (accessed 2019-02-21).

Document from a website

American Chemical Society, Committee on Chemical Safety, Task Force for Safety Education Guidelines. *Guidelines for Chemical Laboratory Safety in Academic Institutions*. American Chemical Society, 2016. <https://www.acs.org/content/dam/acsorg/about/governance/committees/chemicalsafety/publications/acs-safety-guidelines-academic.pdf> (accessed 2019-02-21).

Conference proceedings

Nilsson, A.; Petersson, F.; Persson, H. W.; Jönsson, H. Manipulation of Suspended Particles in a Laminar Flow. In *Micro Total Analysis Systems 2002, Proceedings of the μ TAS 2002 Symposium*, Nara, Japan, November 3–7, 2002; The Netherlands, 2002; pp 751–753. https://doi.org/10.1007/978-94-010-0504-3_50

Governmental and legislation information

Department of Commerce, United States Patent and Trademark Office. Section 706.02 Rejection of Prior Art [R-

07.2015]. *Manual of Patent Examining Procedure (MPEP)*, 9th ed., rev. 08.2017, last revised January 2018. <https://www.uspto.gov/web/offices/pac/mpep/s706.html#d0e58220> (accessed 2019-03-20).

Patent

Lois-Caballe, C.; Baltimore, D.; Qin, X.-F. Method for Expression of Small RNA Molecules within a Cell. US 7 732 193 B2, 2010.

Streaming data

American Chemical Society. Game of Thrones Science: Sword Making and Valyrian Steel. *Reactions*. YouTube, April 15, 2015. <https://www.youtube.com/watch?v=CHRCGoje4j4> (accessed 2019-02-28).

For more information, you can access the [ACS Style Quick Guide](#) and the [Williams College LibGuides](#).

SUBMITTING YOUR MANUSCRIPT

The corresponding author should submit the manuscript online by clicking [here](#). If you are a user, register by clicking [here](#).

At the **User home** page, click in **New submission**.

In Step 1, select a section for your manuscript, verify one more time if you followed all these rules in **Submission checklist**, add Comments for the Editor if you want to, and click Save and continue.

In Step 2, you will **upload your manuscript**. Remember it will pass through a double-blind review process. So, do not provide any information on the authorship.

In Step 3, enter **submission's metadata**: authors' full names, valid e-mail addresses and ORCID ID links (with "http" not "https"). Add title, abstract, contributors and supporting agencies, and the list of references.

In Step 4, upload the **cover letter**, the **graphical abstract** and other **supplementary material** you want to include in your manuscript.

In Step 5, you will be able to check all submitted documents in the **File summary**. If you are certain that you have followed all the rules until here, click in **Finish submission**.

REVIEW PROCESS

The time elapsed between the submission and the first response of the reviewers is around three months. The average time elapsed between submission and publication is around seven months.

Resubmission (manuscripts "rejected in the present form" or subjected to "revision") must contain a letter with the responses to the comments/criticism and suggestions of reviewers/editors should accompany the revised manuscript. All modifications made to the original manuscript must be highlighted.

If you want to check our Editorial process, click [here](#).

EDITOR'S REQUIREMENTS

Authors who have a manuscript accepted in **Eclet. Quim. J.** may be invited to act as reviewers.

Only the authors are responsible for the correctness of all information, data and content of the manuscript submitted to **Eclet. Quim. J.** Thus, the Editors and the Editorial Board cannot accept responsibility for the correctness of the material published in **Eclet. Quim. J.**

Proofs

After accepting the manuscript, **Eclet. Quim. J.** technical assistants will contact you regarding your manuscript page proofs to correct printing errors only, i.e., other corrections or content improvement are not permitted. The proofs shall be returned in three working days (72 h) via email.

Appeal

Authors may only appeal once about the decision regarding a manuscript. To appeal against the Editorial decision on your manuscript, the corresponding author can send a rebuttal letter to the editor, including a detailed response to any comments made by the reviewers/editor. The editor will consider the rebuttal letter, and if deemed appropriate, the manuscript will be sent to a new reviewer. The Editor decision is final.

Contact

If you have any question, please contact our team:

Prof. Assis Vicente Benedetti
Editor-in-Chief
ecletica.iq@unesp.br

Letícia Amanda Miguel and Jéssica Odoni
Technical support
ecletica@ctrlk.com.br

SUMMARY

EDITORIAL BOARD.....	3
EDITORIAL.....	4
DATABASE.....	5
INSTRUCTIONS FOR AUTHORS	6

ORIGINAL ARTICLES

Influence of structural disorder on the photocatalytic properties of ZnS nanocrystals prepared by the one-pot solvothermal approach 17
Victoria Gabriela Benatto, Guilherme da Silva Lopes Fabris, Julio Ricardo Sambrano, Carlton Anthony Taft, Felipe de Almeida La Porta

Voltammetric glassy carbon sensor approach for the extended stability studies of doxorubicin in lyophilized dosage form 32
Carlos Eduardo Peixoto Cunha, Edson Silvio Batista Rodrigues, Jerônimo Raimundo de Oliveira Neto, Vernon Somerset, Stephânia Taveira, Lívia Flório Sgobbi, Eric de Souza Gil

Experimental, DFT study, and *in silico* molecular docking investigations of dichlorodiphenyltrichloroethane against human estrogen receptor alpha..... 39
Tabé Ntui Ntui, Vincent Ndem Osabor, Peter Amba Neji, Michael Akomaye Akpe, John Akwagiobe Agwupuye, Stephen Adie Adalikwu, Terkumbur Emmanuel Gber, Bitrus Hyelavalada Andrew, Uduak Ugbaja

TECHNICAL NOTE

On-site weld quality assessment and qualification for stainless steels tanks..... 55
Luis Henrique Guilherme, Cecilio Sadao Fugivara, Assis Vicente Benedetti

Influence of structural disorder on the photocatalytic properties of ZnS nanocrystals prepared by the one-pot solvothermal approach

Victoria Gabriela Benatto¹, Guilherme da Silva Lopes Fabris^{2,3}, Julio Ricardo Sambrano³, Carlton Anthony Taft⁴, Felipe de Almeida La Porta^{1,5+}

1. Federal University of Technology of Paraná, Laboratory of Nanotechnology and Computational Chemistry, Londrina, Brazil.
2. Federal University of Rio Grande do Norte, Department of Materials Engineering, Natal, Brazil.
3. São Paulo State University, Modeling and Molecular Simulation Group, Bauru, Brazil.
4. Brazilian Center of Physical Research, Rio de Janeiro, Brazil.
5. State University of Londrina, Post-Graduation Program in Chemistry, Londrina, Brazil.

+Corresponding author: Felipe de Almeida La Porta, **Phone:** +55 43 33159437, **Email address:** felipelaporta@utfpr.edu.br

ARTICLE INFO

Article history:

Received: October 04, 2021

Accepted: April 10, 2022

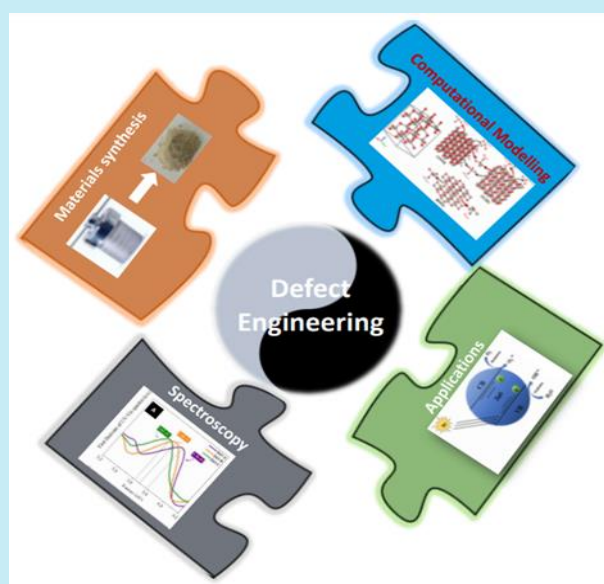
Published: July 01, 2022

Section Editor: Assis Vicente Benedetti

Keywords

1. ZnS
2. density functional theory
3. solvothermal processing
4. photocatalysis properties
5. electronic structure

ABSTRACT: This study focuses on the impact of the sulfur vacancies on the photocatalytic response of the ZnS nanocrystals synthesized by solvothermal method varying the concentration of zinc acetate/thiourea precursors. XRD patterns show that these samples have a hexagonal structure with different degrees of crystallinity, varying the crystallite size from 2.48 to 2.85 nm. The UV-Vis data reveals an absorption peak (at about 320 nm) characteristic of ZnS nanocrystals. As a result, a decrease in the bandgap value of these materials was observed from 3.78 to 3.62 eV. In principle, a comparison of these results and theoretical calculations reveals the formation of intermediate levels inside the bandgap due to structural polarization. These findings also corroborate the zeta potential measured for these samples, evidenced by an increase of positive charge of ZnS surfaces. Also, the low Miller-index surfaces, such as (10 $\bar{1}$ 0), (11 $\bar{2}$ 0) and (0001), were investigated by periodic density functional theory calculations, in nice agreement with the experimental data. A photocatalysis mechanism was investigated and confirmed the formation of reactive oxygen species.



1. Introduction

In recent years, the contamination of water by micropollutants, especially organic dyes, has become a matter of serious environmental concern (Ayodhya and Veerabhadram, 2018; Bilal *et al.*, 2019; Byrne *et al.*, 2018). Additionally, recent studies have also shown a troubling detection of the novel coronavirus (denoted as SARS-CoV-2) in feces and sewage, raising the hypothesis of fecal-oral transmission (Heller *et al.*, 2020). To catalyze the decomposition reactions of these organic pollutants and pathogens, a wide variety of novel nanoscale semiconductor materials has attracted particular interest, because of their high photocatalytic efficiency in converting pollutants into environmentally friendly byproducts (Amorin *et al.*, 2019; Ayala-Durán *et al.*, 2020).

Among the materials proposed for this purpose, the zinc sulfide (ZnS) semiconductor materials have a wide bandgap of about 3.6 eV and exhibit highly tunable chemical and physical properties as well as unique functionalities for a huge variety of emerging technologies (Chen *et al.*, 2010; Hussain *et al.*, 2017; Ippen *et al.*, 2014; Jellison *et al.*, 1986; La Porta *et al.*, 2014a; Lee and Wu, 2017; Lin *et al.*, 2019; Sultana *et al.*, 2018; Xiao *et al.*, 2016; Zhang *et al.*, 2013; Ziegler *et al.*, 2008). A notable example of ZnS-related applications includes light-emitting diodes (LEDs), lasers, sensors, solar cells, piezoelectric nanogenerator, (photo)catalysis, and biomedical applications (Hussain *et al.*, 2017; Ippen *et al.*, 2014; Jellison *et al.*, 1986; La Porta *et al.*, 2014a; Lee and Wu, 2017; Lin *et al.*, 2019; Sultana *et al.*, 2018; X. Wang, *et al.*, 2011; Xiao *et al.*, 2016; Zhang *et al.*, 2013; Ziegler *et al.*, 2008). Furthermore, more recently, the ZnS-based heterostructure have been widely studied, mainly due to high quality of ZnS shell (in core/shell structures with a lower bandgap core) that contributes to an increase in the efficiency and stability of optoelectronic devices based on ZnS heterostructures (Chen *et al.*, 2021; Mukherjee and Selvaraj, 2021; Talapin *et al.*, 2004; P. Wang *et al.*, 2021).

Likely, due to their outstanding chemical and physical properties and incredible versatility, such nanocrystals have enormous importance in academic and industrial scenery. For this reason, several methodologies have been widely developed in the last decades for their simple and straightforward manufacture of ZnS-related materials with desired particle sizes, structures, compositions, and morphologies (Hussain *et al.*, 2017; Jellison *et al.*, 1986; Lee and Wu, 2017; Sultana *et al.*, 2018; X. Wang *et al.*, 2011; Xiao *et al.*, 2016; Zhang *et al.*, 2013).

Nonetheless, among solution-based synthetic routes, it is known that the solvothermal approach is a relatively low-cost method and is widely used to produce diverse crystalline materials of high purity (La Porta *et al.*, 2014a; Li *et al.*, 2015; Santana *et al.*, 2011). Varela and coauthors have optimized the kinetics of solid-state reactions from hours to minutes, leading to obtaining spherical ZnS nanocrystals with controlled phase based on this strategy coupled with the use of microwave energy (La Porta *et al.*, 2013a; 2014a; b) Their work enabled a deep understanding of these ZnS crystals from a modern perspective based on the combination of theory, computational simulations, and experimental results aiming to elucidate these new nanoscale materials' physical and chemical behavior.

Therefore, this study is focused on the effects of structural defects caused by decreased concentration of zinc acetate/thiourea precursors in the solvothermal growth of ZnS nanocrystals with hexagonal structures for enhanced photocatalysis applications. Also, this study can significantly contribute to provide new chemical insights towards materials design with highly tailoring properties.

2. Experimental

2.1 Materials and synthesis

The ZnS nanocrystals with the hexagonal structure used in this study were synthesized from a one-pot solvothermal strategy based on a modification of the protocol established by Varela and collaborators (La Porta *et al.*, 2014a). Briefly, different concentrations of 1:1 zinc acetate/thiourea precursors system (such as 7.34 mmol for sample A, 3.68 mmol for sample B, or 1.835 mmol for sample C) were dissolved in approximately 50 mL of ethylene glycol. Then, 16 mmol of tetrabutylammonium hydroxide (40% wt/v) were added quickly and after 10 min the resulting reaction mixture was transferred into a Teflon-lined stainless-steel autoclave, properly sealed and then placed inside a muffle furnace for one-pot solvothermal synthesis at 160 °C for 120 min. After this period, the solvothermal system was slowly cooled and samples were collected near room temperature. Then, the precipitated powder was rinsed with deionized water/isopropanol several times in sequence and extracted by centrifugation, followed by room temperature drying for 24 h.

2.2 Characterization

The ZnS nanoparticles obtained were structurally characterized by X-ray diffraction (XRD) using a Bruker-D2 PHASER with Cu K α radiation ($\lambda = 1.5406$ Å) in the 2θ range from 20 to 80° at 0.02° s⁻¹. For better reading and identification, the ZnS samples at the three different concentrations were named as A (7.34 mmol of zinc acetate/thiourea), B (3.67 mmol of zinc acetate/thiourea), and C (1.835 mmol zinc acetate/thiourea). Then, the UV-Vis spectra were recorded using a S60 Libra spectrophotometer (Biochrom), with a range of 190–1100 nm, using a quartz cuvette with a 10-mm optical path and two polished windows. Dynamic light scattering (DLS) analysis was performed using a Litesizer 500 particle size analyzer (ANTON PAAR), with 658 nm laser wavelength, using a 12.5 × 15.5 × 45 mm quartz cuvette. For these measurements, the powders (about 0.0005 g) were dispersed in 1 mL of water.

2.3 Photocatalytic degradation

The photocatalytic activity of spherical ZnS nanocrystals was evaluated in this study for the degraded methylene blue (MB) dye solution under ultraviolet C (UVC) lamps (15 W, G15T8/OF, OSRAM) at 254 nm irradiation. In a typical procedure, about 10 mg of the as-prepared catalyst was dispersed in 14 mL of 10 mg L⁻¹ MB. In each test, the solution was continuously stirred for about of 20 min in the dark at room temperature (25 °C) in order to establish an adsorption-desorption equilibrium (Amorin *et al.*, 2019; Suzuki *et al.*, 2019a; 2021). During UVC irradiation, 1 mL of the solution was collected with an interval of 120 min. These MB dye solutions collected during degradation tests and then were analyzed at room temperature by a UV-Vis spectrometer (Biochrom).

2.4 Scavenger test

About 10 mg of catalyst in 14 mL of MB solution (10 mg L⁻¹) in the presence or not of different radical scavengers (in about 1 mmol), such as isopropanol (ISO), AgNO₃ (Ag), ammonium oxalate (AO), and pbenzoquinone (p-BQ), were added to the MB solution containing the photocatalyst (Pereira *et al.*, 2018; Suzuki *et al.*, 2021; Zhang *et al.*, 2012) and were mixed at a stirring rate of 300 rpm in the dark for 20 min. Later, the mixture was placed in the ultraviolet (UV) reactor at the same agitation rate. A 1 mL aliquot of the solution was collected after 120 min. The UV-Vis absorption

spectra of the supernatant liquid were recorded using the same equipment as the previous experiment.

2.5 Computational simulation

The computational density functional theory (DFT) simulations were performed for the bulk ZnS and the (10 $\bar{1}$ 0), (11 $\bar{2}$ 0) and (0001) surfaces under periodic conditions as implemented in the CRYSTAL17 package (Dovesi *et al.*, 2017). Here, both the Zn and S atomic centers were described using the Triple-zeta Plus Polarization (TZVP) basis set, together with the B3LYP-D3 functional (Zhang *et al.*, 2012). The convergence criteria were controlled by a set of five thresholds (10-8, 10-8, 10-8, 10-8, 10-16) and for both Pack–Monkhorst and Gilat shrinking factor of 8. Also, tolerances were set to 0.0001 Hartree/bohr and 0.0004 bohr, respectively, to check on the gradient components as well as nuclear displacements (Dovesi *et al.*, 2017).

The surfaces with lower Miller index: (10 $\bar{1}$ 0), (11 $\bar{2}$ 0) and (0001) were simulated taking into account the stoichiometry/symmetry condition. Here, the surface energy (E_{surf}) was calculated as showed in Eq. 1:

$$E_{surf} = \frac{(E_{slab} - n \times E_{bulk})}{2} \quad (1)$$

where E_{slab} represent the total energy per unit cell of the slab in the (hkl) direction, E_{bulk} is defined as the total energy of the bulk per molecular unit, n is the number of surface layers and A is defined as the surface unit cell area (Dovesi *et al.*, 2017). In this case, the surfaces presented convergence in slab models from 8, 10 and 12 molecular units for the (10 $\bar{1}$ 0), (11 $\bar{2}$ 0) and (0001), respectively.

3. Results and discussion

As is well-known, the single-crystalline ZnS nanocrystals are usually required for many of their technological applications. Therefore, with that in mind, based on the solvothermal protocols developed by Varela and coauthors (La Porta *et al.*, 2013b; 2014a), this study has modified them to obtain single-crystalline ZnS spheric nanoparticles from the alteration of (zinc acetate/thiourea) precursor concentrations. Thus, the authors of this work have found that the variations in the (zinc acetate/thiourea) precursor concentrations lead to a different coloration for the prepared ZnS nanopowders, as shown in Fig. 1e–g. This important visual aspect reveals that this approach may, in

principle, indicate a possible increase in defects in the material, usually seen as a white/yellow colored powder and its darkening is likely due to the formation of sulfur vacancies in the ZnS prepared samples, which it can usually occur in three different load states (i.e., V_S^x , V_S^+ and V_S^{++}), and these cannot be distinguished. Hence, the darkening of the powder color indicates an increase in the density of sulfur vacancies, according to the decrease in the amount of precursor, which in turn can influence the photocatalytic properties of such materials significantly. In order to confirm these hypotheses, a structural analysis of these samples was performed. From the XRD pattern shown in Fig. 1a, it can be observed that ZnS crystals has a hexagonal structure (belongs to space group P63mc) as well as a high degree

of crystallinity at the long-range (JCPDS #36–1450). No characteristic impurity peaks were observed in XRD data. Hence, this suggests that the products obtained have high purity. These results are in nice agreement with the work of Varela and coauthors (La Porta *et al.*, 2013b; 2014a). Figure 1b–d shows the average grain size and dispersion of sizes for these ZnS polycrystals which were determined from the XRD patterns. In particular, it can be assumed that these samples have a spherical crystallite as a model to XRD calculation of the grain size distribution, which is therefore based on using of a lognormal function. As a general result, these analyses suggest that such obtained powders have nanometric sizes.

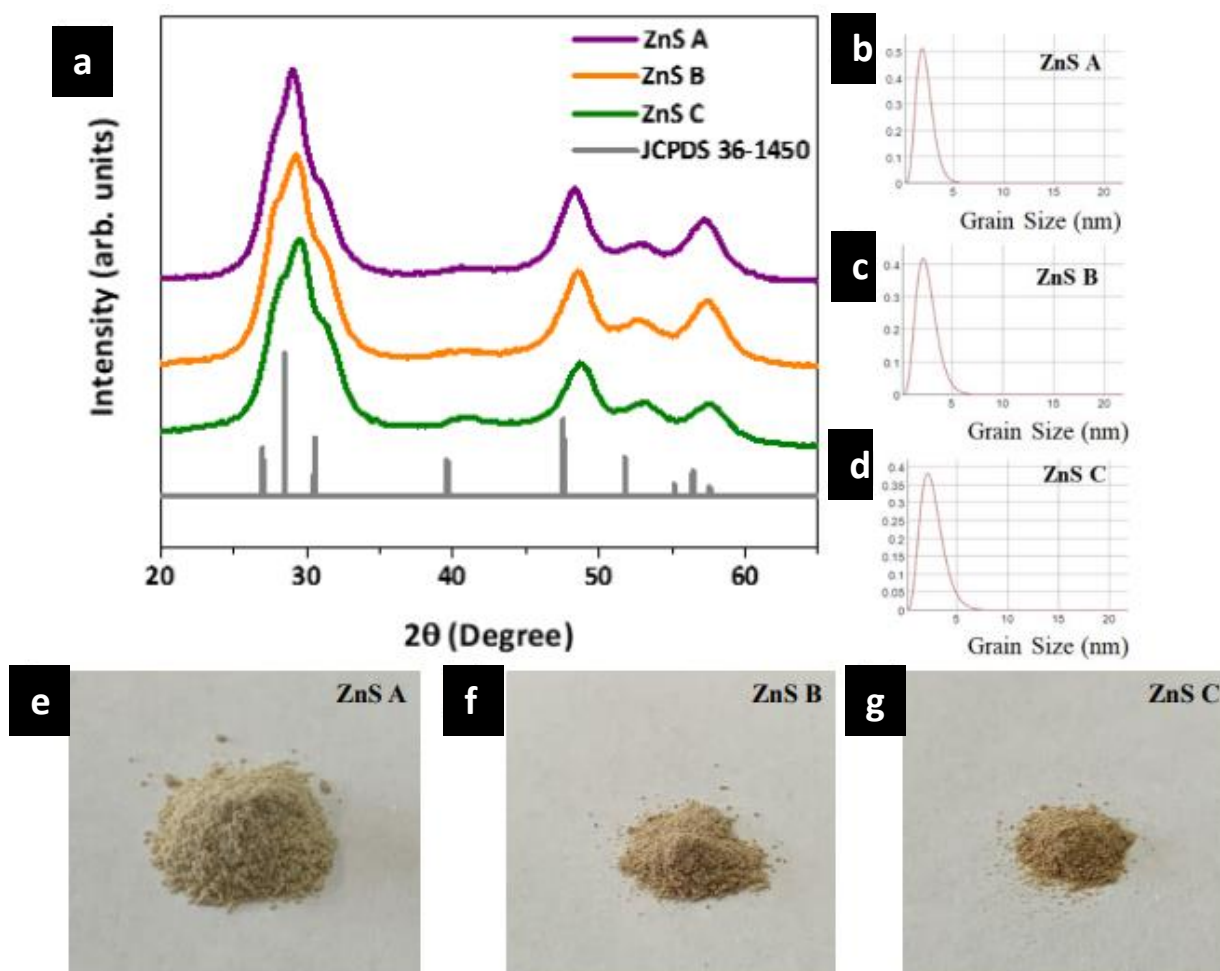


Figure 1. The XRD patterns, grain size distribution and digital photograph of powders. (a) XRD patterns of spheric ZnS nanoparticles; (b–d) Grain size distribution of ZnS samples, with grain sizes of about 2.6 nm, 3.1 nm, and 3.3 nm, for A, B and C samples; (e–g) Digital photograph of as-prepared ZnS nanopowders prepared using different (zinc acetate/thiourea) precursor concentrations in solvothermal conditions.

Moreover, another important aspect pertaining to the XRD peaks, as shown in Fig. 1a, reveals a significant

widening due to the very small crystallite size, as well as a certain degree of amorphization of the samples may

indicate. Thus, from this perspective, the degree of crystallinity was determined for these prepared samples in this study (Tab. 1).

Table 1. Lattice parameters (a , b and c , in Å), crystallite size (nm), crystallinity (%), microstrain, theoretical band, gap energy (E_{gap} , in eV) and surface energy (E_{surf} , in J m^{-2}). For the $(10\bar{1}0)$, $(11\bar{2}0)$ and (0001) the c parameters are described by the thickness of the surface.

ZnS A						
Crystallite Size (nm)		Crystallinity (%)		Microstrain (ϵ)		
2.85		90.1		0.030		
Lattice parameters						
Plane	d_{hkl}	a	c	Unit cell volume (Å ³)		
(100)	3.2786	3.7858	6.5571	93.9768		
(002)	3.0686	3.5433	6.1371	77.0524		
(101)	2.8832	3.3292	5.7663	63.9129		
ZnS B						
Crystallite Size (nm)		Crystallinity (%)		Microstrain (ϵ)		
2.72		86.2		0.031		
Lattice parameters						
Plane	d_{hkl}	a	c	Unit cell volume (Å ³)		
(100)	3.2786	3.7858	6.5571	93.9768		
(002)	3.0538	3.5263	6.1077	75.9460		
(101)	2.8832	3.3292	5.7664	63.9129		
ZnS C						
Crystallite Size (nm)		Crystallinity (%)		Microstrain (ϵ)		
2.48		83.2		0.034		
Lattice parameters						
Plane	d_{hkl}	a	c	Unit cell volume (Å ³)		
(100)	3.2786	3.7858	6.5571	93.9768		
(002)	3.0408	3.5113	6.0817	74.9805		
(101)	2.8588	3.3010	5.7176	62.3035		
Models	DFT					
	a	b	c	E_{gap}	E_{surf}	
	Bulk	3.77	3.77	6.14	4.01	-
	$(10\bar{1}0)$	3.77	6.15	17.78	3.88	1.07
	$(11\bar{2}0)$	6.14	6.53	21.04	4.13	1.10
(0001)	3.77	3.77	8.87	4.47	1.61	

However, based on the XRD data for a more accurate structural analysis we performed the peak deconvolution according to JCPDS #36–1450. Therefore, nine peaks are evident in the XRD pattern and were then deconvolution using a Voigt function, as shown in Fig. 2a–c. After deconvolution of the XRD peaks, these results were analyzed and used to calculate the crystallite size, microstrain, interplanar distance, and lattice parameters for all prepared samples are summarized in Tab. 1. Here, the crystallite size for these samples as prepared was estimated by two methods. First, using the deconvoluted XRD peaks, the average

crystallite size (T) was calculated by the Scherrer method (Eq. 2).

$$T = \frac{0.9\lambda}{\beta \cos\theta} \quad (2)$$

where λ is defined as Cu K α radiation; θ is defined as Bragg diffraction angle, and β is defined as peak width at half the maximum (FWHM) in radians (Guinier *et al.*, 1964). In this case, as the particles of ZnS have a spherical form the value of Scherrer constant is 0.9. Second, both the average strain and crystalline size of all prepared samples were then calculated using the

Williamson–Hall method (Eq. 3) (Suryanarayana, 1998). That is:

$$\frac{\beta \cos \theta}{\lambda} = \frac{0.9}{T} + \frac{4\varepsilon \sin \theta}{\lambda} \quad (3)$$

Here, FWHM can be expressed in terms of deformation (ε) which is determined by the slope of the straight line, and, in this case, T is determined by the intersection with the vertical axis, and the other parameters have the same meaning as in the Eq. 2 (Guinier *et al.*, 1964; La Porta *et al.*, 2014a; Suryanarayana, 1998). The Williamson–Hall plot for spheric ZnS nanocrystals as-prepared are here shown in Fig. 2d-f. In general, this trend observed in these Williamson–Hall results (negative slope) is due to the small crystallite size of about 3 nm obtained for these samples. This behavior has been explained in detail in a previous work (Suzuki *et al.*, 2019b).

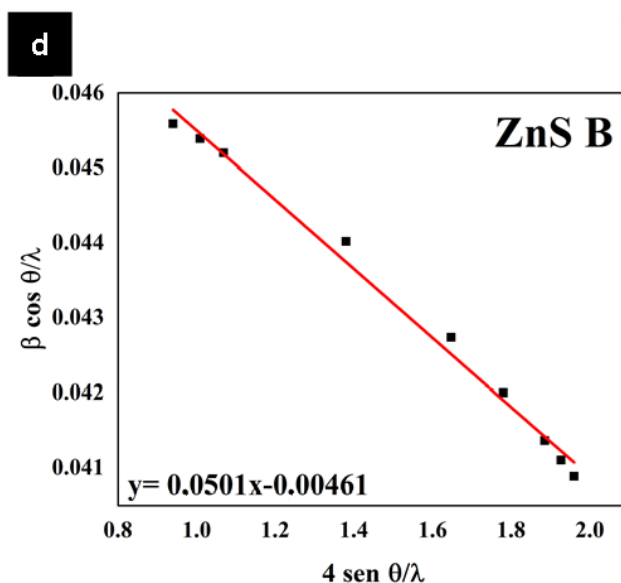
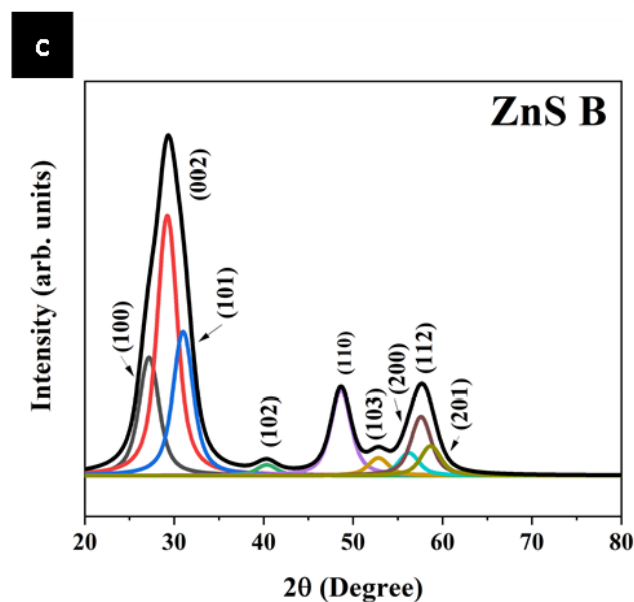
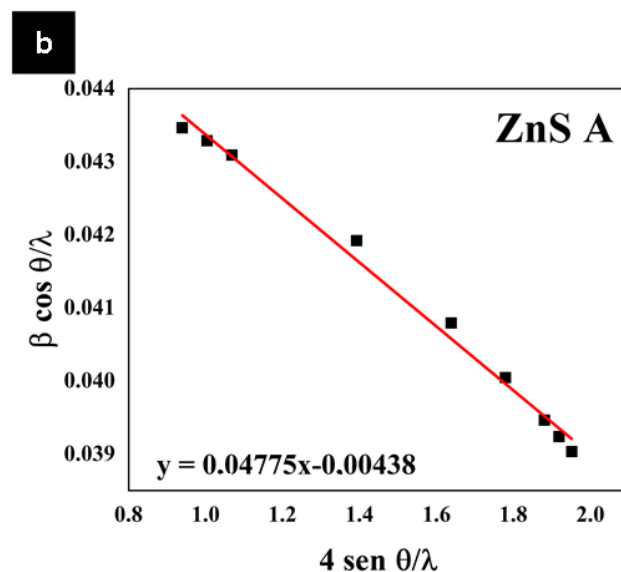
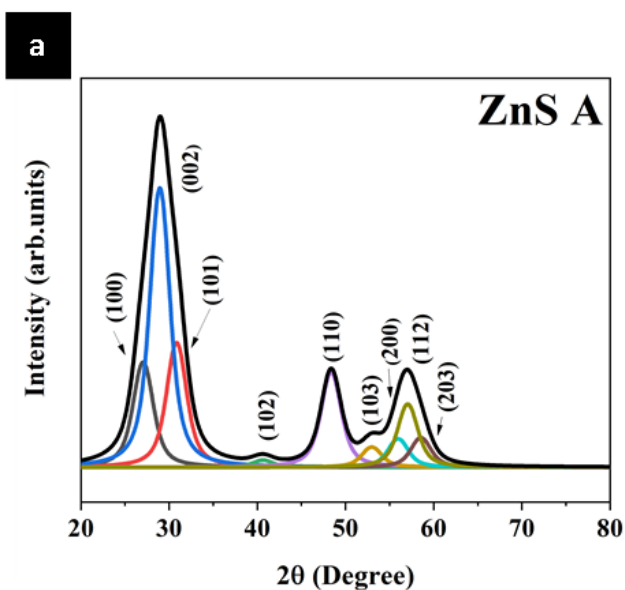
Moreover, the interplanar spacing (d_{hkl}) is related to the ZnS lattice parameters a and c , from Eqs. 4 and 5:

$$2d_{hkl} \sin \theta = n\lambda \quad (4)$$

$$\frac{1}{d^2} = \frac{4}{3} \left(\frac{h^2 + hk + k^2}{a^2} \right) + \frac{l^2}{c^2} \quad (5)$$

Using the estimated values of interplanar distance, according to the above expression, the lattice parameters a and c were calculated by the following relation (Eq. 6):

$$a = \frac{\lambda}{\sqrt{3} \sin \theta}, c = \frac{\lambda}{\sin \theta} \quad (6)$$



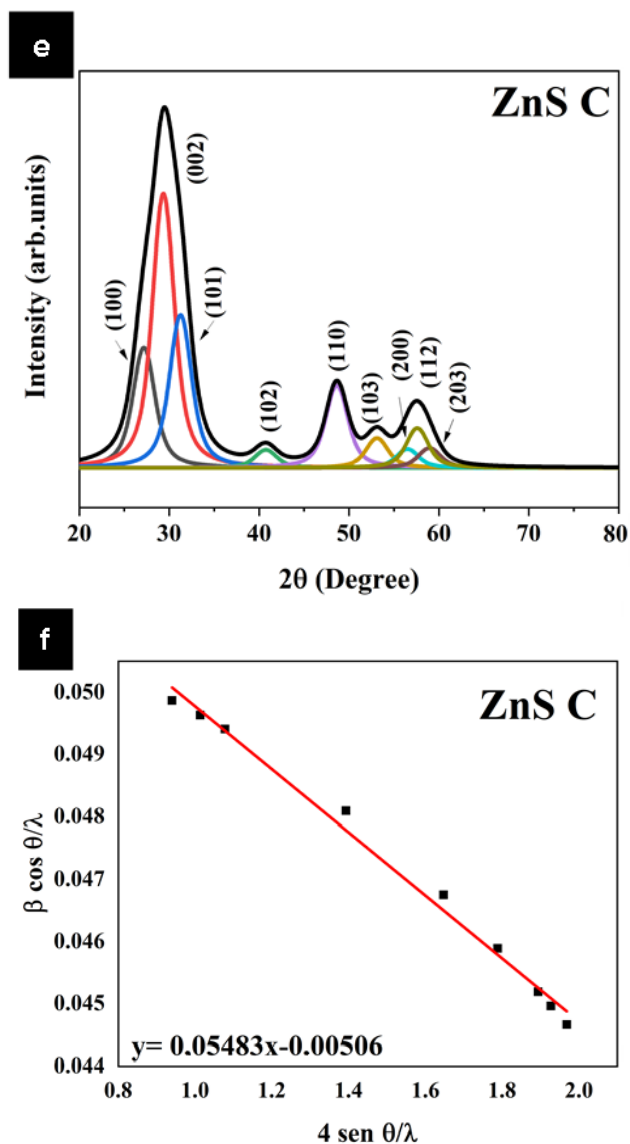


Figure 2. Deconvolution of XRD and Williamson–Hall analysis. (a–c) Deconvoluted XRD pattern into nine bands (according to JCPDS #36–1450); (d–f) Williamson–Hall analysis of the ZnS nanopowders.

As is well-known, the ZnS hexagonal structure (space group P63mc) is formed by tetragonal $[\text{ZnS}_4]$ clusters as shown in Fig. 3a. As is well-known, the low-Miller index $(10\bar{1}0)$, $(11\bar{2}0)$ and (0001) surface planes, in general, are the most stable faces of hexagonal ZnS structure and hence are usually predominant in the obtained crystals, it has been extensively characterized from the diverse theoretical and experimental methodologies (Hamad *et al.*, 2002; La Porta *et al.*, 2017; Meng *et al.*, 2013). However, a more detailed analysis of clusters formed by the $(10\bar{1}0)$, $(11\bar{2}0)$ and (0001) surfaces show different atom arrangements as seen in Fig. 3. The surface modeling shows that for the

$(10\bar{1}0)$ and $(11\bar{2}0)$, the outermost layers are mainly composed by $[\text{ZnS}_3]$ clusters, as its inner layers are composed by $[\text{ZnS}_4]$; as well as the (0001) which is formed by $[\text{ZnS}_4]$ clusters (Fig. 3). This leads to modulation of the catalytic activity in these crystal planes. In line with theoretical and experimental results, a decrease in cluster coordination of these exposed surfaces, particularly, contributes to an increase in surface energy, leading to a high chemical reactivity of these crystal planes (La Porta *et al.*, 2017; Huang *et al.*, 2012; Su *et al.*, 2014); however, as it can depend on the symmetry and between system planes, the results do not follow it perfectly. The surface energy of the (0001) , $(10\bar{1}0)$ and $(11\bar{2}0)$ surfaces are shown in Tab. 1, in which the following stability order $(10\bar{1}0) > (11\bar{2}0) > (0001)$ is shown. Even though the (0001) does not follow perfectly the rule, the $(10\bar{1}0)$ is more favorable than the $(11\bar{2}0)$ due to its lower concentration of $[\text{ZnS}_3]$ in the exposed surface (La Porta *et al.*, 2017).

It is well-known that the UV-Vis absorption spectrum of colloidal semiconductor nanocrystals is size-dependent, as a direct consequence of the quantum confinement effect (El-Sayed, 2004; Jesus *et al.*, 2021; Talapin *et al.*, 2010). Figure 4a shows the first derivative UV-Vis absorption spectra of spherical ZnS nanocrystals, which were recorded after the powder sample being dispersed in water. For ZnS samples, it shows a red-shifted of the UV-Vis absorption peak at about 315, 317 and 323 nm, which is consistent with an increase in particle size and with the literature of ZnS (Yoffe, 2001). According to Calandra *et al.* (1999), the mathematical relation for the estimation of spherical diameter of the ZnS nanocrystals from the UV-Vis absorption peak is expressed as:

$$\lambda_{max} = 186.7d_s^{0.13} \quad (7)$$

As expected from the following power law (Eq. 7), the spherical diameter values of samples A, B and C are, respectively, 55.9, 58.7 and 67.8 nm. Optical energies of the bandgap for these ZnS samples have been determined in this study by the analysis of their first derivative UV-Vis absorption curves according to a methodology discussed by Suzuki *et al.*, (2019a). As a result, the bandgap for the samples under study are shown in Tab. 1 and are in the range of 3.78 to 3.62 eV. In principle, a comparison of these results and theoretical calculations are also shown in Fig. 4c, reveals the formation of intermediate levels inside the bandgap due to structural polarization, as has been proposed by Varela and co-authors (La Porta *et al.*, 2013b; 2014a).

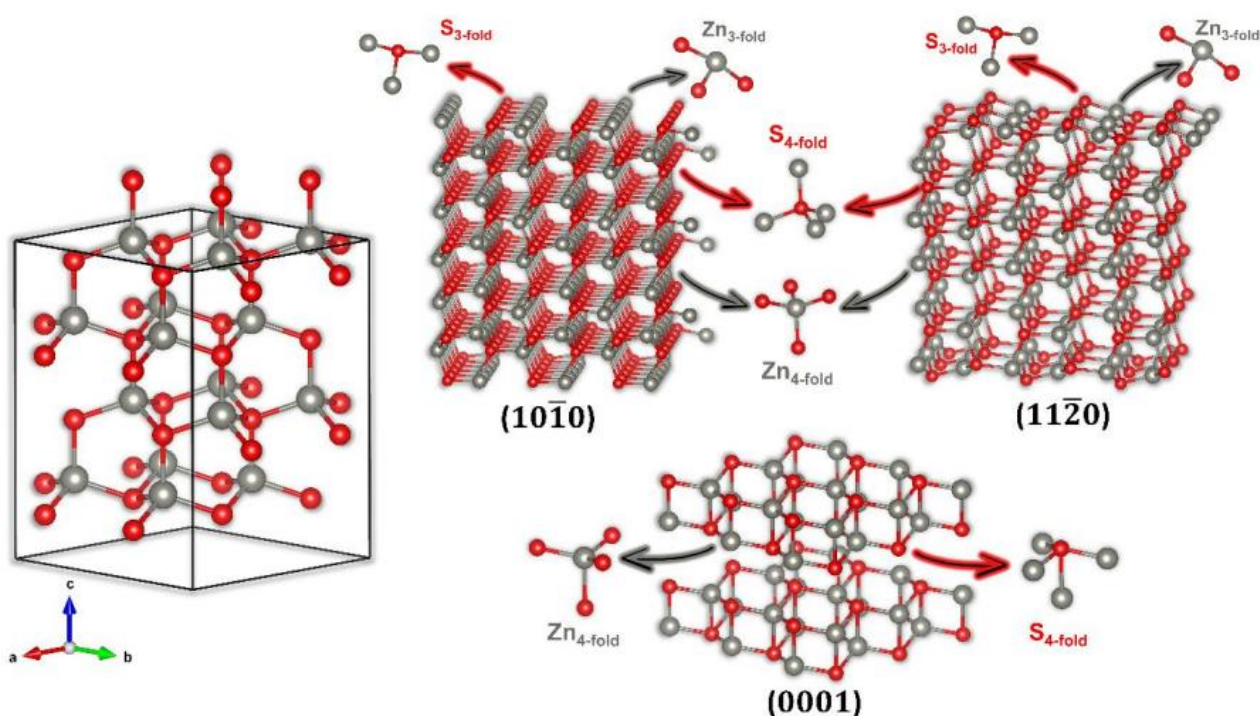


Figure 3. Illustration of the hexagonal ZnS unit cell and the cluster configurations for the (0001), (10 $\bar{1}$ 0) and (11 $\bar{2}$ 0) crystal planes.

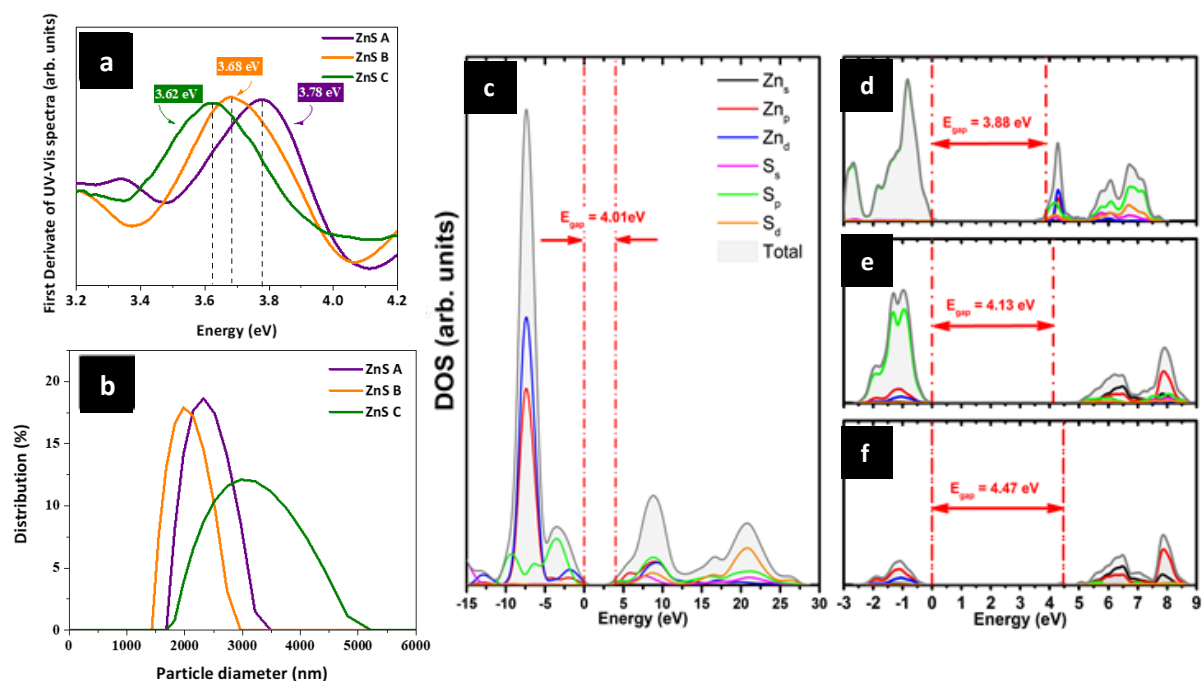


Figure 4. (a) First-derivative curves of the UV-Vis spectra. (b) DLS particle size analysis of the ZnS nanoparticles in water. Density of states of ZnS; (c) bulk; (d) (10 $\bar{1}$ 0); (e) (11 $\bar{2}$ 0); (f) (0001) surfaces.

Additionally, the projected density of states analysis for bulk ZnS model in Fig. 4c shows that the valence bands are mainly composed of sulfur 3p orbitals with a minor contribution of the zinc 3p orbitals, along with 3p and 4s zinc orbitals in the conduction band. From the

ZnS surface models, it can be observed that the valence bands are quite similar to what was observed for the bulk, but in the conduction band the (10 $\bar{1}$ 0) and (0001) has a major contribution of the zinc 4s orbital and a minor of zinc 3p orbital, but the (11 $\bar{2}$ 0) has an equal

contribution of the zinc 4s and 3p orbitals with a minor contribution from the 3p from the sulfur (Fig. 4d and f).

Next, to complement the experimental results, the hydrodynamic diameter of the dispersed phase particles in solution was determined by DLS, in which the method is based on the analysis of light intensity fluctuations of light scattered by particles in the chaotic Brownian motion state (Lorber *et al.*, 2012; Stetefeld *et al.*, 2016). Figure 4b shows the hydrodynamic diameter values for the ZnS nanoparticles, dispersed in water. An analysis of the particle distribution obtained by the DLS suggests an increase in the size distribution with a decrease in the concentration of precursors, which is consistent with the UV-Vis results.

Also, the zeta potential of ZnS nanoparticles with varying concentrations of precursors was also measured on the same instrument, as shown in Fig. 5, which presents the stability characteristic of the system, for nanoparticles in solution by detecting the Doppler frequency change in scattered light because of particle motion (Kuznetsova *et al.*, 2016). As expected, an increase in the positive charge of ZnS nanocrystals was seen, which consists of the formation of sulfur vacancies. In addition, these results have agreed with the theoretical calculations.

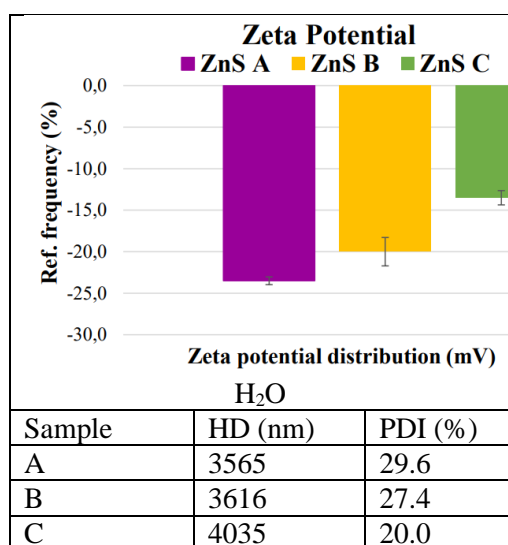
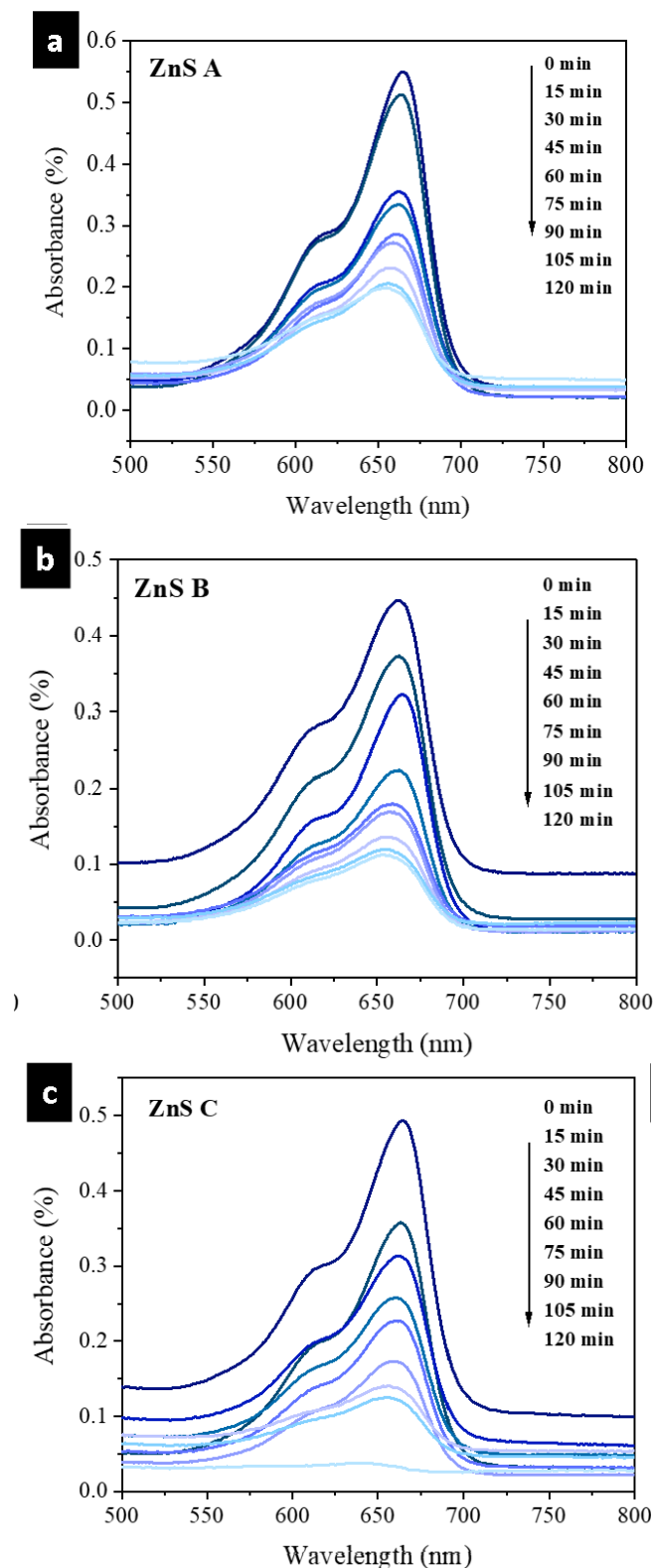


Figure 5. Zeta potential, hydrodynamic diameter (HD) and polydispersion index (PDI) of the ZnS nanoparticles.

The photocatalytic degradation of aqueous MB dye solution by ZnS samples was also investigated in this study (Fig. 6a–d). It is well-known that the photodegradation efficiency of the catalysts can, in principle, be fully adjusted through pseudo-first order reaction kinetics (Eq. 8):

$$\ln\left(\frac{C}{C_0}\right) = kt \quad (8)$$



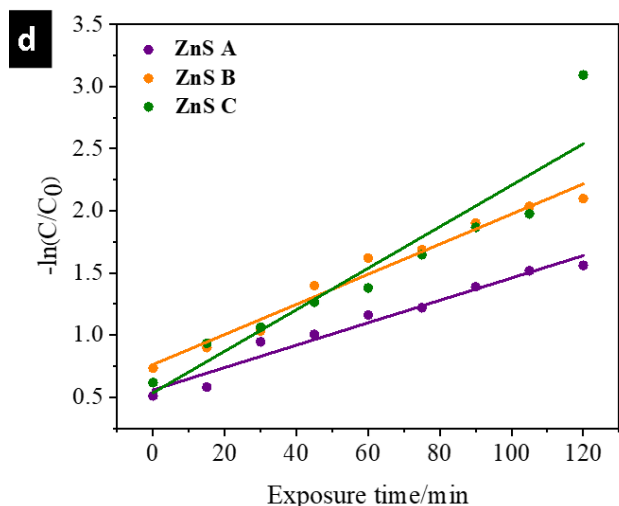
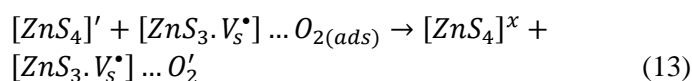
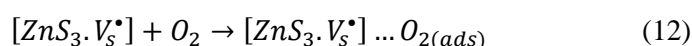
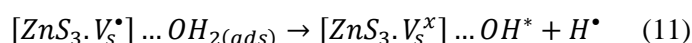
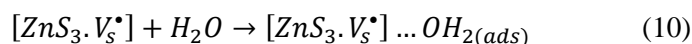
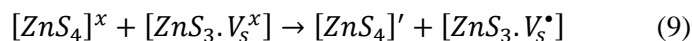


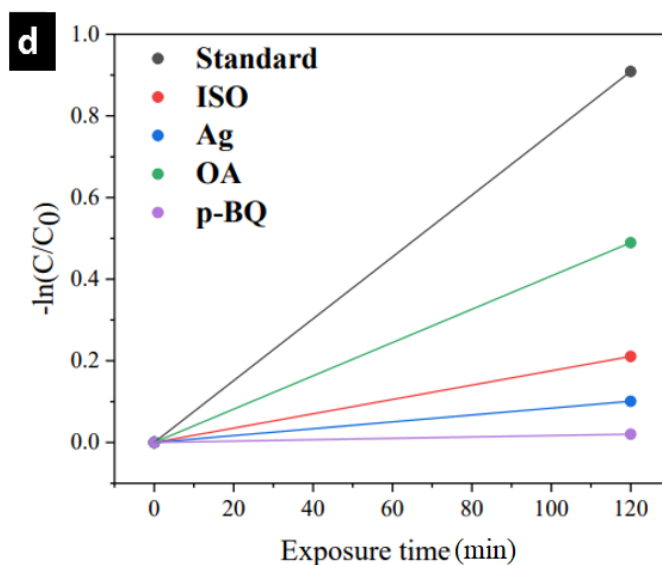
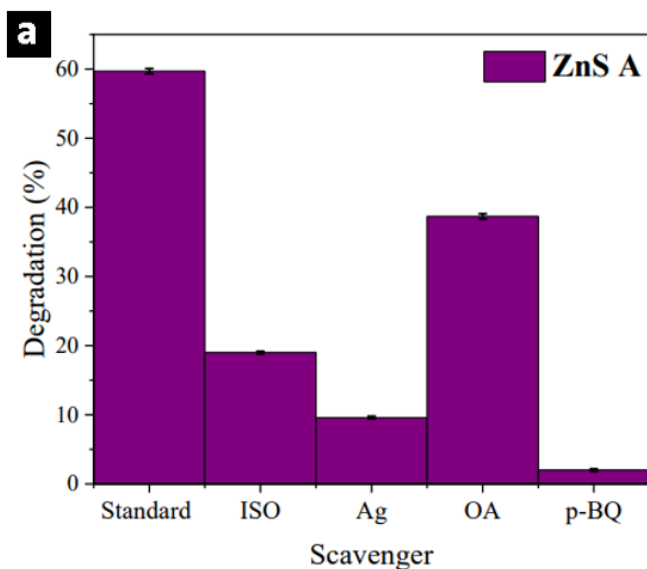
Figure 6. (a-c) UV-Vis absorption spectra of MB solutions at various irradiation times in the presence of the catalysts; (d) $\ln(C/C_0)$ vs. degradation time.

As a result, it was observed that sample C is a better photocatalyst ($k = 0.0115$) than B ($k = 0.0111$) and A ($k = 0.0082$). This is due to the greater number of structural defects and sulfur vacancies on the ZnS samples, considerably favoring the adsorption of water (H_2O) and molecular oxygen (O_2) dissolved in MB solution. Thus, the following Eqs. 9–13, based on the Kröger–Vink notation (Chen *et al.*, 2015; Kröger and Vink, 1956; La Porta *et al.*, 2017; Sousa *et al.*, 2020), are used to explain

the formation of the reactive oxygen species (ROS), which are usually responsible for degrading MB dye solution (Chen *et al.*, 2015; Pereira *et al.*, 2018; Su *et al.*, 2014).



It is well-known that photodegradation reactions are conducted by ROS (Chen *et al.*, 2015; Pereira *et al.*, 2018; Zhang *et al.*, 2012), as shown in the proposed mechanism above (Eqs. 9–13). Thus, with the specific purpose of confirming the formation of ROS, photodegradation tests were performed in the presence of different radical scavengers (Suzuki *et al.*, 2021). Figure 7 showed that the addition of AO, as a holes (h^\bullet) scavenger, did not cause significant changes in the photocatalytic degradation of the MB dye solution.



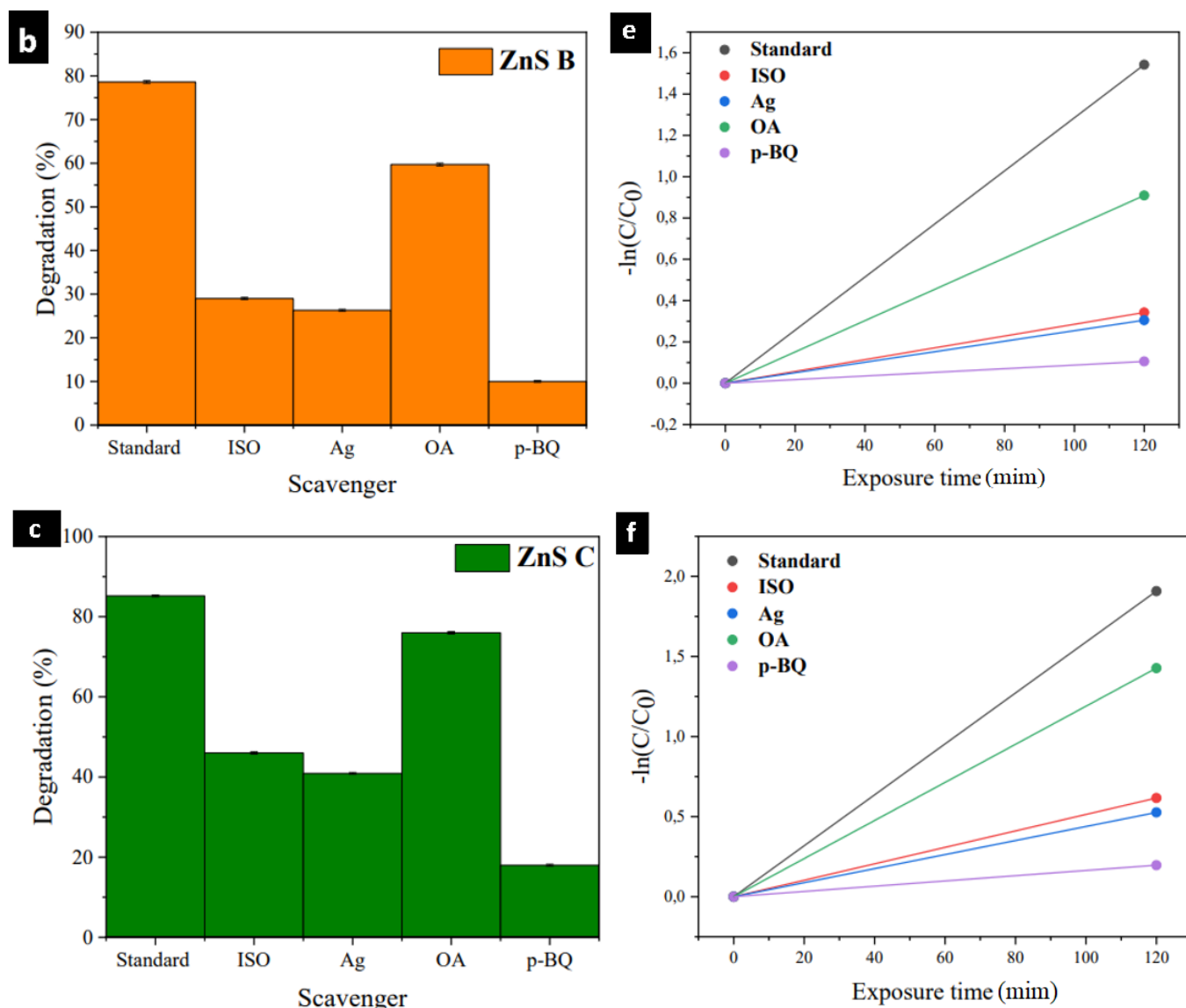


Figure 7. (a-c) Variation of degradation efficiency and (d-f) $\ln(C/C_0)$ vs. degradation time for the ZnS samples in the presence of different scavengers.

In comparison, as illustrated in Fig. 7, it was found that the photodegradation of the MB dye solution is notably inhibited by the addition of ISO, Ag and p-BQ, which are reactive species such as radical species (OH^*), electron (e^-) and superoxide radicals ($\text{O}_2^{\bullet-}$), indicating a more significant role to the photocatalytic mechanism. Photodegradation tests suggest that the high concentration of sulfur vacancies and structural defects significantly contribute to the adsorption of H_2O and O_2 , improving the material's photocatalytic activity (Chen *et al.*, 2015; Liqiang *et al.*, 2006). Therefore, from this perspective, it can be assumed that these ROS are the active species responsible for leading to the complete degradation of the MB dye solution (Amorin *et al.*, 2019).

4. Conclusions

ZnS nanoparticles with different degrees of crystallinity were synthesized by the one-pot solvothermal method under different concentrations of zinc acetate/thiourea precursors. It was found from XRD patterns that the samples have a hexagonal structure, varying the crystallite size range from 2.48 to 2.85 nm. The DLS and UV-Vis measurements were also performed to analyze the particle size distribution and its optical properties. Overall, the results show the decrease in the concentration of precursors favors the formation of sulfur vacancies. Furthermore, bandgap engineering has a significant impact on the photocatalytic response of these samples. A

photocatalysis mechanism was investigated and confirmed the formation of ROS. Therefore, these complex defects are more effective sites for adsorption, leading to improved photocatalytic response. Studies are ongoing to assess the interaction of ZnS nanocrystals with the main protease of SARS-CoV-2.

Authors' contribution

Conceptualization: La Porta, F. A.

Data curation: Benatto, V. G.; Fabris, G. S. L.

Formal Analysis: Benatto, V. G.; Fabris, G. S. L.; La Porta, F. A.

Funding acquisition: La Porta, F. A.; Taft, C. A.; Sambrano, J. R.

Investigation: Benatto, V. G.; Fabris, G. S. L.

Methodology: Benatto, V. G.; Fabris, G. S. L.

Project administration: La Porta, F. A.; Taft, C. A.; Sambrano, J. R.

Resources: La Porta, F. A.; Taft, C. A.; Sambrano, J. R.

Software: Sambrano, J. R.; Fabris, G. S. L.

Supervision: La Porta, F. A.; Taft, C. A.; Sambrano, J. R.

Validation: Benatto, V. G.; Fabris, G. S. L.

Visualization: Benatto, V. G.; Fabris, G. S. L.

Writing – original draft: Benatto, V. G.; Fabris, G. S. L.

Writing – review & editing: La Porta, F. A.; Taft, C. A.; Sambrano, J. R.

Data availability statement

The data will be available upon request.

Funding

Fundação de Amparo à Pesquisa do Estado de São Paulo (FAPESP). Grant No: 2019/08928-9; 2013/07296-2.

Conselho Nacional de Desenvolvimento Científico e Tecnológico (CNPq). Grant No: 304604/2018-6; 307213/2021-8.

Coordenação de Aperfeiçoamento de Pessoal de Nível Superior (CAPES). Finance Code 001; Grant No: 88887.467334/2019-00.

Molecular Simulations Laboratory (São Paulo State University, Bauru, Brazil).

Acknowledgments

The deceased Prof. Dr. J. A. Varela (São Paulo State University, Brazil) did the research for decades with advanced ceramics, in collaboration with other experimental/theoretical groups, leaving a very important legacy still used by many groups in their work today. This research paper is dedicated to his memory.

References

Amorin, L. H.; Suzuki, V. Y.; Paula, N. H.; Duarte, J. L.; Silva, M. A. T.; Taft, C. A.; La Porta, F. A. Electronic, structural, optical, and photocatalytic properties of graphitic carbon nitride. *New J. Chem.* **2019**, *43* (34), 13647–13653. <https://doi.org/10.1039/C9NJ02702E>

Ayala-Durán, S. C.; Hammer, P.; Nogueira, R. F. P. Surface composition and catalytic activity of an iron mining residue for simultaneous degradation of sulfonamide antibiotics. *Environ. Sci. Pollut. Res.* **2020**, *27*, 1710-1720. <https://doi.org/10.1007/s11356-019-06662-1>

Ayodhya, D.; Veerabhadram, G. A review on recent advances in photodegradation of dyes using doped and heterojunction based semiconductor metal sulfide nanostructures for environmental protection. *Mater. Today Energy* **2018**, *9*, 83-113. <https://doi.org/10.1016/j.mtener.2018.05.007>

Bilal, M.; Adeel, M.; Rasheed, T.; Zhao, Y.; Iqbal, H. M. N. Emerging contaminants of high concern and their enzyme-assisted biodegradation - A review. *Environ. Int.* **2019**, *124*, 336-353. <https://doi.org/10.1016/j.envint.2019.01.011>

Byrne, C.; Subramanian, G.; Pillai, S. C. Recent advances in photocatalysis for environmental applications. *J. Environ. Chem. Eng.* **2018**, *6*, 3531-3555. <https://doi.org/10.1016/j.jece.2017.07.080>

Calandra, P.; Goffredi, M.; Liveri, V. T. Study of the growth of ZnS nanoparticles in water/AOT/nheptane microemulsions by UV-absorption spectroscopy. *Colloids Surfaces A Physicochem. Eng. Asp.* **1999**, *160*, 9-13. [https://doi.org/10.1016/S0927-7757\(99\)00256-3](https://doi.org/10.1016/S0927-7757(99)00256-3)

Chen, D.; Huang, F.; Ren, G.; Li, D.; Zheng, M.; Wang, Y.; Lin, Z. ZnS nano-architectures: Photocatalysis, deactivation and regeneration. *Nanoscale* **2010**, *2*, 2062-2064. <https://doi.org/10.1039/c0nr00171f>

Chen, S.; Shen, S.; Liu, G.; Qi, Y.; Zhang, F.; Li, C. Interface engineering of a CoOx/Ta3N5 photocatalyst for unprecedented water oxidation performance under visible-light- Irradiation. *Angew. Chemie - Int. Ed.* **2015**, *54*, 3047-3051. <https://doi.org/10.1002/anie.201409906>

Chen, K.; Tang, W.; Chen, Y.; Yuan, R.; Lv, Y.; Shan, W.; Zhang, W. H. A facile solution processed ZnO@ZnS core-

- shell nanorods arrays for high-efficiency perovskite solar cells with boosted stability. *J. Energy Chem.* **2021**, *61*, 553-560. <https://doi.org/10.1016/j.jechem.2021.02.018>
- Dovesi, R.; Saunders, V. R.; Roetti, C.; Orlando, R.; Zicovich-Wilson, C. M.; Pascale, F.; Civalleri, B.; Doll, K.; Harrison, N. M.; Bush, I. J.; D'Arco, P.; Llunell, M.; Causà, M.; Noël, Y.; Maschio, L.; Erba, A.; Rerat, M.; Casassa, S. C. CRYSTAL17 User's Manual. Univ. Torino, Torino (2017).
- El-Sayed, M. A. Small Is Different: Shape-, Size-, and Composition-Dependent Properties of Some Colloidal Semiconductor Nanocrystals. *Acc. Chem. Res.* **2004**, *37* (5), 326-333. <https://doi.org/10.1021/ar020204f>
- Guinier, A., Lorrain, P., Lorrain, D. S.; Gillis, J. X-Ray Diffraction in Crystals, Imperfect Crystals, and Amorphous Bodies. *Phys. Today* **1964**, *17*, 70-72. <https://doi.org/10.1063/1.3051547>
- Hamad, S.; Cristol, S.; Catlow, C. R. A. Surface structures and crystal morphology of ZnS: Computational study. *J. Phys. Chem. B* **2002**, *106*, 11002-11008. <https://doi.org/10.1021/jp026396d>
- Heller, L.; Mota, C. R.; Greco, D. B. COVID-19 faecal-oral transmission: Are we asking the right questions? *Sci. Total Environ.* **2020**, *729*, 138919. <https://doi.org/10.1016/j.scitotenv.2020.138919>
- Huang, W. C.; Lyu, L. M.; Yang, Y. C.; Huang, M. H. Synthesis of Cu₂O nanocrystals from cubic to rhombic dodecahedral structures and their comparative photocatalytic activity. *J. Am. Chem. Soc.* **2012**, *134*, 1261-1267. <https://doi.org/10.1021/ja209662v>
- Hussain, S.; Liu, T.; Javed, M. S.; Aslam, N.; Zeng, W. Highly reactive 0D ZnS nanospheres and nanoparticles for formaldehyde gas-sensing properties. *Sens. Actuators B Chem.* **2017**, *239*, 1243-1250. <https://doi.org/10.1016/j.snb.2016.09.128>
- Ippen, C.; Greco, T.; Kim, Y.; Kim, J.; Suk, M.; Jong, C.; Wedel, A. ZnSe / ZnS quantum dots as emitting material in blue QD-LEDs with narrow emission peak and wavelength tunability. *Org. Electron.* **2014**, *15*, 126-131. <https://doi.org/10.1016/j.orgel.2013.11.003>
- Jellison, G. E.; Wood, R. F. Antireflection coatings for planar silicon solar cells. *Solar Cells* **1986**, *18*, 93-114. [https://doi.org/10.1016/0379-6787\(86\)90029-3](https://doi.org/10.1016/0379-6787(86)90029-3)
- Jesus, J. P. A.; Jimenez, M. Z.; La Porta, F. de A. Theoretical investigation on the effects of electric field on the electronic structure and spectroscopic properties of Zn_{6-x}Cd_xS₆ clusters as model systems of semiconductor quantum dots. *Comput. Mater. Sci.* **2021**, *188*, 110147. <https://doi.org/10.1016/j.commatsci.2020.110147>
- Kröger, F. A.; Vink, H. J. Relations between the Concentrations of Imperfections in Crystalline Solids. *Solid State Phys.* **1956**, *3*, 307-435. [https://doi.org/10.1016/S0081-1947\(08\)60135-6](https://doi.org/10.1016/S0081-1947(08)60135-6)
- Kuznetsova, Y. V.; Kazantseva, A. A.; Rempel, A. A. Zeta Potential, Size, and Semiconductor Properties of Zinc Sulfide Nanoparticles in a Stable Aqueous Colloid Solution. *Russ. J. Phys. Chem. A* **2016**, *90*, 864-869. <https://doi.org/10.1134/S0036024416040154>
- La Porta, F. A.; Ferrer, M. M.; Santana, Y. V. B.; Raubach, C. W.; Longo, V. M.; Sambrano, J. R.; Longo, E.; Andrés, J.; Li, M. S.; Varela, J. A. Towards an Understanding on the Role of Precursor in the Synthesis of ZnS Nanostructures. *Curr. Phys. Chem.* **2013a**, *3*(4), 378-385. <https://doi.org/10.2174/18779468113036660012>
- La Porta, F. A.; Ferrer, M. M.; De Santana, Y. V. B.; Raubach, C. W.; Longo, V. M.; Sambrano, J. R.; Longo, E.; Andrés, J.; Li, M. S.; Varela, J. A. Synthesis of Wurtzite ZnS Nanoparticles Using the Microwave Assisted Solvothermal Method. *J. Alloys Compd.* **2013b**, *556*, 153-159. <https://doi.org/10.1016/j.jallcom.2012.12.081>
- La Porta, F. A.; Andrés, J.; Li, M. S.; Sambrano, J. R.; Varela, J. A.; Longo, E. Zinc Blende versus Wurtzite ZnS Nanoparticles: Control of the Phase and Optical Properties by Tetrabutylammonium Hydroxide. *Phys. Chem. Chem. Phys.* **2014a**, *16* (37), 20127-20137. <https://doi.org/10.1039/C4CP02611J>
- La Porta, F. A.; Gracia, L.; Andrés, J.; Sambrano, J. R.; Varela, J. A.; Longo, E. A DFT Study of Structural and Electronic Properties of ZnS Polymorphs and Its Pressure-Induced Phase Transitions. *J. Am. Ceram. Soc.* **2014b**, *97* (12), 4011-4018. <https://doi.org/10.1111/jace.13191>
- La Porta, F. A.; Nogueira, A. E.; Gracia, L.; Pereira, W. S.; Botelho, G.; Mulinari, T. A.; Andrés, J.; Longo, E. An Experimental and Theoretical Investigation on the Optical and Photocatalytic Properties of ZnS Nanoparticles. *J. Phys. Chem. Solids* **2017**, *103*, 179-189. <https://doi.org/10.1016/j.jpcs.2016.12.025>
- Lee, G.; Wu, J. J. Recent developments in ZnS photocatalysts from synthesis to photocatalytic applications - A review. *Powder Technol.* **2017**, *318*, 8-22. <https://doi.org/10.1016/j.powtec.2017.05.022>
- Li, J.; Wu, Q.; Wu, J. Synthesis of Nanoparticles via Solvothermal and Hydrothermal Methods. In: Aliofkhae, M. (eds) Handbook of Nanoparticles. Springer, Cham., **2016**, 265-293. <https://doi.org/10.1007/978-3-319-15338-4>
- Lin, Z. Q.; Wang, G. G.; Li, L. H.; Wang, H.; Tian, J. L.; Zhang, H. Y.; Han, J. C. Preparation and Protection of ZnS Surface Sub-Wavelength Structure for Infrared Window. *Appl. Surf. Sci.* **2019**, *470*, 395-404.

<https://doi.org/10.1016/j.apsusc.2018.11.156>

Liqiang, J.; Yichun, Q.; Baiqi, W.; Shudan, L.; Baojiang, J.; Libin, Y.; Wei, F.; Honggang, F.; Jiazhong, S. Review of photoluminescence performance of nano-sized semiconductor materials and its relationships with photocatalytic activity. *Sol. Energy Mater. Sol. Cells* **2006**, *90*, 1773-1787. <https://doi.org/10.1016/j.solmat.2005.11.007>

Lorber, B.; Fischer, F.; Bailly, M.; Roy, H.; Kern, D. Protein analysis by dynamic light scattering: Methods and techniques for students. *Biochem. Mol. Biol. Educ.* **2012**, *40*, 372-382. <https://doi.org/10.1002/bmb.20644>

Meng, X.; Xiao, H.; Wen, X.; Goddard, W. A.; Li, S.; Qin, G. Dependence on the structure and surface polarity of ZnS photocatalytic activities of water splitting: First-principles calculations. *Phys. Chem. Chem. Phys.* **2013**, *15*, 9531-9539. <https://doi.org/10.1039/c3cp50330e>

Mukherjee, S.; Selvaraj, J.; Paramasivam, T. Ag-Doped ZnInS/ZnS Core/Shell Quantum Dots for Display Applications. *ACS Appl. Nano Mater.* **2021**, *4*, 10228-10243. <https://doi.org/10.1021/acsnm.1c01720>

Pereira, W. da S.; Sczancoski, J. C.; Calderon, Y. N. C.; Mastelaro, V. R.; Botelho, G.; Machado, T. R.; Leite, E. R.; Longo, E. Influence of Cu substitution on the structural ordering, photocatalytic activity and photoluminescence emission of Ag_{3-2x}Cu_xPO₄ powders. *Appl. Surf. Sci.* **2018**, *440*, 61-72. <https://doi.org/10.1016/j.apsusc.2017.12.202>

Santana, Y. V. B.; Raubach, C. W.; Ferrer, M. M.; La Porta, F. A.; Sambrano, J. R.; Longo, V. M.; Leite, E. R.; Longo, E. Experimental and theoretical studies on the enhanced photoluminescence activity of zinc sulfide with a capping agent. *J. Appl. Phys.* **2011**, *110*, 123507. <https://doi.org/10.1063/1.3666070>

Sousa, G. S.; Nobre, F. X.; Araújo Júnior, E. A.; Sambrano, J. R.; Albuquerque, A. dos R.; Bindá, R. dos S.; Couceiro, P. R. da C.; Brito, W. R.; Cavalcante, L. S.; Santos, M. R. de M. C.; Matos, J. M. E. Hydrothermal synthesis, structural characterization and photocatalytic properties of β-Ag₂MoO₄ microcrystals: Correlation between experimental and theoretical data. *Arab. J. Chem.* **2020**, *13*, 2806-2825. <https://doi.org/10.1016/j.arabjc.2018.07.011>

Stetefeld, J.; McKenna, S. A.; Patel, T. R. Dynamic light scattering: a practical guide and applications in biomedical sciences. *Biophys. Rev.* **2016**, *8*, 409-427. <https://doi.org/10.1007/s12551-016-0218-6>

Su, D.; Dou, S.; Wang, G. Single crystalline Co₃O₄ nanocrystals exposed with different crystal planes for Li-o₂ batteries. *Sci. Rep.* **2014**, *4*, 5767. <https://doi.org/10.1038/srep05767>

Sultana, A.; Middya, T. R.; Mandal, D. ZnS-paper based flexible piezoelectric nanogenerator. *AIP Conf. Proc.* **2018**, *1942*, 120018. <https://doi.org/10.1063/1.5029058>

Suryanarayana, C., Norton, M. G. Practical Aspects of X-Ray Diffraction. In: X-Ray Diffraction. Springer **1998**, 63-94. https://doi.org/10.1007/978-1-4899-0148-4_3

Suzuki, V. Y.; Amorin, L. H. C.; Lima, N. M.; Machado, E. G.; Carvalho, P. E.; Castro, S. B. R.; Alves, C. C. S.; Carli, A. P.; Li, M. S.; Longo, E.; La Porta, F. A. Characterization of the Structural, Optical, Photocatalytic and: In Vitro and in Vivo Anti-Inflammatory Properties of Mn²⁺ Doped Zn₂GeO₄ Nanorods. *J. Mater. Chem. C* **2019a**, *7* (27), 8216-8225. <https://doi.org/10.1039/c9tc01189g>

Suzuki, V. Y.; Paula, N. H.; Gonçalves, R.; Li, M. S.; Pereira, E. C.; Longo, E.; La Porta, F. A. Exploring Effects of Microwave-Assisted Thermal Annealing on Optical Properties of Zn₂GeO₄ Nanostructured Films. *Mater. Sci. Eng. B Solid-State Mater. Adv. Technol.* **2019b**, *246*, 7-12. <https://doi.org/10.1016/j.mseb.2019.05.023>

Suzuki, V. Y.; Amorin, L. H. C.; de Paula, N. H.; Albuquerque, A. R.; Li, M. S.; Sambrano, J. R.; Longo, E.; La Porta, F. A. New Insights into the Nature of the Bandgap of CuGeO₃ Nanofibers: Synthesis, Electronic Structure, and Optical and Photocatalytic Properties. *Mater. Today Commun.* **2021**, *26*, 101701. <https://doi.org/10.1016/j.mtcomm.2020.101701>

Talapin, D. V.; Mekis, I.; Go, S.; Kornowski, A.; Benson, O.; Weller, H. CdSe/CdS/ZnS and CdSe/ZnSe/ZnS Core-Shell Nanocrystals. *J. Phys. Chem. B* **2004**, *108* (49), 18826-18831. <https://doi.org/10.1021/jp046481g>

Talapin, D. V.; Lee, J. S.; Kovalenko, M. V.; Shevchenko, E. V. Prospects of Colloidal Nanocrystals for Electronic and Optoelectronic Applications. *Chem. Rev.* **2010**, *110* (1), 389-458. <https://doi.org/10.1021/cr900137k>

Wang, X.; Shi, J.; Feng, Z.; Li, M.; Li, C. Visible Emission Characteristics from Different Defects of ZnS Nanocrystals. *Phys. Chem. Chem. Phys.* **2011**, *13* (10), 4715-4723. <https://doi.org/10.1039/c0cp01620a>

Wang, P.; Wu, Z.; Wu, M.; Wei, J.; Sun, Y.; Zhao, Z. All-Solution-Processed, Highly Efficient and Stable Green Light-Emitting Devices Based on Zn-Doped CsPbBr₃/ZnS Heterojunction Quantum Dots. *J. Mater. Sci.* **2021**, *56* (6), 4161-4171. <https://doi.org/10.1007/s10853-020-05527-0>

Xiao, J.; Song, C.; Song, M.; Dong, W.; Li, C.; Yin, Y. Preparation and Gas Sensing Properties of Hollow ZnS Microspheres. *J. Nanosci. Nanotechnol.* **2016**, *16* (3), 3026-3029. <https://doi.org/10.1166/jnn.2016.10765>

Yoffe, A. D. Semiconductor Quantum Dots and Related Systems: Electronic, Optical, Luminescence and Related

Properties of Low Dimensional Systems. *Adv. Phys.* **2001**, 50 (1), 1-208. <https://doi.org/10.1080/00018730010006608>

Zhang, Y.; Zhang, N.; Tang, Z. R.; Xu, Y. J. Graphene Transforms Wide Band Gap ZnS to a Visible Light Photocatalyst. the New Role of Graphene as a Macromolecular Photosensitizer. *ACS Nano* **2012**, 6 (11), 9777-9789. <https://doi.org/10.1021/nm304154s>

Zhang, Z.; She, J.; Chen, H.; Deng, S.; Xu, N. Laser-Induced Doping and Fine Patterning of Massively Prepared Luminescent ZnS Nanospheres. *J. Mater. Chem. C* **2013**, 1 (32), 4970-4978. <https://doi.org/10.1039/c3tc30714j>

Ziegler, B. J.; Xu, S.; Kucur, E.; Meister, F.; Batentschuk, M.; Gindele, F.; Nann, T. Silica-Coated InP/ZnS Nanocrystals as Converter Material in White LEDs. *Adv. Mater.* **2008**, 20 (21), 4068-4073. <https://doi.org/10.1002/adma.200800724>

Voltammetric glassy carbon sensor approach for the extended stability studies of doxorubicin in lyophilized dosage form

Carlos Eduardo Peixoto Cunha^{1+✉}, Edson Silvio Batista Rodrigues^{1✉}, Jerônimo Raimundo de Oliveira Neto^{1✉}, Vernon Somerset^{2✉}, Stephânia Taveira^{1✉}, Livia Flório Sgobbi^{3✉}, Eric de Souza Gil^{1✉}

1. Federal University of Goiás, Pharmacy, Goiânia, Brazil.
2. Cape Peninsula University of Technology, Faculty of Applied Sciences, Cape Town, South Africa.
3. Federal University of Goiás, Chemistry, Goiânia, Brazil.

+Corresponding author: Carlos Eduardo Peixoto Cunha, **Phone:** +55 62 981120522 **Email address:** cedcunhap35@hotmail.com

ARTICLE INFO

Article history:

Received: November 03, 2021

Accepted: May 05, 2022

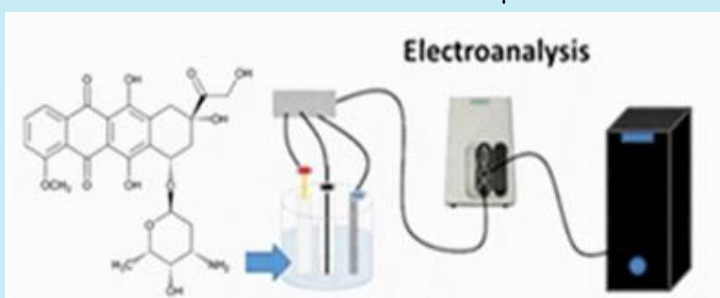
Published: July 01, 2022

Section Editor: Assis Vicente Benedetti

Keywords

1. electrochemistry
2. quality control of medicines
3. analytical validation
4. voltammetry
5. anticancer drugs

ABSTRACT: Doxorubicin (DOX) is an anthracycline antibiotic that is widely used in the clinical treatment of cancer patients. DOX has a high market value. Electroanalytical methods for DOX analysis are an alternative and promising approach compared to chromatographic techniques. In this context, electroanalysis provides a low-cost method for determining drugs such as DOX lyophilized powder for the injection. Differential pulse voltammetry with a glassy carbon electrode was used. DOX stability after reconstitution was performed, and the correct time for safe administration to patients in hospitals was determined. The electroanalytical method showed a limit of detection of $0.54 \mu\text{mol L}^{-1}$ and limit of quantification of $1.83 \mu\text{mol L}^{-1}$, which is enough for the application in quality control of DOX. The high-performance liquid chromatography analysis was also applied in pharmaceutical samples containing DOX to compare with the proposed method, showing that the obtained results are relatively similar for both methods. Therefore, the electroanalytical approach shows the viability of an attractive alternative technique for applying this sensor for drug quality control.



1. Introduction

Doxorubicin hydrochloride (DOX) (Fig. 1) is an anthracycline antibiotic which starting material is *Streptomyces percerius* var. *cesium*, which is widely used in the clinical treatment of patients with leukemias and tumors in the lung or breast. Doxorubicin hydrochloride is composed of an amino sugar linked to anthraquinone aglycone, as shown in its chemical structure (Fig. 1). Its mechanism of action is elucidated in four different ways, i.e., a) inhibition of deoxyribonucleic acid (DNA) synthesis in tumor cells; b) creation of free radicals, which can damage DNA; c) induction of DNA damage due to DOX interference with topoisomerase II; and d) induction of apoptosis (Alhareth *et al.*, 2012; Li *et al.*, 2020; Skalová *et al.*, 2020).

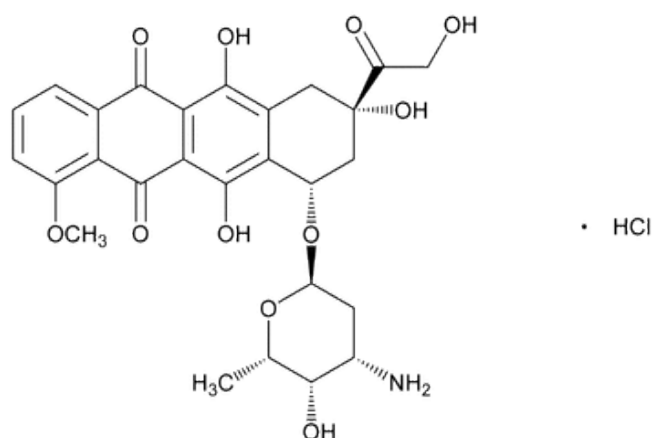


Figure 1. Doxorubicin chemical structure.

Doxorubicin hydrochloride is highly prescribed for therapeutic use in the form of a lyophilized powder for injection, so it is necessary to ensure the quality of the drug. Doxorubicin hydrochloride has a high market value, so it is a drug with less accessibility to patients with less purchasing power. However, hospitals allow the use of the DOX injection form to grant access to more patients. Nonetheless, it is necessary to carry out stability control after reconstitution of the lyophilized powder for DOX injection to ensure the drug's efficacy and safety (Navas *et al.*, 2013; Radi, 2003; Rodrigues *et al.*, 2018).

Quality control tests involve checking the content and possible impurities and stability of the drug. Techniques with good sensitivity are needed to perform the quality control tests for DOX, with the official methods used to determine the content consisting of high-performance liquid chromatography (HPLC) tests with UV detection and UV-VIS spectrometry (Felix and Angnes, 2018; Navas *et al.*,

2013). These techniques require expensive instrumentation, centralized laboratory and well-qualified personnel, time-consuming sample pretreatment steps in addition to making use of many organic reagents, also not environment-friendly (ACS, 2019; Hahn and Lee, 2004; Shellaiah and Sun, 2020).

As an alternative to those above conventional analytical methods, electrochemical sensors offer several remarkable attributes, such as low-cost instrumentation, elimination or reduction of sample pretreatment steps, fast response, and the possibility of online and *in situ* detection. Furthermore, electroanalytical methods provide good sensitivity, versatility, and cleaner and more sustainable analysis. The glassy carbon electrode (GCE) and the carbon paste electrode (CPE) have been used frequently among many electrodes employed in electroanalysis. Modifications of these electrodes, mostly with catalysts and/or nanoparticles, have displayed a significant increase in sensitivity for electrochemical detection (Hajian *et al.*, 2017; Shah *et al.*, 2018; Skalová *et al.*, 2020).

This work aims to perform the electroanalytical determination of DOX in lyophilized powder form, by differential pulse voltammetry (DPV) with a GCE sensor. We also aimed to verify the stability of DOX after reconstitution, establishing the correct time for safe administration to patients in hospitals. For comparison, DOX determination was also performed by HPLC-UV.

2. Materials and Methods

Electrolyte solutions were prepared using high analytical grade salts, which were solved in Milli-Q water (conductivity $\leq 0.1 \mu\text{S cm}^{-1}$) (Millipore S. A., Molsheim, France).

Analytical grade DOX was obtained from the United States Pharmacopeia (USP) ($\geq 99\%$). Pharmaceutical formulations of DOX (10 mg mL^{-1}) were kindly provided by a private oncology health unit (Rio de Janeiro/RJ – Brazil). The stock standard solution was prepared from a test dose of 27.18 mg in a 50 mL volumetric flask, then 25 mL of Milli-Q water was added and taken to ultrasound until complete solubilization, then the volume of the flask obtaining a concentration of 1.0 mmol L^{-1} DOX, the solution was prepared immediately before the experiments.

The samples of the reconstituted drug destined for the evaluation of the stability against the ambient temperatures and at 2 to 8 °C by voltammetric tests were prepared from an initial solution of DOX reconstituted in water for injection in its original packaging and divided into four 10-mL amber glass volumetric flasks. In contrast, those for monitoring by

chromatographic tests were packaged in four 100-mL amber glass volumetric flasks. The tests were performed at zero time and repeated in 2, 4, 6, 12, 24, 48, and 96 h in the samples exposed to the environmental conditions proposed by the study.

2.1. Electroanalytical tests

Voltammetric measurements were performed using a potentiostat/galvanostat PGSTAT model 204 with a FRA32M module (Metrohm Autolab, Eco Chemie, Netherlands) integrated with NOVA 2.1 software. All measurements were carried out in a 1-mL one-compartment electrochemical cell coupled to a three-electrode system consisting of a GCE, a Pt wire counter electrode and an Ag/AgCl/KCl_{sat} reference electrode (both purchased from Lab Solutions, São Paulo, Brazil).

The experimental conditions used for the DPV were pulse amplitude of 50 mV, pulse width of 0.5 s, and scan rate of 10 mV s⁻¹. All voltammetric assays were performed in 0.1 mol L⁻¹ phosphate buffer solution (PBS), pH 7.0. The DP voltammograms were background-subtracted and baseline-corrected. All experiments were conducted in triplicate, and data were analyzed using Origin Pro 9 software (Northampton, MA, USA). Between each voltammogram reading, the GCE was sanded with 0.3 μm alumina suspension and subsequently rinsed with Milli-Q water, in order to renew the electrode surface, thus ensuring the reproducibility of the tests.

2.2 Chromatography tests

For the chromatographic assay, a stainless-steel column (250 × 4.6 mm) was used, packed with octadecylsilyl silica gel for chromatography (5 μm) (Hypersil C18). The elution was isocratic with the mobile comprised of acetonitrile and acid surfactant solution (containing 0.288% w/v dodecyl sulfate and 0.225% w/v orthophosphoric acid) in a 50:50 (v/v) proportion. The analyses were performed at room temperature (25 °C). The flow was 1 mL min⁻¹, the wavelength was 254 nm, and the injection volume was 10 μL. The samples were prepared with 0.01% w/v of the reconstituted solution for injection diluted in the mobile phase, compared to the USP standard's declared value (USP, 2020; Zhao and Dash, 1999).

2.3 Method validation

The method was developed and validated for linearity, accuracy, precision, quantification limit,

detection limit, and selectivity in accordance with ICH Q2 (R1). The linearity of the method was performed through three analytical curves using DOX standard solutions. The results were statistically analyzed by linear regression analysis using the least squares method (ICH, 2014).

3. Results and discussion

3.1 Electroanalytical tests

The DP voltammogram obtained with GCE showed one main oxidation peak for DOX at $E_{pa} = 0.33$ V corresponding to oxidation in the quinonic portion of the anthracyclines drug class, followed by a second and third oxidation peaks, at $E_{pa} = 0.60$ V and $E_{pa} = 0.75$ V that are explained by the adsorption of DOX, attributed to the formation of a hydrogen bond between the hydroxyl groups of the phenolic compound and the carbonyl group (Piovesan and Spinelli, 2014).

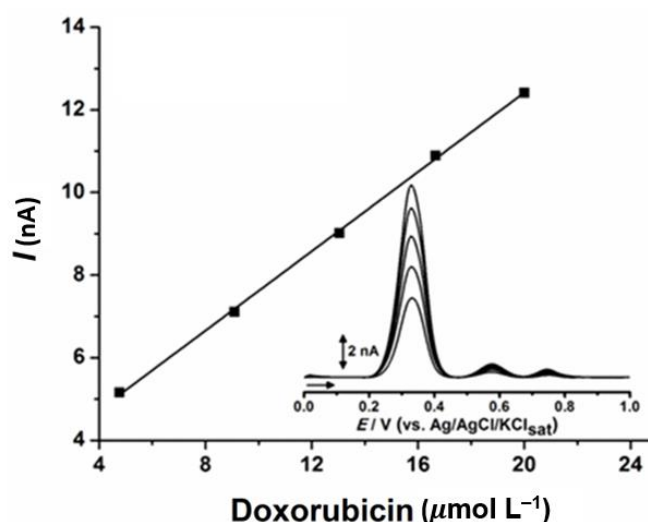


Figure 2. Calibration curve of DOX with DPV with GCE in PBS pH 7.0.

A calibration curve (Fig. 2) was constructed to determine the ideal concentration for DOX recovery in the stability study. Linearity was found on the calibration curve for the anodic peak E_{pa1} a.a. 0.33 V. As E_{pa1} presented a good linearity coefficient ($r^2 = 0.9993$), it was used to calculate the regression equation: $y = (2.81 \pm 0.09) + (0.48 \pm 0.01 \times [\text{DOX}])$ ($\mu\text{mol L}^{-1}$). As the p-value (0) found in the ANOVA F test is less than 0.05, it was rejected the null hypothesis (zero slope) at the significance level of 5%, whereas the P-value of 2755.7954 of the t-test is greater than 0.05, therefore, it was not rejected the null hypothesis (intercept equal to zero) at the significance level of 5%.

The correlation coefficient found of 0.9993 is greater than 0.9900, so it was concluded that there is an adequate linear relationship, showing residual sum of squares of 3.94×10^{-9} .

A comparison of the analytical parameters obtained by the proposed method and HPLC for the determination of DOX in pharmaceutical samples is described in [Tab. 1](#).

Table 1. Precision and Repeatability assays values for voltammetric and chromatographic assays.

Samples	Sample amount (%)	Methods	
		DPV – GCE (% ± SD) (n = 6)	HPLC (% ± SD) (n = 6)
DOX lyophilized powder for injection Repeatability (intraday)	100.0	101.4 ± 0.8	100.9 ± 0.2
DOX lyophilized powder for injection tablets Intermediary precision (interday)	100.0	101.0 ± 0.5	100.6 ± 0.1

SD: standard deviation.

For comparison reasons, HPLC recovery assays were performed. Repeatability assays were performed within a single day with intervals of 2 h. Intermediary precision assays were performed on three different days with three different analysts with intervals of 4 h for each day. It can be seen from [Tab. 1](#) that both methods displayed acceptable precision.

The voltammetric method displayed slightly higher deviations of precision in both assays in comparison with HPLC, as expected. However, due to the great

difference between equipment and preprocessing of both approaches, the precision difference shows that the method developed in this work is within an appropriate range of precision in comparison with pharmacopoeia methods. The results are further in agreement with the study conducted by [Macêdo et al. \(2020\)](#) and [Cunha et al. \(2019\)](#). Accuracy assays were also performed for both methods and the results are shown in [Tab. 2](#).

Table 2. Accuracy assays validation data for voltammetric and chromatographic assays for DOX lyophilized powder for injection.

Samples	Sample amount (%)	Methods	
		DPV – GCE (% ± RSD)	HPLC (% ± RSD)
DOX lyophilized powder for injection	80.0	81.4 ± 0.7	80.7 ± 0.2
	100.0	101.1 ± 0.5	101.5 ± 0.2
	120.0	120.7 ± 0.8	120.1 ± 0.4

RSD: Relative standard deviation.

As observed in [Tab. 2](#), the accuracy of both methods was satisfactory, with results within 5% deviation range. The chromatography approach showed only slightly lesser deviation than the voltammetric method with the GCE, corroborating the considerations

made previously. [Table 3](#) presents the limit of detection (LOD) and limit of quantification (LOQ) values of this study compared to the results obtained from the literature data used to determine DOX.

Table 3. Comparisons of the limits of detection and the limits of quantification in the determination of DOX with other methods.

Method	LOD	LOQ	Reference
DPV	0.54 $\mu\text{mol L}^{-1}$	1.83 $\mu\text{mol L}^{-1}$	This work
HPLC	0.5 ng mL^{-1}	5.0 ng mL^{-1}	Skalová et al., 2020
DPV-PGE	9.9 $\mu\text{mol L}^{-1}$	33.31 $\mu\text{mol L}^{-1}$	Cunha et al., 2019
DPCSV	0.44 $\mu\text{mol L}^{-1}$	0.6 $\mu\text{mol L}^{-1}$	Deepa et al., 2020
HPLC	0.2 ng mL^{-1}	0.6 ng mL^{-1}	Thomaz et al., 2018

Next, a summary and a comparison of our method depicted in [Tab. 3](#) were provided, which shows the current analytical approaches for the detection of DOX, from which it is possible to infer that an adequate

sensitivity was obtained for the simplified electroanalytical approach used. The results further demonstrate the availability of a faster analytical method and at a lower cost compared to other methods.

The electroanalytical method proposed in this work showed a LOD of $0.54 \mu\text{mol L}^{-1}$ and LOQ of $1.83 \mu\text{mol L}^{-1}$, which is sensitive enough for the application in quality control of DOX in lyophilized powder for injection.

3.2 Extended stability study test on a DOX pharmaceutical sample

The GCE sensor was also used to monitor the stability of DOX lyophilized powder for injection applications. In this context, injectable DOX solutions were evaluated after reconstitution at room temperature and at temperatures from 2 to 8 °C. Analytical assays

were performed at different times monitoring the decay of the DOX content after reconstitution, where the recovery in percentage after each period was evaluated, determining the stability after its reconstitution through the assay found (Tab. 4). As expected, the recovery values for voltammetric and chromatographic determinations showed DOX degradation after reconstitution. However, at room temperature, it shows DOX degradation after 48 h, while from 2 to 8 °C it remained stable until 96 h. (Tab. 4). All concentrations found were less than 5% of the relative standard deviation. Both methods showed effective approaches to assess the stability of DOX lyophilized powder for injection after reconstitution.

Table 4. Results obtained for the recovery of DOX in the evaluation of the extended stability study at different times.

Time (h)	% DOX (at room temperature)		% DOX (2–8 °C)	
	DPV	HPLC	DPV	HPLC
0	92.74	92.33	92.74	92.33
2	92.18	93.36	92.22	93.34
4	91.13	92.92	93.62	93.84
6	92.04	92.61	91.61	91.50
12	91.38	90.20	92.55	92.33
24	92.07	88.47	91.12	90.74
48	83.36	84.23	91.78	90.89
96	79.51	81.52	91.06	91.41

4. Conclusions

The GCE sensor, when compared to other sensors and evaluation methods, offers efficiency in its analytical performance for the determination of lyophilized powder for injection. This characteristic, when associated with low cost, easy access, quick and efficient cleaning of the electrode surface area, indicates that the GCE sensor can be a useful tool for DOX analysis. Also, the GCE sensor exhibited satisfactory detection and recovery, although the standard deviation values were slightly higher than most of the sensors and methods applied. However, the results are following the specifications for such an analysis. The general analytical performance and the low cost of the material associated with the immediate analysis provided by both electrodes, consistently justify the choice of these analytical devices as alternative approaches to quality control and extended drug stability studies.

Authors' contribution

Conceptualization: Cunha, C. E. P.; Gil, E. S.; Rodrigues, E. S. B.; Sgobbi, L. F.; Taveira, S. F
Data curation: Cunha, C. E. P.; Rodrigues, E. S. B.; Oliveira Neto, J. R.; Sgobbi, L. F.; Taveira, S. F
Formal Analysis: Cunha, C. E. P.; Rodrigues, E. S. B.; Oliveira Neto, J. R.; Sgobbi, L. F.; Taveira, S. F
Funding acquisition: Not applicable.
Investigation: Cunha, C. E. P.; Rodrigues, E. S. B.; Oliveira Neto, J. R.; Sgobbi, L. F.; Taveira, S. F
Methodology: Cunha, C. E. P.; Rodrigues, E. S. B.; Oliveira Neto, J. R.; Sgobbi, L. F.; Taveira, S. F
Project administration: Gil, E. S.
Resources: Gil, E. S.
Software: Not applicable.
Supervision: Gil, E. S.
Validation: Somerset, V.
Visualization: Cunha, C. E. P.; Rodrigues, E. S. B.; Oliveira Neto, J. R.; Sgobbi, L. F.; Taveira, S. F
Writing – original draft: Cunha, C. E. P.; Rodrigues, E. S. B.; Oliveira Neto, J. R.
Writing – review & editing: Gil, E. S.; Somerset, V.

Data availability statement

All dataset were generated or analyzed in the current study.

Funding

Not applicable.

Acknowledgments

We thank to AV Farma for their support and to the Federal University of Goiás (UFG) for supporting this work.

References

- ACS Publications Home Page. 2019. <https://pubs.acs.org/> (accessed 2019-02-21).
- Alhareth, K.; Vauthier, C.; Gueutin, C.; Ponchel, G.; Moussa, F. HPLC quantification of doxorubicin in plasma and tissues of rats treated with doxorubicin loaded poly(alkylcyanoacrylate) nanoparticles. *J. Chromatogr. B Biomed. Appl.* **2012**, *887–888*, 128–132. <https://doi.org/10.1016/j.jchromb.2012.01.025>
- Cunha, C. E. P.; Rodrigues, E. S. B.; Alecrim, M. F.; Thomaz, D. V.; Macêdo, I. Y. L.; Garcia, L. F.; Oliveira Neto, J. R.; Moreno, E. K. G.; Ballaminut, N.; Gil, E. de S. Voltammetric Evaluation of Diclofenac Tablets Samples through Carbon Black-Based Electrodes. *Pharmaceuticals*. **2019**, *12* (2), 83. <https://doi.org/10.3390/ph12020083>
- Deepa, S.; Swamy, B. E. K.; Pai, K. P. Voltammetric detection of anticancer drug Doxorubicin at pencil graphite electrode: A voltammetric study. *Sensors International* **2020**, *1*, 100033. <https://doi.org/10.1016/j.sintl.2020.100033>
- Felix, F. S.; Angnes, L. Electrochemical immunosensors – A powerful tool for analytical applications. *Biosens. Bioelectron.* **2018**, *102*, 470–478. <https://doi.org/10.1016/j.bios.2017.11.029>
- Hahn, Y.; Lee, H. Y. Electrochemical behavior and square wave voltammetric determination of doxorubicin hydrochloride. *Arch. Pharm. Res.* **2004**, *27* (1), 31–34. <https://doi.org/10.1007/BF02980041>
- Hajian, R.; Tayebi, Z.; Shams, N. Fabrication of an electrochemical sensor for determination of doxorubicin in human plasma and its interaction with DNA. *J. Pharm. Anal.* **2017**, *7* (1), 27–33. <https://doi.org/10.1016/j.jpha.2016.07.005>
- ICH Harmonized Tripartite Guideline. Validation of analytical procedures: text and methodology (Q2) R1. Current Step 4. International Conference on Harmonization of Technical Requirements for Registration of Pharmaceuticals for Human Use. 2014. <https://database.ich.org/sites/default/files/Q2%28R1%29%20Guideline.pdf> (accessed 2021-02-28).
- Li, D.; Xu, Y.; Fan, L.; Shen, B.; Ding, X.; Yuan, R.; Li, X.; Chen, W. Target-Driven Rolling Walker Based Electrochemical Biosensor for Ultrasensitive Detection of Circulating Tumor DNA Using Doxorubicin@tetrahedron-Au Tags. *Biosens. Bioelectron.* **2020**, *148*, 111826. <https://doi.org/10.1016/j.bios.2019.111826>
- Macêdo, I. Y. L.; Alecrim, M. F.; Oliveira Neto, J. R.; Torres, I. M. S.; Thomaz, D. V.; Gil, E. S. Piroxicam voltammetric determination by ultra low cost pencil graphite electrode. *Braz. J. Pharm. Sci.* **2020**, *56*, e17344. <https://doi.org/10.1590/s2175-97902019000317344>
- Navas, N.; Herrera, A.; Martínez-Ortega, A.; Salmerón-García, A.; Cabeza, J.; Cuadros-Rodríguez, L. Quantification of an intact monoclonal antibody, rituximab, by (RP)HPLC/DAD in compliance with ICH guidelines. *Anal. Bioanal. Chem.* **2013**, *405* (29), 9351–9363. <https://doi.org/10.1007/s00216-013-7368-1>
- Piovesan, J. V.; Spinelli, A. Determination of Quercetin in a Pharmaceutical Sample by Square-Wave Voltammetry Using a Poly(vinylpyrrolidone)-Modified Carbon-Paste Electrode. *J. Braz. Chem. Soc.* **2014**, *25* (3), 517–525. <https://doi.org/10.5935/0103-5053.20140019>
- Radi, A. Anodic voltammetric assay of lansoprazole and omeprazole on a carbon paste electrode. *Pharm. Biomed. Anal.* **2003**, *31* (5), 1007–1012. [https://doi.org/10.1016/S0731-7085\(02\)00707-0](https://doi.org/10.1016/S0731-7085(02)00707-0)
- Rodrigues, E. S. B.; Macêdo, I. Y. L.; Lima, L. L. S.; Thomaz, D. V.; Cunha, C. E. P.; Oliveira, M. T.; Ballaminut, N.; Alecrim, M. F.; Carvalho, M.F.; Isecke, B. G.; Leite, K. C. S.; Machado, F. B.; Guimarães, F. F.; Menegatti, R.; Somerset, V.; Gil, E. S. Electrochemical Characterization of Central Action Tricyclic Drugs by Voltammetric Techniques and Density Functional Theory Calculations. *Pharmaceuticals* **2018**, *12* (3), 116. <https://doi.org/10.3390/ph12030116>
- Shah, M.; Bourner, L.; Ali, S.; Al-Enazy, S.; Youssef, M. M.; Fisler, M.; Rytting, E. HPLC Method Development for Quantification of Doxorubicin in Cell Culture and Placental Perfusion Media. *Separations*. **2018**, *5* (1), 9. <https://doi.org/10.3390/separations5010009>
- Shellaiah, M.; Sun, K. W. Review on Sensing Applications of Perovskite Nanomaterials. *Chemosensors*. **2020**, *8* (3), 55. <https://doi.org/10.3390/chemosensors8030055>
- Skalová, Š.; Langmaier, J.; Barek, J.; Vyskočil, V.; Navrátil, T. Doxorubicin determination using two novel voltammetric

approaches: A comparative study. *Electrochim. Acta.* **2020**, 330, 135180. <https://doi.org/10.1016/j.electacta.2019.135180>

Thomaz, D. V.; Leite, K. C. de S.; Moreno, E. K. G.; Garcia, L. F.; Alecrim, M. F.; Macêdo, I. Y. L.; Caetano, M. P.; Carvalho, M. F.; Machado, F. B.; Gil, E. de S. Electrochemical Study of Commercial Black Tea Samples. *Int. J. Electrochem. Sci.* **2018**, 13 (6), 5433–5439. <https://doi.org/10.20964/2018.06.55>

US Pharmacopeia (USP). Doxorubicin lyophilized powde. 2020. https://online.uspnf.com/uspnf/document/1_GUID-41785247-DA22-407F-B060-7182FDA4FD3A_3_en-US (accessed 2021-02-28).

Zhao, P.; Dash, A. K. A simple HPLC method using a microbore column for the analysis of doxorubicin. *J. Pharm. Biomed. Anal.* **1999**, 20 (3), 543–548. [https://doi.org/10.1016/S0731-7085\(99\)00070-9](https://doi.org/10.1016/S0731-7085(99)00070-9)

Experimental, DFT study, and *in silico* molecular docking investigations of dichlorodiphenyltrichloroethane against human estrogen receptor alpha

Tabe Ntui Ntui¹, Vincent Ndem Osabor², Peter Amba Neji¹, Michael Akomaye Akpe², John Akwagiobe Agwupuye²⁺, Stephen Adie Adalikwu³, Terkumbur Emmanuel Gber², Bitrus Hyelavalada Andrew², Uduak Ugbaja²

1. Cross River University of Technology, Faculty of Physical Sciences, Calabar, Nigeria.
2. University of Calabar-Nigeria, Department of Pure and Applied Chemistry, Calabar, Nigeria.
3. Cross River State College of Education, Akamkpa.

+Corresponding author: John Akwagiobe Agwupuye, Phone: +2348100056340, Email address: agwupuye.john@yahoo.com

ARTICLE INFO

Article history:

Received: November 09, 2021

Accepted: May 07, 2022

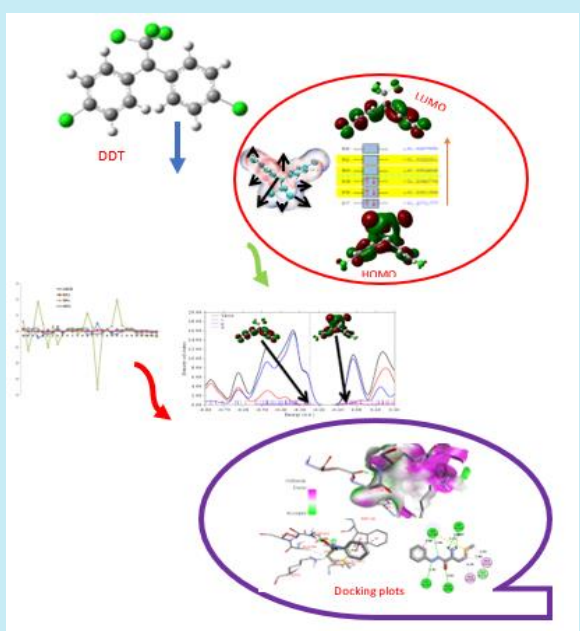
Published: July 01, 2022

Keywords

1. DFT
2. molecular docking
3. DDT
4. estrogen receptor

Section Editor: Assis Vicente Benedetti

ABSTRACT: Advanced computational tools allowed to study a pure commercial sample of dichlorodiphenyltrichloroethane (DDT) prepared in liquid phase in KBr pellets and characterized using FT-IR and GC-MS followed by the application of DDT for molecular docking against human estrogen receptor alpha. The compound was modelled using GaussView software. Using Veda 04 program, the theoretical vibrational energy distributions and experimental vibrational frequencies were compared. Interestingly, C1 and C2 possess the highest atomic charge density distribution (ACDD) of -0.284e and -0.283e while C21 and C11 have lowest ACDD of -0.064e and -0.063e in a relative manner, since the deactivating power of chlorine atoms decreases charge densities of the bonded carbon. The highest intramolecular interacting perturbation energy is 1121.92 kJ mol⁻¹ occurs between π^* C19–C21 donor orbital and π^* C14–C16 acceptor orbital while the least intramolecular interaction occurs in the lone pair of LPC26 and the sigma nonbonding (σ C1–C124) NBO orbitals with $E^{(2)}$ of 32.21 kJ mol⁻¹. Steric interaction was the only interaction found within the complex after the docking.



1. Introduction

Experimental and density functional theory (DFT) studies of the powerful insecticide dichlorodiphenyltrichloroethane (DDT), often referred to as 4', 4'-DDT have been carried out by several researchers, and studies showed that it has great impact on human health and environment in general. The DDT is one of the organochlorine pesticides (OCPs) with the potential to contaminate or pollute water and other environmental matrices due to its toxic effect on human and aquatic organisms (Buah-Kwofie *et al.*, 2018; Miao *et al.*, 2020). Notwithstanding, the persistent nature of DDT in water is due to its feeble solubility and excess half-life and the flimsy soluble nature of DDT in water results in their deposition on soil, which may either spread to the surface water or affect the groundwater. Besides, when aquatic invertebrates are subjected to DDT, it has the potential to disturb the function of the endocrine system of fishes and birds that consume them (Kowenje *et al.*, 2013; Sruthi *et al.*, 2017).

R. Zhang *et al.* (2021) studied the detoxifying mechanism of 1-chloro-4-[2, 2, 2-trichloro-1-(4-chlorophenyl) ethyl] benzene metabolized by human P450 enzymes using a combination of molecular dynamic, quantum mechanics/molecular mechanics and DFT. Their fact-findings reveals that DDT can be broken-down by P450 enzymes through the hydrogen abstraction and electrophilic addition mechanism, and the primary derivatives are epoxides (2, 3-oxide-DDT and 3, 4-oxide-DDT), DDE and dicofol. Similarly, Iramain *et al.* (2020) carried out a combine experimental (Fourier Transform Infrared (FT-IR) and Fourier Transform Raman (FT-Raman) and different DFT methodologies (B3LYP/6-31G+(d) and B3LYP/6-311++G(d, p)) studies to structurally characterized the potent insecticide dichlorodiphenyltrichloroethane (4', 4'-DDT). Furthermore, DFT technique at the Becke-86 exchange functional and LeeYang-Parr correlation functional under generalized gradient approximation methods was used in inspecting the chemiresistive detecting potential of a buckled configuration of antimonene nanotube (SbNT) towards the water pollutants-DDT and toxaphene (Bhuvanewari *et al.*, 2020).

The DFT calculations were carried out using B3LYP/6-31G (d) basic sets. The experimental and theoretical results for the vibrational frequency analysis were reported. The energies of the frontier molecular orbitals (FMOs) involving the highest occupied molecular orbital (HOMO) and the lowest unoccupied molecular orbital (LUMO) were analyzed with tabular

and graphical representation. Fukui functions, chemical reactivity descriptors, natural bond orbital (NBO), electrostatic potential, and a comparison between three population analysis; MPA, NPA and atomic dipole moment corrected Hirshfeld (ADCH) were calculated and reported to reveal the most reactive sites in the compound and its overall reactivity.

2. Methodology

2.1 Experimental method

A pure commercial sample of liquid DDT was prepared in potassium bromide (KBr) pellets and used to study experimental FT-IR spectrum using KBr disc at wavenumber region 4000-650 cm^{-1} with a CARY 630 FTIR-Agilent technology spectrophotometer and with a spectral resolution at 8 cm^{-1} . Similarly, electrospray ionization mass spectroscopy (ESI-MS) was employed for further structural determination of DDT.

2.2 Computational method

The initial structure of 1,1,1,2-tetrachloro-2,2-bis(p-chlorophenyl)ethane (DDT) was modeled using GaussView software (Fig. 1) according to the single X-ray crystal structure obtained by Hovmöller *et al.* (1978). Geometry optimization of DDT were performed using B3LYP which includes Becke's (B3) parameter exchange functional along with Lee-Yang Parr's (LYP) gradient corrected correlation functional (Lee *et al.*, 1988) using Gaussian 09 and GaussView 6.0.16 softwares (Dennington *et al.*, 2016; Frisch *et al.*, 2009). Pregeometry optimization using the molecular mechanic optimization with molecular mechanics in combination with forcefield implemented in the HyperChem program (HyperChem, 2001) has been performed on model structures and outputs used for further geometry optimization at the B3LYP/6-31+G(d,p) level of theory. Natural bond orbital analyses were calculated by the NBO 3.1 module embedded in Gaussian. In the calculation, a 6-31+G(d,p) basis set was used for the investigation, using water solvation model as an implicit approach. The QTAIM investigations and all other wavefunction analyses were conducted by Multiwfn 3.7 dev, which is a multifunctional wavefunction analysis program developed by Lu and Chen (2012). Unless otherwise specified, the default settings were used throughout these calculations. All molecular electrostatic isosurface maps were rendered by visual molecular dynamic (VMD) 1.9.3 program (Humphrey *et al.*, 1996) based on the outputs of Multiwfn analyzer.

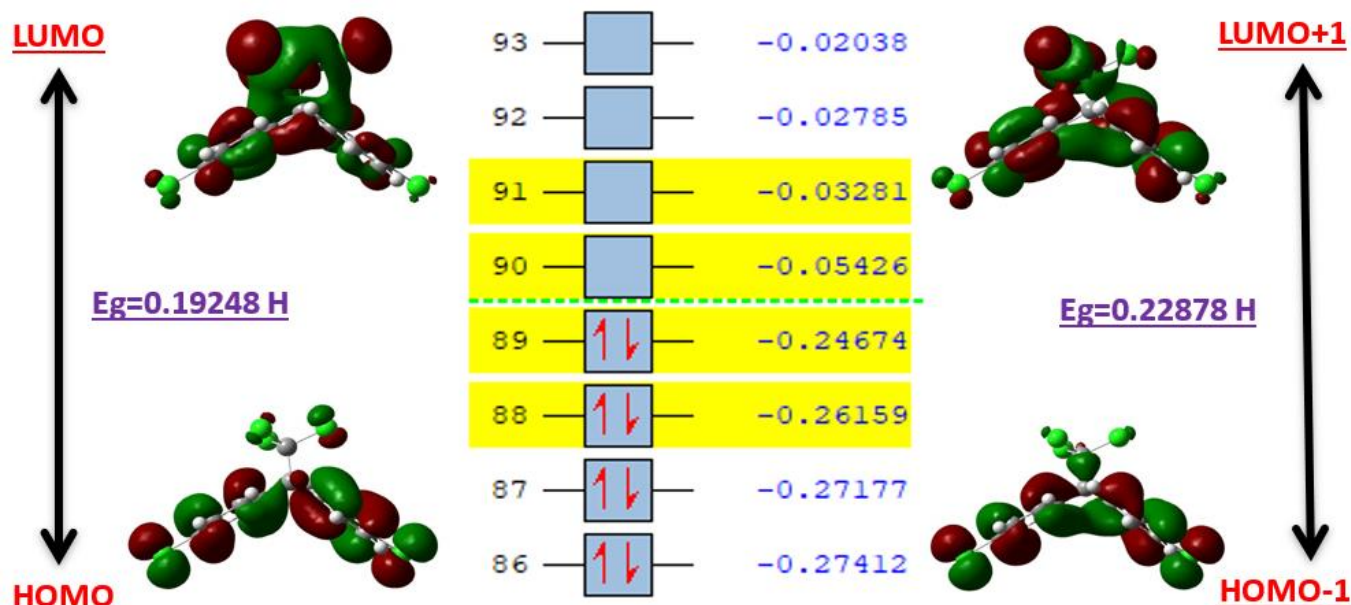


Figure 1. HOMO-LUMO of the tile molecule.

Source: Elaborated by the authors, obtained using Visual molecular dynamic (VMD) 1.9.3 program based on the outputs of Multiwfn analyzer.

3. Results and discussion

3.1 Structural analysis

3.1.1 Fourier transform infrared vibrational analysis

The vibrational modes associated with relevant and specific molecular structures of the calculated compound in question have been the main goal of the vibrational analysis. From the vibrational analysis carried out, the maximum number of possibly active noticeable fundamentals of a nonlinear molecule that contains N atoms is equal to $(3N-6)$ usual modes of vibration (Agwupuye *et al.*, 2021a). The studied compound has 36 atoms and 102 modes of vibrations. Out of the 102 modes of vibration, 35 are stretching modes, 34 are bending modes, and 33 are torsional. The DFT computed vibration wavenumber are often of much magnitude as compared to the experimentally determined wave number owing to the DFT basic set deficiencies and the combination of electron correlation effects. Hence, factors called scale factors are used to fit the DFT computed wave numbers compared to the observed ones for accurate results

fitting. The scale factor used is less than one (0.96) to reduce the overall deviation. The fundamental modes in terms of vibrational assignments associated with theoretical IR and potential energy distributions computed with the DFTB3LYP/6-311++G(d,p) method along with investigational FT-IR spectrum presented in Tab. S1 and Fig. S1 of the supporting information respectively. Few bands with weak intensity were not present in the spectra which can be confirmed by theoretically computed FT-IR intensity values.

C–Cl vibrations: The characteristic R-NH₂ vibrations for primary amines have been assigned in the region 3500–3200 cm⁻¹ (Pretsch *et al.*, 2013). Bend in primary amines results in a broadband in the range 1640–1560 cm⁻¹ (Pretsch *et al.*, 2013). The present calculations place the R-NH₂ stretching modes at 3451 and 3358 cm⁻¹ in experimental FT-IR. The H–N–H band was also observed experimentally to occur at 1640 cm⁻¹. The bands at 3516 and 3417 cm⁻¹ for R-NH₂ stretch and 1628 cm⁻¹ for N-H bond B3LYP/6-31++G(d,p) set are in good agreement with observed spectral data. These are intense stretching modes and identified from the PED in Tab. 1.

Table 1. Detailed assignments of fundamental experimental and theoretical vibrations of AATCo by normal mode analysis.

Mode No.	Experimental IR (cm ⁻¹)	Theoretical Value		I_{IR}^b	Assignments with <i>PEd</i> (%)
		Unscaled Frequency	Scaled Frequency		
1	3239	3235	3106	2.10	ν CH(98)
2	800	869	801	100.22	ν C1C(42)+ ν C1C(49)
6		3229	3100	4.10	ν CH(84)
7		3220	3091	6.28	ν CH(95)
8		3216	3087	27.29	ν CH(84)
9		3206	3078	37.66	ν_{asy} CH(88)
10		3193	3065	14.70	ν CH(89)
11		3183	3056	23.77	ν CH(88)
12		3183	3056	5.87	ν CH(88)
13		3180	3053	17.90	ν CH(97)
14	2214	2316	2223	124.98	ν_{asy} (90)+ ν CC(10)
18		1655	1589	2.85	ν CC(51)+ β HCC(20)
19		1636	1571	1.61	ν CC(53)+ β HCC(13)
20	1607	1620	1555	16.61	ν CC(53)+ β HCC(10)
21		1574	1511	35.87	ν CC(14)+ ν_{asy} CC(12)+ β' HCC(29)
22		1559	1497	283.54	ν_{asy} CC(38)+ β' HCC(29)
23		1533	1472	15.54	β HCC(52)+ β CCC(11)
31		1366	1311	1311	ν_{asy} (52)+ β HCC(18)
32		1349	1295	3.83	β HCC(56)
33		1340	1286	6.88	ν CC(39)+ β HCC(25)
37		1226	1177	49.48	ν_{asy} CC(20)+ β HCC(71)
38		1190	1142	0.79	β HCC(79)
39		1186	1139	0.35	β' HCC(84)
45		1049	1007	3.47	ν CC(46)+ β HCC(24)+ β CCC(17)
46		1032	991	0.15	β HCC(11)+ β CCC(70)
47		1015	974	0.13	ν CC(27)+ β CCC(57)
49		979	940	0.06	τ HCCC(81)
53		940	902	3.85	τ HCCC(83)
64		703	675	25.25	τ HCCC(27)+ τ HCCC(13)+ τ RCCCC(40)
65		694	666	2.87	δ CCCC(25)+ τ RCCCC(25)+ τ RCCCC(13)+ δ CCCC(15)
66	690	654	628	1.41	β CCC(63)+ β CCC(12)
67		630	605	0.12	β CCC(84)
73		534	513	21.23	β CCC(28)
81		421	404	1.41	τ HCCC(13)+ τ RCCCC(67)
82		419	402	6.33	τ RCCCC(69)
89		274	263	7.34	ν CC(19)+ β CCC(16)
96		115	110	0.83	δ CCCC(18)
97		83	80	2.98	β CCC(10)+ β CCS(10)+ β CCC(14)+ τ CCCC(10)
98		64	61	4.58	τ RCCCC(63)
99		61	59	3.30	τ RCCCC(55)+ δ CCCC(65)

ν = symmetrical stretching; ν_{asy} = asymmetrical stretching; β = in plane bending; δ = out of plane bending; τ = torsional; τR = torsional ring.

Source: Elaborated by the authors using data obtained from a CARY 630 FTIR–Agilent technology spectrophotometer and Gaussian 09/ GaussView 6.0 software.

=C–H vibrations: The C–H stretching vibration modes in the aromatic ring was observed at range 3300–3000 cm^{-1} region (Bassey *et al.*, 2022). The title compound observes =C–H stretching vibrational mode at 3239 cm^{-1} for experimental FT-IR while the computational frequency of the title compound was observed at 3106 cm^{-1} . These are intense stretching modes and identified from the PED.

C–C and C=C vibrations: The aromatic C=C and C–C stretching vibrations (aromatic ring stretching vibrations) arises in the region 1625–1400 cm^{-1} (Tadesse, 2017). In the present study, the observed C=C stretching vibrational modes of the title compound are 1607 and 1506 cm^{-1} in experimental FT-IR and also C–C stretching vibrational modes are assigned at 1297 and 1181 cm^{-1} respectively in experimental FTIR. The C–C–C the range 999–665 cm^{-1} was reported for planar vibration wave number by Saminathan *et al.* (2021). The experimental aromatic ring C–C–C bending vibrations of the title compound has appeared at 731 and 690 cm^{-1} in experimental FT-IR. The computationally calculated FT-IR for C=C stretching vibrations, C–C stretching vibrations, and aromatic ring C–C–C bending vibrations are 1602 and 1411, 1286 and 1190, 763 and 688 cm^{-1} respectively.

3.1.2 Electron spray ionization-mass spectrometry analysis

The ESI-MS is a high-speed and accurate spectroscopic technique used in the qualitative and quantitative identification of small organic molecules and the determination of their component molecular weights. The ESI-mass spectrum of DDT is presented in Fig. S1 of the supporting information, the peaks with higher intensity at m/z are 42.0, 125.0, 81.0, 152.0 and 170.0 and they correspond to the species $\text{C}_2\text{H}_4\text{N}$, $\text{C}_5\text{H}_5\text{N}_2\text{S}$, C_4HS , $\text{C}_7\text{H}_8\text{N}_2\text{S}$ and $\text{C}_{11}\text{H}_{10}\text{N}_2$. The peaks with low intensity at m/z are 53.0, 68.0, 97.0, 108.0 and 137.0. Their corresponding species are $[\text{C}_2\text{S}]^+$, C_5H_8 , $\text{C}_5\text{H}_5\text{S}$, $\text{N}_2\text{C}_4\text{S}$ and $\text{C}_6\text{H}_5\text{N}_2\text{S}$.

3.2 Frontier Molecular Orbital (FMO)

The can be linked on two important parameters in quantum chemistry—HOMO and LUMO. These parameters are very important in the analysis of the reactivity and the kinetic stability of a molecule (Agwupuye *et al.*, 2021b). Within the molecule, the electron donating capability can be seeing in the

HOMO, while the ability of an atom or molecule to accept electrons is indicated by the LUMO. The difference between these two parameters, which are HOMO and LUMO energies ($E_{\text{HOMO}} - E_{\text{LUMO}}$) match to the energy gap of the molecule. The bond gap depicts information which indicate the structure's stability and intramolecular interaction as a result of charge transfer from the donor and acceptor atom (Khalid *et al.*, 2020). Using Gauss View 6.0.16 software, the values of the E_{HOMO} , E_{LUMO} and energy gap were obtained maximizing the used with the output log file gotten from the free optimized structure. The computed FMO and global reactivity descriptors are reported in Tab. 2. Using the Multiwfn analyzer for calculating the HOMO-LUMO orbital compositions, the results revealed that the HOMO orbitals are majorly distributed within C_4 , C_{11} , C_{14} , and C_{21} ring atoms with compositions of 13.10, 10.84, 12.75, and 11.43% respectively. However, the LUMO molecular orbital compositions are primarily situated on C_1 , Cl_{25} , Cl_{24} , and Cl_{26} atoms respectively. The HOMO-LUMO molecular orbital distributions are reported in Fig. 1.

Table 2. HOMO-LUMO energy.

S/No	B3LYP/6-31+G(d)	Values
1	E_{total}	-2839.87 a.u.
2	Dipole moment	1.04 Debye
3	E_{HOMO}	-6.71 eV
4	E_{LUMO}	-1.48 eV
5	E_{gap}	5.23 eV
6	$E_{\text{HOMO}-1}$	-7.12 eV
7	$E_{\text{LUMO}+1}$	-0.89 eV
8	$E_{(\text{HOMO}-1)} - E_{(\text{LUMO}+1)}$	6.23 eV
9	μ	4.09
10	η	2.62
11	ω	3.20
12	S	0.19
13	χ	-4.09

Source: Elaborated by the authors, calculated using B3LP/6-31G(d) in Gaussian 09 software.

3.3 Natural Bond Orbital Analysis

The NBO provides a profitable technique in understanding the computational solutions of the Schrödinger equation, it also provided the convenient basis for studying the charge transfer or conjugate interaction in the molecules especially the nature of hydrogen bonding and also interaction among bonds (Agwupuye *et al.*, 2021b). This parameter is very significant in studying the interactions of donor and acceptor orbitals of molecules that enables the understanding of intra- and intermolecular bonding and

interactions. Donor occupied orbitals can interact strongly (Suresh *et al.*, 2014). Second-order perturbation Fock matrix was carried out to study the Lewis valence orbital (donor) i , non-Lewis valence orbital (acceptor) j , interactions in the NBO basis. The stabilization energy associated with the electron delocalization between Lewis (filled) and non-Lewis (unfilled) is estimated in Eq. 1 (Armaković *et al.*, 2012; Enudi *et al.*, 2021).

$$E^{(2)} = \Delta E_{i,j} = q_i \frac{F^2(i,j)}{\varepsilon_i - \varepsilon_j} \quad (1)$$

From the equation above, the donor orbital occupancy was represented by q_i the donor orbital occupancy, ε_i and ε_j represent the diagonal elements, and the Fock matrix elements were represented by $F_{(i,j)}$. The larger perturbation energy value also called the stabilization energy value $E^{(2)}$ depicts a stronger

interaction between electron donors and electron acceptors, i.e., the greater extent of conjugation of the whole system and the more donating tendency from the electron donors to electron acceptor was vividly understood by this analysis. NBO analysis of the studied structure has been performed by using the DFT/B3LYP/6-311+G(d) level of theory (Agwupuye *et al.*, 2021c) to understand clearly the charge transfer or conjugative interaction, delocalization of electron density in the molecule and energy of interaction as reported in Tab. 3. From the results, the highest intramolecular interacting perturbation energy is 1122 kJ mol⁻¹ occurring between $\pi^*C_{19} - C_{21}$ donor orbital and $\pi^*C_{14} - C_{16}$ acceptor orbital while the least intramolecular interaction is observed to occur in the lone pair of πpC_{26} and the sigma nonbonding ($\sigma C_1 - Cl_{24}$) NBO orbitals having $E^{(2)}$ energy of 32 kJ mol⁻¹.

Table 3. NBO second order perturbation energies for the studied compound.

S/NO	Donor	Acceptor	$E^{(2)}$ (kcal mol ⁻¹)	$E(i) - E(j)$	$F(i, j)$
1	$\pi^*C_{19} - C_{21}$	$\pi^*C_{14} - C_{16}$	268.21	0.01	0.094
2	$\pi^*C_9 - C_{11}$	$\pi^*C_4 - C_6$	255.27	0.01	0.084
3	$\pi^*C_{19} - C_{21}$	$\pi^*C_{15} - C_{17}$	218.48	0.01	0.800
4	$\pi^*C_9 - C_{11}$	$\pi^*C_5 - C_7$	184.74	0.01	0.079
5	$\pi^*C_{14} - C_{16}$	$\pi^*C_{19} - C_{21}$	21.57	0.27	0.069
6	$\pi^*C_{15} - C_{17}$	$\pi^*C_{19} - C_{21}$	20.49	0.27	0.067
7	$\pi^*C_{19} - C_{21}$	$\pi^*C_{15} - C_{17}$	19.58	0.30	0.068
8	$\pi^*C_{19} - C_{21}$	$\pi^*C_{14} - C_{16}$	18.99	0.30	0.067
9	πpCl_{28}	$\pi^*C_9 - C_{11}$	12.28	0.33	0.062
10	πpC_{26}	$\sigma C_1 - Cl_{24}$	7.70	0.39	0.043

Source: Elaborated by the authors, calculated using NBO 3.1 module embedded in Gaussian 09 software.

3.4 Population Analysis

DFT study of atomic charge is very important analysis in describing the distribution and location of ionic charges within the molecule thereby predicting the individual atomic reactivity. This is very relevant in many areas of studies as it stretches across the field of quantum chemistry and molecular modeling, details of electrostatic interaction with molecular force fields can also be provided by this analysis (Agwupuye *et al.*, 2021a) Using Mulliken Population Analysis (MPA), the atomic charges of the studied DDT in this present study are obtained, Hirshfeld (HPA), Atomic dipole moment corrected Hirshfeld (ADCH), and Becke (BPA) methods. The computational population result for the charge distributions for the different methods is presented in Fig. 2. It is observed that C_1 and C_2 possess the highest atomic charge density distribution of -0.284 and -0.283e while C_{21} and C_{11} are less with atomic charge distribution of -0.064 and -0.063e respectively. This is caused by the electron withdrawing power of the

chlorine atoms resulting in decreasing in charge densities of the bonded carbon.

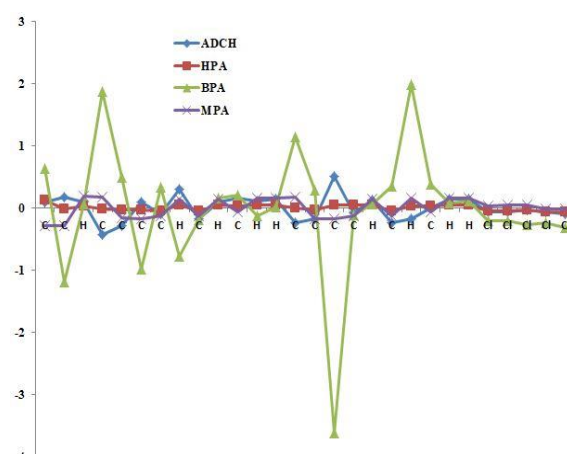


Figure 2. Population analysis plot.

Source: Elaborated by the authors, plotted using multiwfn analyzer software.

3.5 Absorption Study

The excitation type, energy, wavelength, oscillator strength, and major orbital contributions in both gas and solvents are presented in [Tabs. 4 and 5](#) respectively. The studied compound has vertical excitation energies of 5.34 and 5.37 eV with associated wavelengths of 232 and 230 nm in gas and solvents respectively. In the gas phase, the prominent intense

absorption (of 21.39% orbital contributions) arises as a result of electronic transitions from HOMO (89) → LUMO+2 (91) molecular orbital. It can also be deduced that the electron density is uniformly distributed throughout within the LUMO in the molecule, as the result of the electron withdrawing moiety it is shifted towards the LUMO and LUMO+2 transition accordingly.

Table 4. Excitation energies and oscillator strength in solvation.

Excitation type	E/eV	λ (nm)	f	Major contributions	Assignment
$S_0 \rightarrow S_1$	5.3436	232.02	0.0104	89 → 91 (21.39%)	$\pi \rightarrow \pi^*$
				86 → 92 (11.49%)	
				89 → 92 (10.05%)	
$S_0 \rightarrow S_2$	5.3601	231.31	0.0107	89 → 93 (20.00%)	$\pi \rightarrow \pi^*$
				89 → 90 (17.02%)	
				89 → 92 (10.88%)	
$S_0 \rightarrow S_3$	5.6127	220.90	0.3030	89 → 90 (71.58%)	$\pi \rightarrow \pi^*$
				89 → 93 (5.40%)	
				88 → 92 (3.15%)	
$S_0 \rightarrow S_4$	6.0123	206.22	0.1097	88 → 90 (45.09%)	$\pi \rightarrow \pi^*$
				89 → 94 (11.36%)	
				89 → 92 (11.03%)	
$S_0 \rightarrow S_5$	6.1582	201.33	0.0537	89 → 91 (26.72%)	$\pi \rightarrow \pi^*$
				85 → 90 (14.31%)	
				89 → 92 (10.08%)	

Source: Elaborated by the authors, calculated using DFT/B3LYP/6-311+G(d).

In the solvents, a similar transition is involved between HOMO → LUMO+2 molecular orbitals with an oscillator strength of 0.0207. Other LUMO orbitals having different vertical excitations in solvents are LUMO+3 and LUMO+5 having orbital contributions

of 12.66 and 12.93% respectively. For all the ground state (S_0) to the fifth singlet states (S_1), $S_0 \rightarrow S_1$ first vertical singlet states transition has the highest orbital contributions in solvents involving HOMO-2 to LUMO orbitals.

Table 5. Excitation energies and oscillator strength in solvation.

Excitation type	E/eV	λ (nm)	f	Major contributions	Assignment
$S_0 \rightarrow S_1$	5.3730	230.75	0.0207	89 → 91 (13.18%)	$\pi \rightarrow \pi^*$
				89 → 92 (12.66%)	
				89 → 94 (12.93%)	
$S_0 \rightarrow S_2$	5.3794	230.48	0.0150	87 → 90 (100.46%)	$\pi \rightarrow \pi^*$
				89 → 93 (16.56%)	
				88 → 92 (9.31%)	
$S_0 \rightarrow S_3$	5.5677	222.69	0.3205	89 → 90 (70.20%)	$\pi \rightarrow \pi^*$
				88 → 92 (4.00%)	
				89 → 94 (3.71%)	
$S_0 \rightarrow S_4$	5.9995	206.66	0.1320	88 → 90 (47.5859)	$\pi \rightarrow \pi^*$
				89 → 92 (10.30%)	
				88 → 91 (6.76%)	
$S_0 \rightarrow S_5$	6.1053	203.07	0.1008	89 → 92 (44.37%)	$\pi \rightarrow \pi^*$
				89 → 90 (10.82%)	
				89 → 92 (5.35%)	

Source: Elaborated by the authors, calculated using multiwfn software.

3.6 Molecular Electrostatic Potential

Molecular electrostatic potential diagrams are primarily used to show the electron density distribution difference in a compound. In the title molecule, electron density is evident around the DDT ring without any significant distortion. The distance of these electrons apart is also indicated as can be seen in Fig. 3.

3.7 Density of States

Density-of-state (DOS) is essentially the number of different states at a particular energy level that electrons are allowed to occupy, and it is very vital in this kind of study to appropriately characterized orbital composition by visualizing them. In the underlying curves, the plots show the different energy levels in unit energy interval at the number of molecular orbitals. Multiwfn analyzer was used in plotting the total DOS (TDOS) map for the title molecule with contribution from different sets of molecular orbitals (Fig. 4) (Liu *et al.*, 2020) and the prominent curves are denoted by the colored peaks.

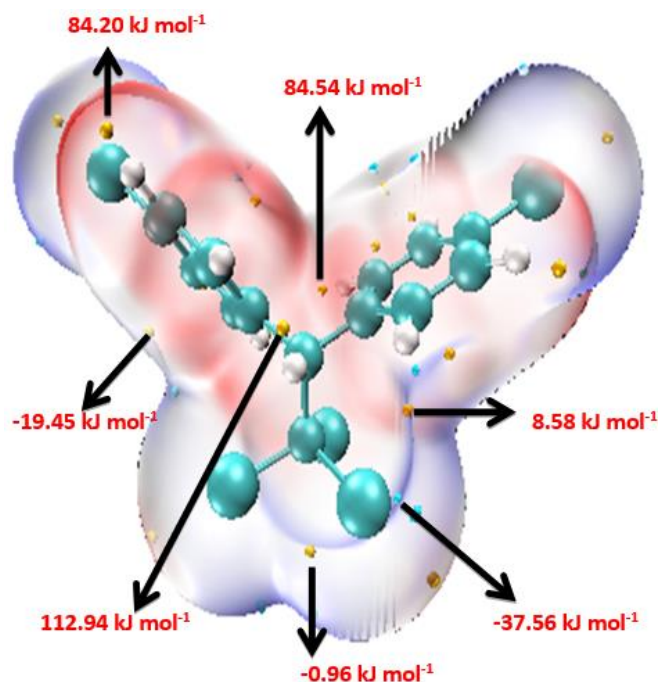


Figure 3. Molecular electrostatic potential map of the title molecule.

Source: Elaborated by the authors. Isosurface maps were rendered by visual molecular dynamic (VMD) 1.9.3 program based on the outputs of Multiwfn analyzer.

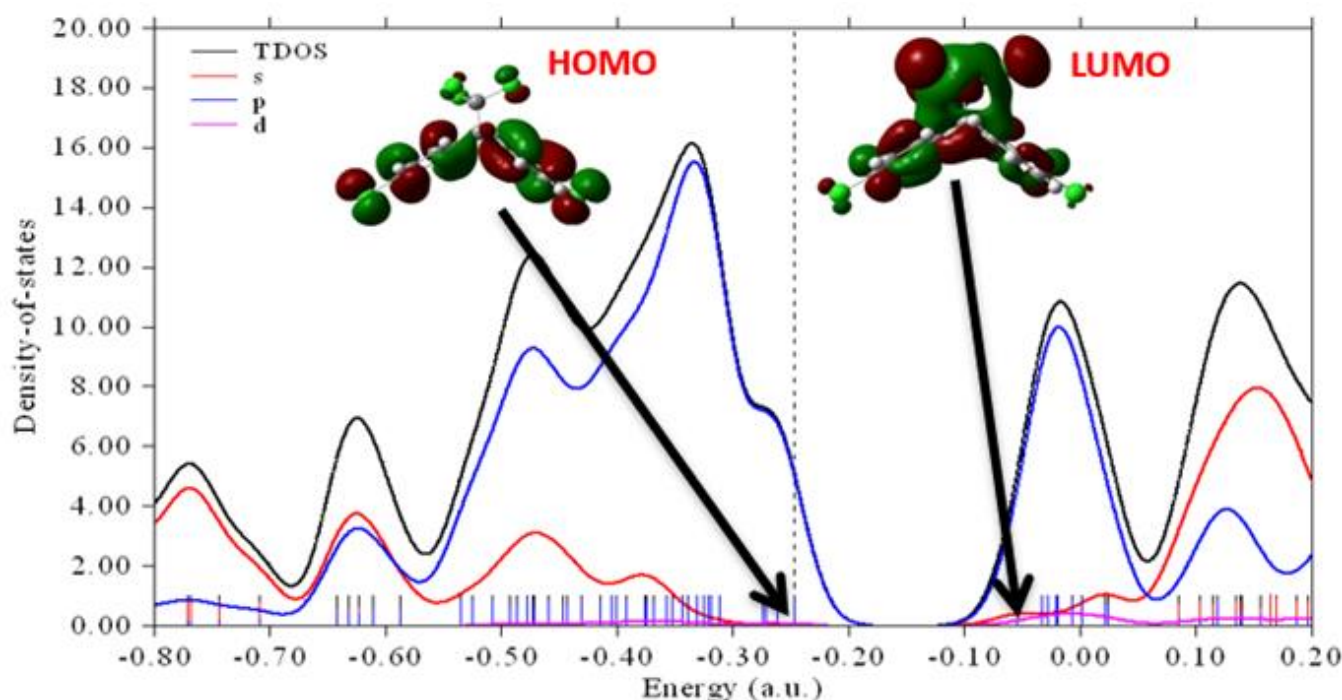


Figure 4. Density of states plot for DDT.

Source: Elaborated by the authors, plotted using Multiwfn analyzer software.

3.8 Nonlinear optics

Nonlinear response of properties like amplitude, phase, frequency and other propagation features of incident fields were clearly explained by nonlinear optics. The interaction of applied electromagnetic radiation to produce new fields from incidents one coins the term nonlinear optical effects (Ray, 2010). The growth of nonlinear optical materials has attracted important attention in fundamental and applied research. Nonlinear optical materials have vast applications in technologies such as in the design of information storage, processing of signal, switching of optical and design of optoelectronic devices in modern communication technology (Y. Zhang and Wang, 2017). Highly delocalized π – electron parts in a molecule and also high electron donors and acceptors containing organic materials are very good sources of nonlinear optical materials (Prasad and Ulrich, 2012). Taylor's series expansion of the total dipole moment, μ_{tot} induced by the field is used to present the NLO response of an isolated molecule in an electric field (ω) Eq. 2.

$$\mu_i(E_i) = \mu_i + \alpha_{ij}E_j + \frac{1}{2!}\beta_{ijk}E_jE_k + \frac{1}{3!}\gamma_{ijkl}E_jE_kE_l + \dots \quad (2)$$

where, E_i is the homogenous electric field, $\mu_i(E)$ is known as the dipole moment in an electric field, μ_i refers to dipole moments at zero field, α_{ij} , β_{ijk} , γ_{ijkl} are the polarizability tensor component, first-order hyperpolarizability component, and second-order hyperpolarizability component respectively. Using the x, y, and z components, electric dipole moment (μ) (Eq. 3) and the average polarizability (α_{tot}) (Eq. 4) can be obtained as:

$$\mu = \sqrt{(\mu_x^2 + \mu_y^2 + \mu_z^2)} \quad (3)$$

$$\alpha_{tot} = \frac{\alpha_{xx} + \alpha_{yy} + \alpha_{zz}}{3} \quad (4)$$

Anisotropy of polarizability, Eq. 5.

$$\Delta\alpha = 2^{-1/2} \left[(\alpha_{xx} - \alpha_{yy})^2 + (\alpha_{yy} - \alpha_{zz})^2 + (\alpha_{zz} - \alpha_{xx})^2 \right]^{1/2} \quad (5)$$

The first order polarizability (β_{ijk}) is a 3rd rank tensor ($3 \times 3 \times 3$ matrix). The magnitude of the first order hyperpolarizability β is calculated using the Eq. 6.

$$\beta_{tot} = \sqrt{\beta_1^2 + \beta_2^2 + \beta_3^2} \quad (6)$$

Where, beta is given by Eq. 7:

$$\beta_i = \frac{1}{3} \sum_{j=1}^3 (\beta_{ijj} + \beta_{jij} + \beta_{jji}) \quad (7)$$

$$= \sum_{j=1}^3 \beta_{ijj}$$

Here i, j = x, y, and z. and the final form resulting from Kleinman symmetry (Isborn et al, 2007).

The calculations were carried out by incorporating polar keyword and B3LYP functional and 6 – 311 + G(d) basis set and the output was loaded lurching multiwave function analyzer where the results obtained and presented in Tab. 6.

Table 6. The electric dipole moment (μ), polarizability ($\Delta\alpha$), and first order hyper polarizability (β) of reduced compound by B3LYP/6-311+G(d,p) approach and Multi wave function analyzer.

Parameter	Value
μ_x	0.355
μ_y	-0.204
μ_z	-0.002
μ_{Total}	0.410
Parameter	Value
α_{xx}	171.175
α_{xy}	11.897
α_{yy}	159.84
α_{xz}	0.811
α_{yz}	2.334
α_{zz}	255.023
α_{Total}	88.786
$\Delta\mu_{Total}$	537.319
Parameter	Value
β_{xxx}	-26.884
β_{xxy}	-11.862
β_{xyy}	-65.056
β_{yyy}	-165.703
β_{xxz}	2.624
β_{xyz}	17.599
β_{yyz}	52.314
β_{xzz}	-1355.432
β_{yzz}	-355.432
β_{zzz}	87.982
β_{Total}	597.706

Source: Elaborated by the authors, calculated using B3LYP/6-311+G(d,p) and Multiwfn analyzer.

3.9 Molecular docking studies

Molecular docking studies were carried out using human estrogen receptor alpha for human X-ray

structures (1R5K, 1ERR, 2BJ4 and 3ERT) cocrystallized with DDT. The structure of the compound was drawn using Gaussian 09 (Glendening *et al.*, 2018). The optimized structure of the compound was used in Multiwfn (Lu, 2017) to invoke the different atomic number in order to know the specific atoms that interacted with the different amino acid. The main purpose of molecular docking is to obtain an optimized conformation for each of the drug and protein with relative orientation between them such that the free energy of the overall system is minimized (Mascarenhas and Ghoshal, 2008). It is a computational tool and techniques employed in predicting and evaluating the suitability of the studied compounds as drug candidate. It is a method that analyzes the orientation and conformation of molecules into the binding site of a macromolecular target. Toward this objective, comparative molecular docking was employed to study the drug delivery of human estrogen receptor alpha for human X-ray against DDT. The receptor proteins were prepared by removing water molecules, adding explicit hydrogens, charges and correction of deformation in amino acid sequence. The active sites of the receptor protein were predicted and defined based on the interaction of the crystallographic ligand and the complexes with the receptor molecules respectively as visualized with the discovery studio visualizer. This aims at predicting the type of interactions and the docking procedure also aims to identify and recognize the correct and most favorable binding poses within the binding site of the studied protein (Pagadala *et al.*, 2017). From these docking results hydrogen bonding was not the only bonding type that exists in the studied compounds, other

interaction like unfavorable Donor–Donor bond, pi cation, pi sigma, pi alkyl, salt bridge and other as can be seen in 2D and 3D plots. However, for each receptor interaction with DDT the highest pose was recorded as -34 , -26 , -25 and -32 kJ mol⁻¹ for 1ERR-DDT, 1R5K-DDT, 2BJ4-DDT and 3ERT respectively. These interactions are shown in Fig. 5a and 5b from this docking result, it can be seen that DDT interaction with 1ERR has the highest binding affinity compared to other receptors. The 3D structure of the hER α within the receptor backbone is presented in Fig. 5b. This steric effect that was observed in the docking result is due to the constituent atoms that make up the molecule occupy some degree of space, and when atoms come too close together there's a rise in the energy of the molecule due to the atoms being forced to occupy the same physical space. This explains why steric effect can have a dramatic effect on the observed or preferred shape of a molecule and in some cases even its chemical reactivity (Barnes, 2019; Yang *et al.*, 2010).

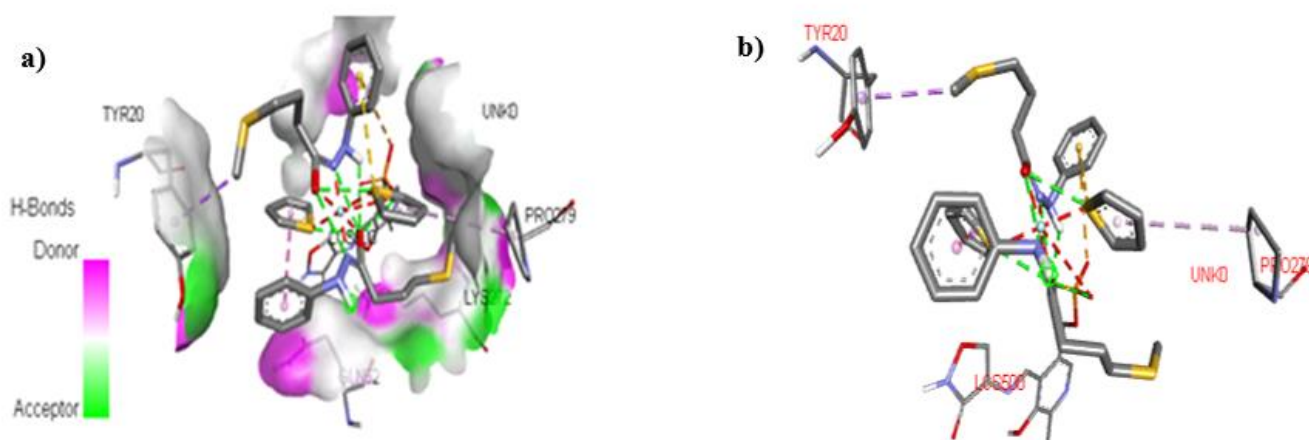
The docking results of the DDT 1ERR, 1R5K, 2BJ4 and 3ERT as well as the root mean square distance in reference to the first mode are presented in Tab. 7.

Table 7. Binding affinities and root mean square distance of the docking score.

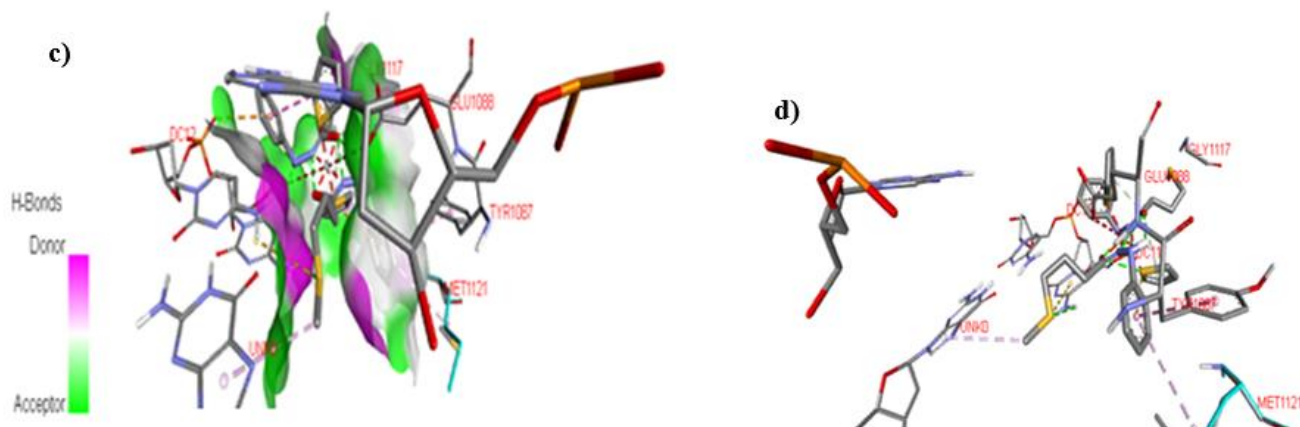
Receptors	Binding affinity (kJ mol ⁻¹)	Rmsd (l.b)	Rmsd (u.b)
1ERR	-33.9	2.448	5.061
1R5K	-25.9	2.122	3.872
2BJ4	-25.1	1.169	5.252
3ERT	-32.2	1.297	4.858

Source: Elaborated by the authors, calculated using autoDoc Vina tools.

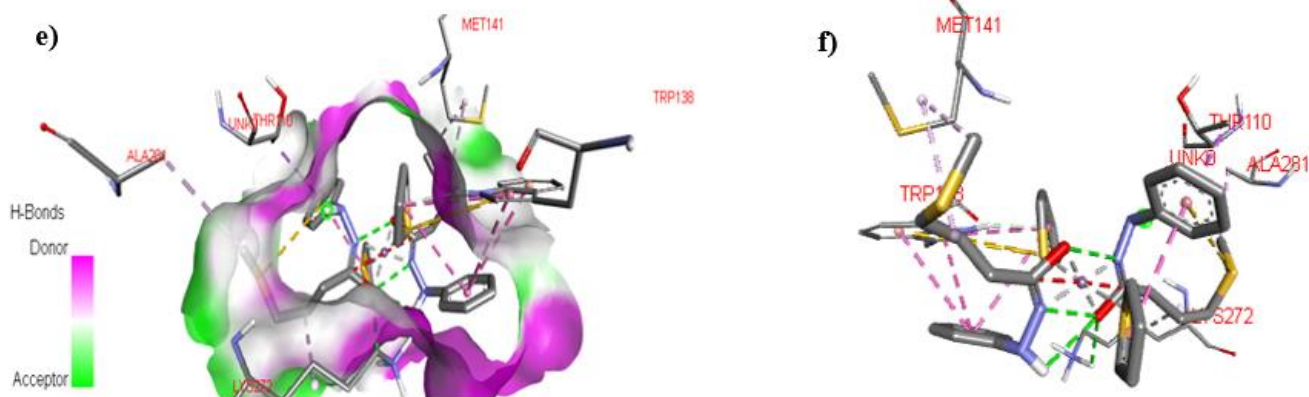
Human estrogen receptor; 1r5k interaction with DDT



Human estrogen receptor; 1err interaction with DDT



Human estrogen receptor; 2bj4 interaction with DDT



Human estrogen receptor; 3ert interaction with DDT

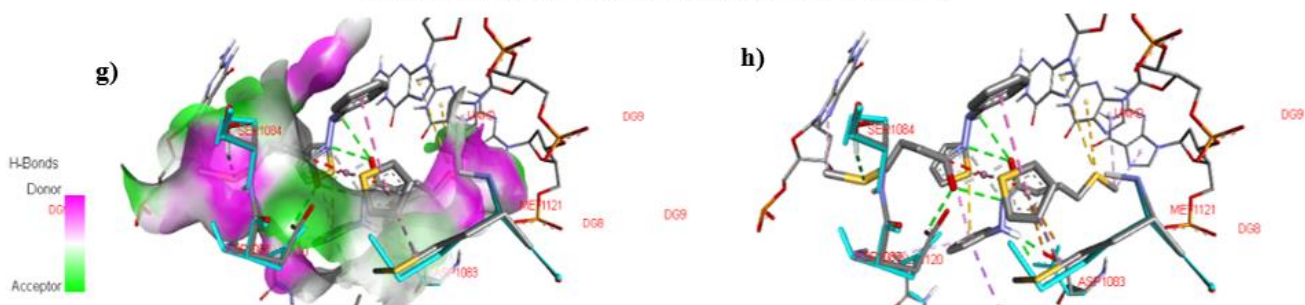


Figure 5. Showing 3D, steric interactions and other forms of interaction of the human estrogen receptor alpha X-ray structures as cocrystallized with DDT.

Source: Elaborated by the authors, Generated using AutoDoc Vina tools.

4. Conclusions

High level quantum computational tools were used to study a pure commercial sample of DDT prepared in liquid phase in KBr pellets and characterized using FT-IR and GC-MS followed by the application of the title molecule for molecular docking against human estrogen receptor alpha (hER α). Using water model as

an implicit approach, the high calculations were computed using a 6 – 31 + G(d,p) basic set. The fundamental modes in terms of vibrational assignments associated with theoretical IR and potential energy distributions were computed by the use the DFT-B3LYP/6-311++G(d,p) basic sets along with experimental FT-IR spectrum. It was observed that bands with weak intensity were not existing in the

spectra, and this was confirmed with theoretically calculated FT-IR intensity values. Using Multiwfn analyzer for calculating the HOMO-LUMO orbital compositions, the results revealed that the HOMO orbitals are majorly distributed within C₄, C₁₁, C₁₄, and C₂₁ ring atoms with compositions of 13.10, 10.84, 12.75, and 11.43% respectively. However, the LUMO molecular orbital compositions are primarily situated on C₁, Cl₂₅, Cl₂₄, and Cl₂₆ atoms respectively. From the NBO result, the highest intramolecular interacting perturbation energy is 1122 kJ/mol occurring between $\pi^*C_{19} - C_{21}$ donor orbital and $\pi^*C_{14} - C_{16}$ acceptor orbital while the least intramolecular interaction is observed to occur in the lone pair of electron from πC_{26} and the sigma nonbonding ($\sigma C_1 - Cl_{24}$) NBO orbitals having $E^{(2)}$ energy of 32 kJ/mol. ADCH analysis shows that C₁ and C₂ possess the highest atomic charge density distribution of -0.284 and -0.283e while C₂₁ and C₁₁ are less with atomic charge distribution of -0.064 and -0.063e accordingly. The electron withdrawing power of chlorine atoms in the molecules was observed to be the cause of this changes resulting in decreasing in charge densities of the bonded carbon. And in the adsorption studies, all the ground state (S₀) to the fifth singlet states (S₁), S₀→S₁ first vertical singlet states transition has the highest orbital contributions in solvents involving HOMO-2 to LUMO orbitals. While in the molecular docking studies, steric interaction was the only observable interaction that was found within the complex after the docking however, there were no observable hydrogen interactions between the drug (DDT) and any of the hER α , which would have been the bases for determining the drug activeness with the receptors.

Authors' contribution

Conceptualization: Tabe N. Ntui, John A. Agwupuye, Terkumbur E. Gber

Data curation: Stephen A. Adalikwu, Michael A. Akpe

Formal Analysis: John A. Agwupuye

Funding acquisition: Uduak Ugbaja, Tabe N. Ntui, Michael A. Akpe

Investigation: Bitrus H Andrew, Terkumbur E. Gber, John A. Agwupuye

Methodology: John A. Agwupuye, Tabe N. Ntui

Project administration: Vincent N. Osabor, Peter A. Neji, John A. Agwupuye

Resources: Michael A. Akpe, Stephen A. Adalikwu.

Software: Terkumbur E. Gber, John A. Agwupuye

Supervision: Tabe N. Ntui, Vincent N. Osabor, Peter A. Neji

Validation: John A. Agwupuye, Terkumbur E. Gber

Visualization: John A. Agwupuye

Writing – original draft: Terkumbur E. Gber

Writing – review & editing: John A. Agwupuye

Data availability statement

GC-MS, FT-IR analysis was carried at Central Laboratory at Usman Dan Fodio University, Sokoto – Nigeria and the DFT analysis was conducted using Gaussian 09, GaussView 6.0.16, and multiwfn 3.7 softwares.

Funding

Not applicable.

Acknowledgments

Taba Ntui is very thankful to his Supervisor, Dr. Peter Neji and Hitler Louis for his immense support and contributions.










References

- Agwupuye, J. A.; Louis, H.; Enudi, O. C.; Unimuke, T. O.; Edim, M. M. Theoretical insight into electronic and molecular properties of halogenated (F, Cl, Br) and heteroatom (N, O, S) doped cyclooctane. *Mater. Chem. Phys.* **2021a**, *275*, 125239. <https://doi.org/10.1016/j.matchemphys.2021.125239>
- Agwupuye, J. A.; Louis, H.; Unimuke, T. O.; David, P.; Ubana, E. I.; Moshood, Y. L. Electronic structure investigation of the stability, reactivity, NBO analysis, thermodynamics, and the nature of the interactions in methyl-substituted imidazolium-based ionic liquids. *J. Mol. Liq.* **2021b**, *337*, 116458. <https://doi.org/10.1016/j.molliq.2021.116458>
- Agwupuye, J. A.; Neji, P. A.; Louis, H.; Odey, J. O.; Unimuke, T. O.; Bisiong, E. A.; Ntui, T. N. Investigation on electronic structure, vibrational spectra, NBO analysis, and molecular docking studies of aflatoxins and selected emerging mycotoxins against wild-type androgen receptor. *Heliyon.* **2021c**, *7* (7), e07544. <https://doi.org/10.1016/j.heliyon.2021.e07544>
- Armaković, S.; Armaković, S. J.; Šetrajčić, J. P.; Šetrajčić, I. J. Active components of frequently used β -blockers from the

- aspect of computational study. *J. Mol. Model.* **2012**, *18* (9), 4491–4501. <https://doi.org/10.1007/s00894-012-1457-5>
- Barnes K. *What is the Steric Effect in Organic Chemistry? - Definition & Examples*. Study.com. 2019. <https://study.com/academy/lesson/what-is-the-steric-effect-in-organic-chemistry-definition-examples.html#:~:text=The%20steric%20effect%20is%20when,occupy%20the%20same%20physical%20space> (accessed 2022-06-26).
- Bassey, V. M.; Apebende, C. G.; Idante, P. S.; Louis, H.; Emori, W.; Cheng, C. R.; Asogwa, F. C. Vibrational characterization and molecular electronic investigations of 2-acetyl-5-methylfuran using FT-IR, FT-Raman, UV-VIS, NMR, and DFT methods. *J. Fluoresc.* **2022**, *32* (3), 1005–1017. <https://doi.org/10.1007/s10895-022-02903-8>
- Bhuvanawari, R.; Nagarajan, V.; Chandiramouli, R. Sensing studies of DDT and Toxaphene molecules using chemi-resistive β -antimonene nanotubes based on first-principles insights. *Chem. Phys. Lett.* **2020**, *757*, 137895. <https://doi.org/10.1016/j.cplett.2020.137895>
- Buah-Kwofie, A.; Humphries, M. S.; Pillay, L. Bioaccumulation and risk assessment of organochlorine pesticides in fish from a global biodiversity hotspot: iSimangaliso Wetland Park, South Africa. *Sci. Total Environ.* **2018**, *621*, 273–281. <https://doi.org/10.1016/j.scitotenv.2017.11.212>
- Dennington, R.; Keith, T. A.; Millam, J. M. GaussView 6.0. 16. Semichem Inc.: Shawnee Mission, KS, USA. 2016.
- Enudi, O. C.; Louis, H.; Edim, M. M.; Agwupuye, J. A.; Ekpen, F. O.; Bisong, E. A.; Utsu, P. M. Understanding the aqueous chemistry of quinoline and the diazanaphthalenes: insight from DFT study. *Heliyon.* **2021**, *7* (7), e07531. <https://doi.org/10.1016/j.heliyon.2021.e07531>
- Frisch, M. J.; Trucks, G. W.; Schlegel, H. B.; Scuseria, G. E.; Robb, M. A.; Cheeseman, J. R.; Scalmani, G.; Barone, V.; Mennucci, B.; Petersson, G. A.; Nakatsuji, H.; Caricato, M.; Li, X.; Hratchian, H. P.; Izmaylov, A. F.; Bloino, J.; Zheng, G.; Sonnenberg, J. L.; Hada, M.; Ehara, M.; Toyota, K.; Fukuda, R.; Hasegawa, J.; Ishida, M.; Nakajima, T.; Honda, Y.; Kitao, O.; Nakai, H.; Vreven, T.; Montgomery Jr., J. A.; Peralta, J. E.; Ogliaro, F.; Bearpark, M.; Heyd, J. J.; Brothers, E.; Kudin, K. N.; Staroverov, V. N.; Kobayashi, R.; Normand, J.; Raghavachari, K.; Rendell, A.; Burant, J. C.; Iyengar, S. S.; Tomasi, J.; Cossi, M.; Rega, N.; Millam, J. M.; Klene, M.; Knox, J. E.; Cross, J. B.; Bakken, V.; Adamo, C.; Jaramillo, J.; Gomperts, R.; Stratmann, R. E.; Yazyev, O.; Austin, A. J.; Cammi, R.; Pomelli, C.; Ochterski, J. W.; Martin, R. L.; Morokuma, K.; Zakrzewski, V. G.; Voth, G. A.; Salvador, P.; Dannenberg, J. J.; Dapprich, S.; Daniels, A. D.; Farkas, Ö.; Foresman, J. B.; Ortiz, J. V.; Cioslowski, J.; Fox, D. J. Gaussian 09 (Gaussian, Inc., Wallingford CT, 2009).
- Glendening, E. D.; Badenhop, J. K.; Reed, A. E.; Carpenter, J. E.; Bohmann, J. A.; Morales, C. M.; Karafiloglou, P.; Landis, C. R.; Weinhold, F. *NBO 7.0*, Theoretical Chemistry Institute, University of Wisconsin, Madison, 2018. https://nbo7.chem.wisc.edu/biblio_css.htm (accessed 2022-06-26).
- Hovmöller, S.; Smith, G.; Kennard, C. H. L. Structural Studies of Polychlorinated Hydrocarbons. V. 1, 1, 1, 2-Tetrachloro-2, 2-bis (*p*-chlorophenyl) ethane and 1, 1, 1-Tribromo-2, 2-bis (*p*-chlorophenyl) ethane. *Acta Cryst.* **1978**, *B34* (10), 3016–3021. <https://doi.org/10.1107/S0567740878009942>
- Humphrey, W.; Dalke, A.; Schulten, K. VMD: visual molecular dynamics. *J. Mol. Graph.* **1996**, *14* (1), 33–38. [https://doi.org/10.1016/0263-7855\(96\)00018-5](https://doi.org/10.1016/0263-7855(96)00018-5)
- HyperChem, T. HyperChem 8.07, HyperChem Professional Program. Gainesville, Hypercube. 2001.
- Iramain, M. A.; Castillo, M. V.; Davies, L.; Manzur, M. E.; Brandan, S. A. Structural and SQMFF study of potent insecticide 4', 4'-DDT combining the FT-IR and FT-Raman spectra with DFT calculations. *J. Mol. Struct.* **2020**, *1199*, 126964. <https://doi.org/10.1016/j.molstruc.2019.126964>
- Isborn, C. M.; Leclercq, A.; Vila, F. D.; Dalton, J. L.; Brédas, L. R.; Eichinger, B. E.; Robinson, B. H. Comparison of static first hyperpolarizabilities calculated with various quantum mechanical methods. *J. Phys. Chem. A.* **2007**, *111* (7) 1319–1327. <https://doi.org/10.1021/jp064096g>
- Khalid, M.; Ali, A.; Adeel, M.; Din, Z. U.; Tahir, M. N.; Rodrigues-Filho, E.; Khan, M. U. Facile preparation, characterization, SC-XRD and DFT/DTDFT study of diversely functionalized unsymmetrical bis-aryl- α , β -unsaturated ketone derivatives. *J. Mol. Struct.* **2020**, *1206*, 127755. <https://doi.org/10.1016/j.molstruc.2020.127755>
- Kowenje, C. O.; Osewe, E. T.; Lalah, J. O. Effects of faujasite X and Y zeolites on the 1,1,1-trichloro-2, 2'bis (*p*-chlorophenyl) ethane (DDT) degradation during water purification. *Int. J. Environ. Pollut.* **2013**, *1* (1), 9–15. <https://doi.org/10.11648/j.ijep.20130101.12>
- Lee, C.; Yang, W.; Parr, R. G. Development of the colle-salveti correlation energy formula into a functional of the electron density. *Phys. Rev. B.* **1988**, *37* (2), 785–789. <https://doi.org/10.1103/PhysRevB.37.785>
- Liu, Z.; Lu, T.; Chen, Q. An sp-hybridized all-carboatomic ring, cyclo[18]carbon: Electronic structure, electronic spectrum, and optical nonlinearity. *Carbon* **2020**, *165*, 461–467. <https://doi.org/10.1016/j.carbon.2020.05.023>
- Lu, T.; Chen, F. Multiwfn: a multifunctional wavefunction analyzer. *J. Comput. Chem.* **2012**, *33* (5), 580–592. <https://doi.org/10.1002/jcc.22885>
- Lu, T. *Multiwfn (a multifunctional wavefunction analyzer), software manual*. Beijing Kein Research Center for Natural Sciences; Version 3.4, 2017. https://web.mit.edu/multiwfn_v3.4/Manual_3.4.pdf (accessed 2022-06-26).

- Mascarenhas, N. M.; Ghoshal, N. An efficient tool for identifying inhibitors based on 3D-QSAR and docking using feature-shape pharmacophore of biologically active conformation—A case study with CDK2/CyclinA. *Eur. J. Med. Chem.* **2008**, *43* (12), 2807–2818. <https://doi.org/10.1016/j.ejmech.2007.10.016>
- Miao, J.; Liu, A.; Wu, L.; Yu, M.; Wei, W.; Liu, S. Magnetic ferroferric oxide and polydopamine molecularly imprinted polymer nanocomposites based electrochemical impedance sensor for the selective separation and sensitive determination of dichlorodiphenyltrichloroethane (DDT). *Anal. Chim. Acta.* **2020**, *1095*, 82–92. <https://doi.org/10.1016/j.aca.2019.10.027>
- Pagadala, N. S.; Syed, K.; Tuszynski, J. Software for molecular docking: a review. *Biophys. Rev.* **2017**, *9* (2), 91–102. <https://doi.org/10.1007/s12551-016-0247-1>
- Prasad, P. N.; Ulrich, D. R. *Nonlinear optical and electroactive polymers*. Springer Science & Business Media, 2012.
- Pretsch, E.; Clerc, T.; Seibl, J.; Simon, W. *Tables of spectral data for structure determination of organic compounds*. Springer Science & Business Media, 2013.
- Ray, P. C. Size and shape dependent second order nonlinear optical properties of nanomaterials and their application in biological and chemical sensing. *Chem. Rev.* **2010**, *110* (9), 5332–5365. <https://doi.org/10.1021/cr900335q>
- Saminathan, M.; Jayakumar, M. R.; Chandrasekaran, R.; Raja, R.; George, J.; Alagusundaram, P. Synthesis, spectral, crystal structure, drug-likeness, in silico and in vitro biological screening of halogen [Cl, Br] substituted *N*-Phenylbenzo [g] indazole derivatives as antimicrobial agents. *J. Heterocycl. Chem.* **2021**, *58* (3), 841–863. <https://doi.org/10.1002/jhet.4219>
- Sruthi, S. N.; Shyleshchandran, M. S.; Mathew, S. P.; Ramasamy, E. V. Contamination from organochlorine pesticides (OCPs) in agricultural soils of Kuttanad agroecosystem in India and related potential health risk. *Environ. Sci. Pollut. Res.* **2017**, *24* (1), 969–978. <https://doi.org/10.1007/s11356-016-7834-3>
- Suresh, S.; Gunasekaran, S.; Srinivasan, S. Spectroscopic (FT-IR, FT-Raman, NMR and UV–Visible) and quantum chemical studies of molecular geometry, Frontier molecular orbital, NLO/NBO and thermodynamic properties of salicylic acid. *Spectrochim. Acta A Mol. Biomol. Spectrosc.* **2014**, *132*, 130–141. <https://doi.org/10.1016/j.saa.2014.04.174>
- Tadesse, T. Quantum Mechanical Study on the Effect of Solvent in the Properties of Benzophenone. *J. Phys. Chem. Biophys.* **2017**, *7* (4) 1000259. <https://doi.org/10.4172/2161-0398.1000259>
- Yang, W. H.; Wang, Z. Y.; Liu, H. L.; Yu, H. X. Exploring the binding features of polybrominated diphenyl ethers as estrogen receptor antagonists: docking studies. *SAR QSAR Environ. Res.* **2010**, *21* (3–4), 351–367. <https://doi.org/10.1080/10629361003773971>
- Zhang, Y.-x.; Wang, Y.-h. Nonlinear optical properties of metal nanoparticles: a review. *RSC Adv.* **2017**, *7* (71), 45129–45144. <https://doi.org/10.1039/C7RA07551K>
- Zhang, R.; Li, P.; Zhang, R.; Shi, X.; Li, Y.; Zhang, Q.; Wang, W. Computational study on the detoxifying mechanism of DDT metabolized by cytochrome P450 enzymes. *J. Hazard. Mater.* **2021**, *414*, 125457. <https://doi.org/10.1016/j.jhazmat.2021.125457>

Experimental, DFT study, and *in silico* molecular docking investigations of dichlorodiphenyltrichloroethane against human estrogen receptor alpha

Tabe Ntui Ntui¹, Vincent Ndem Osabor², Peter Amba Neji¹, Michael Akomaye Akpe², John Akwagiobe Agwupuye²⁺, Stephen Adie Adaliku³, Terkumbur Emmanuel Gber², Bitrus Hyelavalada Andrew², Uduak Ugbaja²

1. Cross River University of Technology, Faculty of Physical Sciences, Calabar, Nigeria.
2. University of Calabar-Nigeria, Department of Pure and Applied Chemistry, Calabar, Nigeria.
3. Cross River State College of Education, Akamkpa.

+Corresponding author: John Akwagiobe Agwupuye, **Phone:** +2348100056340, **Email address:** agwupuye.john@yahoo.com

ARTICLE INFO

Article history:

Received: November 09, 2021

Accepted: May 07, 2022

Published: July 01, 2022

Keywords

1. DFT
2. molecular docking
3. DDT
4. estrogen receptor

Section Editor: Assis Vicente Benedetti

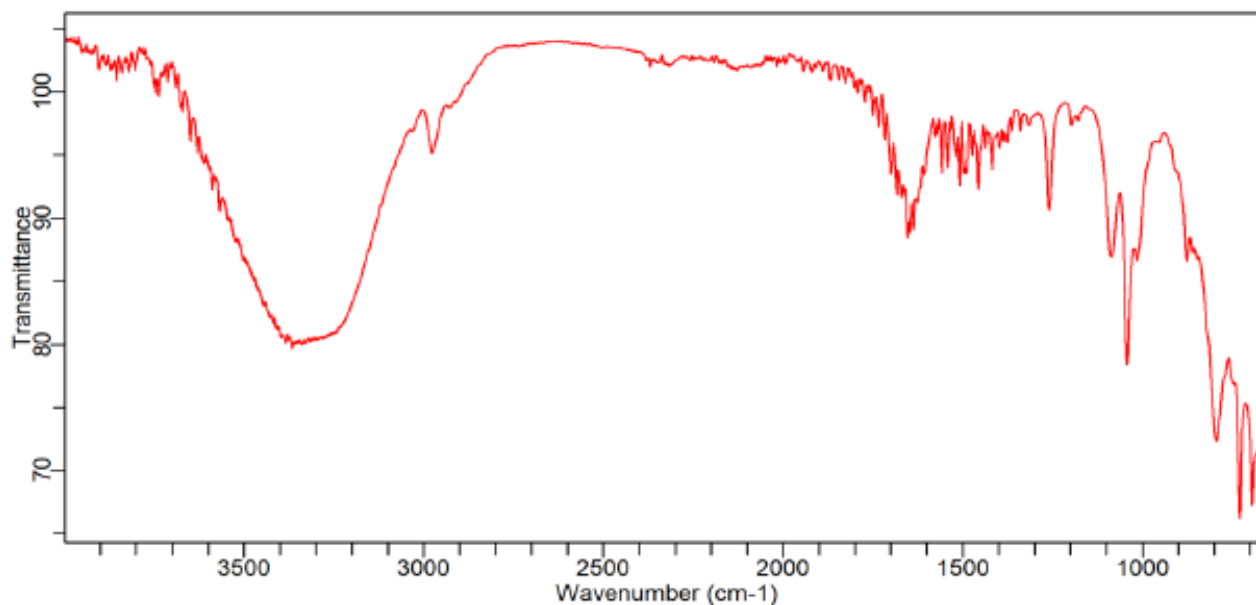


Figure S1. The ESI-Mass spectrum of dichlorodiphenyltrichloroethane (DDT).

Table S1. ADCH, HPA, BPA and MPA result of DDT.

Atoms	ADCH	HPA	BPA	MPA
C	0.0957	0.1321	0.6365	-0.2842
C	0.1777	-0.0175	-1.1844	-0.2833
H	0.0929	0.0392	0.0717	0.1909
C	-0.4344	-0.0101	1.8669	0.1801
C	-0.2849	-0.0315	0.4992	-0.1513
C	0.1021	-0.0369	-0.9841	-0.1694
C	-0.0902	-0.0414	0.3357	-0.1334
H	0.3078	0.0409	-0.7734	0.1491
C	-0.1675	-0.0429	-0.1831	-0.1292
H	0.1019	0.0435	0.1667	0.1465
C	0.1569	0.0293	0.2059	-0.0629
H	0.1153	0.0531	-0.1346	0.1607
H	0.1457	0.0531	0.0220	0.1602
C	-0.2301	-0.0048	1.1507	0.1756
C	-0.1779	-0.0341	0.2824	-0.1718
C	0.5055	0.0408	-3.6223	-0.1747
C	-0.0821	0.0409	-0.1093	-0.1254
H	0.1251	0.0479	0.0671	0.1417
C	-0.2409	-0.0407	0.3509	-0.1330
H	-0.1773	0.0332	1.9935	0.1603
C	0.0014	0.0278	0.3894	-0.0635
H	0.1409	0.0536	0.0787	0.1607
H	0.1367	0.0532	0.1088	0.1611
Cl	-0.0631	-0.0517	-0.2071	0.0373
Cl	-0.0569	-0.0520	-0.2055	0.0475
Cl	-0.0343	-0.0332	-0.2737	0.0418
Cl	-0.0664	-0.0619	-0.2387	-0.0157
Cl	-0.0971	-0.0616	-0.3100	-0.0157

On-site weld quality assessment and qualification for stainless steels tanks

Luis Henrique Guilherme^{1,2+id}, Cecilio Sadao Fugivara^{3id}, Assis Vicente Benedetti^{3id}

1. Soudap Soldas Sanitárias, Engineering Department, Araraquara, Brazil.
2. ACW Engineering, Research & Development Department, Araraquara, Brazil.
3. São Paulo State University, Institute of Chemistry, Araraquara, Brazil.

+Corresponding author: Luis Henrique Guilherme, **Phone:** +55 16 997650040, **Email address:** lh.guilherme@soudap.com.br

ARTICLE INFO

Article history:

Received: November 09, 2021

Accepted: May 07, 2022

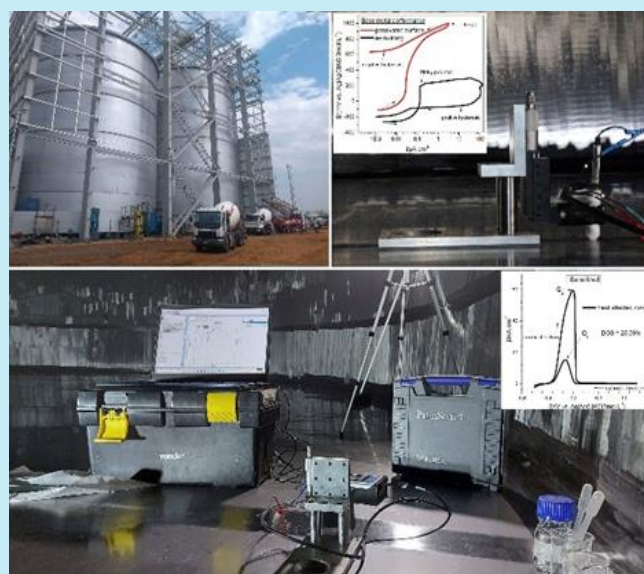
Published: July 01, 2022

Section Editor: Paulo Clairmont Feitosa Lima Gomes

Keywords

1. 2101 lean duplex stainless steel
2. on-site corrosion tests
3. cyclic polarization
4. chemical passivation treatment
5. sensitized weld

ABSTRACT: Stainless steel tanks are frequently degraded by localized corrosion in bioprocess industries. A case study of 2101 duplex stainless steel tank allowed to apply a portable electrochemical microcell system (PassivityScan) for *on-site* weld inspection and corrosion monitoring from the manufacturing until 12 months of operation. During the tank manufacturing, the double loop electrochemical potentiokinetic reactivation technique was applied to measure the sensitization degree on the welded regions. The manufactured tank was submitted to the passivation treatment to improve the passivation properties and corrosion resistance. *On-site* cyclic polarization tests were performed and confirmed the increase of passivation level of treated surface. The passivation level was measured again after 12 months of operation and detected a lower passivation level compared to the initial passivated surface, indicating that the passivation treatment lost its effect after that period. Therefore, an acceptance criterion to passivation level was empirically determined. PassivityScan is an advanced device to qualify the welds and the passivated surfaces, and useful for corrosion monitoring and the reliability maintenance.



1. Introduction

Stainless steel is widely used to build the bioprocessing equipment and facilities due to its natural capacity to generate and recover a passive film on the surface, characterized as a thin layer of chromium oxide (Cr_2O_3) that becomes the steel surface with high electrical resistance, almost inert and then, adequate to aseptic and anticorrosive applications. The electrical resistance of the passive film is dependent on the steel chemical composition and particularly on the content of chromium (Cr), molybdenum (Mo) and nickel (Ni). Besides the chemical composition, the stainless steel grade to be selected must consider the characteristic of the particular industrial process. The most used stainless steels in bioprocessing applications are from austenitic (304L and 316L) and duplex (2205, 2101 and 2304) groups, because they have showed adequate performance in processes in which hygienic characteristic and anticorrosive properties are required (Guilherme *et al.*, 2022).

The American Society of Mechanical Engineers: Bioprocessing Equipment (ASME BPE, 2019) standard aims to define requirements to the project and construction of the equipment and facilities to the bioprocessing industry, such as pharma and life science, food grade products, as well as any industrial sector where high level of hygienic and asepsis requirements are established. The welding process, the surface finishing and the chemical passivation treatment are considered by ASME BPE as special processes to obtain a hygienic surface and, therefore, the standard has specific requirements to each process.

In the field of welding, the ASME BPE defines physical and metallurgical requirements to achieve an aseptic and corrosion resistant welded joint. The equipment design needs to specify the average roughness (R_a) of the surface finishing, which can be obtained by mechanically polishing or electropolishing processes. The surface in contact with the aseptic product also needs to be submitted to the chemical passivation treatment because this procedure removes the impurities and contaminants from the surface, providing a passive film with high corrosion resistance.

The ASME BPE recommends the use of electrochemical techniques to field services as an *in situ* advanced inspection, being specifically suggested the application of the electrochemical impedance spectroscopy (EIS) to assess the rouge contamination and the cyclic potentiodynamic polarization (CPP) to

assess the level of surface passivation. However, the ASME BPE mentions that the development of an electrochemical tool to *in situ* services is still ongoing. On the other hand, recent works (Guilherme *et al.*, 2019a; 2021a; b; c; d) have showed a portable electrochemical microcell, named PassivityScan, that can apply electrochemical techniques in *on-site* surface inspection of the tanks and pipelines.

This work aims at showing the results obtained by PassivityScan in advanced *on-site* inspection and how it is useful to the reliability maintenance. For this purpose, results from *on-site* metallurgical integrity and passivation properties inspections are presented and discussed. It is important to highlight that the *on-site* surface inspections were performed in three steps of the tank life cycle: as built, after chemical passivation treatment and after 12 uninterrupted months of operation.

2. Study of case

The study of case shows the results of the *on-site* inspection of an aseptic stainless steel tank where advanced electrochemical techniques were applied. The inspections were made in the following steps of the tank life cycle as built, after surface chemical passivation and after 12 uninterrupted months of operation. The LDX 2101 lean duplex was used as base metal to construct the tank that was designed to storage NFC orange juice in an industrial cold chamber that works at around 1–3 °C. Figure 1 shows a general view of the tanks during its manufacturing and the tank inside view regarding the bottom plate and inner wall that were the objective of the surface inspections.



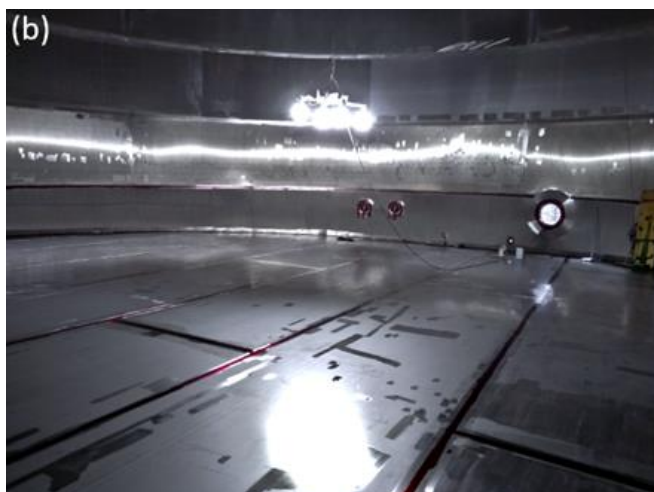


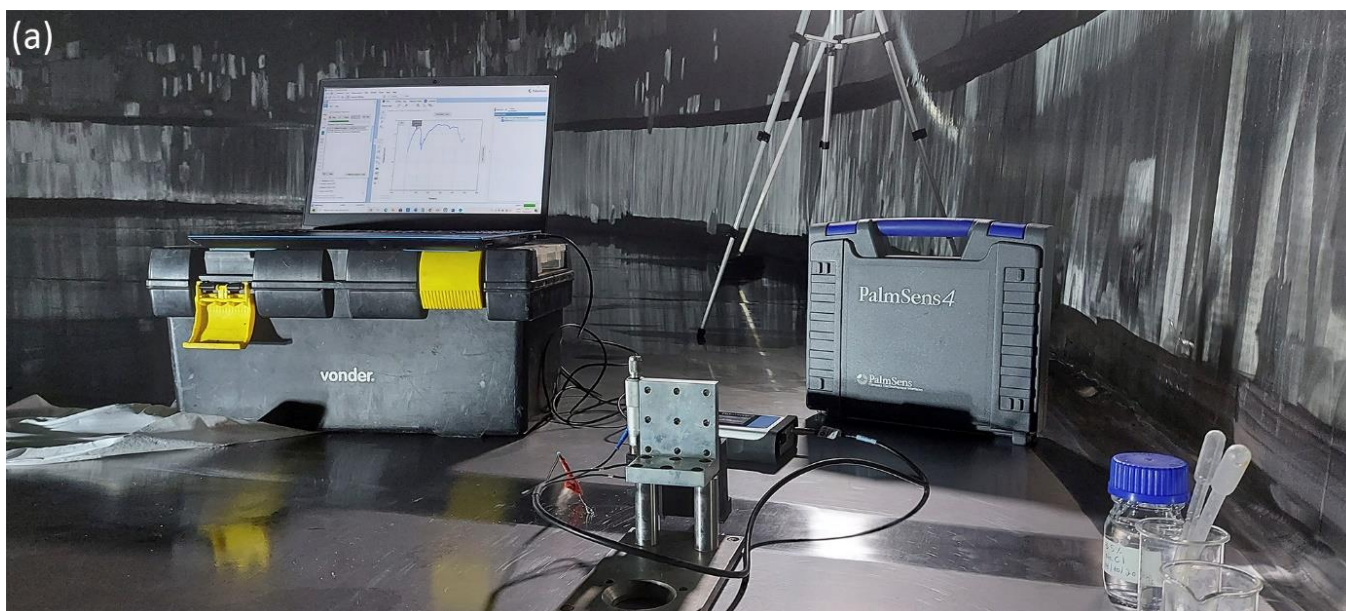
Figure 1. Construction site of the industrial cold chamber where it is showed the tanks. **(a)** In building process; **(b)** Internal face of tank showing the bottom plate and shell.

The welding of the tank parts was made using a semiautomatic tungsten inert gas (TIG) process (TIP TIG) by applying a double side synchronous welding technique, which means that two welders attack the joint simultaneously on opposite sides, and the maximum heat input was regulated as 2.5 kJ mm^{-1} to generate an appropriate weld metallurgy (Guilherme *et al.*, 2021c; Huang, 2015; Reccagni *et al.*, 2019; Wang *et al.*, 2021). The surface finishing was obtained by

mechanically grinding with an average surface roughness, $R_a < 0.76 \mu\text{m}$, and this parameter was controlled by a digital profilometer. After the surface finishing was concluded, a chemical treatment according to ASTM A-380 using a based nitric acid aqueous solution (12 v/v%) was performed to improve the passivation property of the inner surface of the tank.

The PassivityScan is a portable system capable of making electrochemical tests directly on the industrial site to evaluate equipment and facilities. It works as a typical three-electrodes microcell that was designed to be used in *on-site* inspection services (Guilherme *et al.*, 2019a). PassivityScan is robust and versatile to be used in all positions because its O-ring with diameter of 1.0 mm (scanned surface area is 0.008 cm^2) inserted on the bottom of the cell gets a well coupling with the surface, avoiding crevice corrosion, noise, or any external influence. The coupling of the microcell O-ring with the tank bottom surface can be seen in Fig. 2.

The construction site inspection management considered *on-site* electrochemical techniques in the Quality Control Inspection & Test Plan, and the aim was to assess the metallurgical integrity of welds by double loop electrochemical potentiokinetic reactivation technique (DL-EPR tests) and to certify the passivation level after chemical passivation treatment (by CPP tests), as described in Tab. 1.



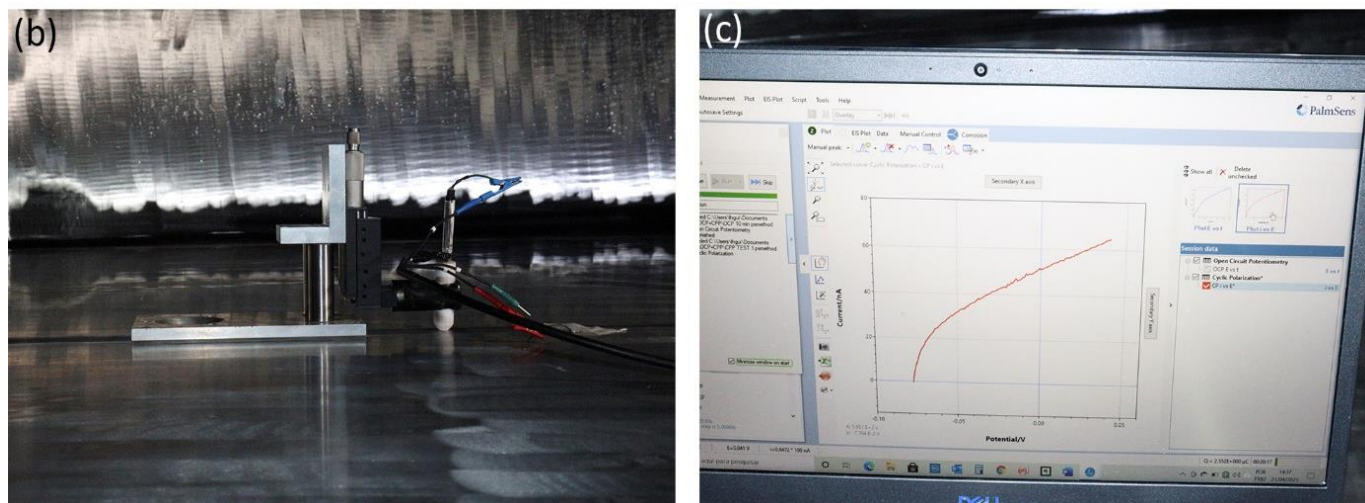


Figure 2. PassivityScan being used to measure the passivation level of the tank’s internal surface. (a) PassivityScan’s overview; (b) view of support and mini-cell; (c) Cyclic potentiodynamic polarization measurement on going.

Table 1. Goals of using PassivityScan in the integrity inspection and passivation.

Tank conditions	Objective	Technique	Performance parameters	Criteria
as built	metallurgical integrity of welds	on-site DL-EPR	i_a, i_r, Q_a, Q_r	DOS < 1
after chemical passivation (ASTM A-380)	passivation level	on-site cyclic polarization	$E_{corr}, E_{pit}, E_{prot}$ passivation level	$E_{prot} - E_{corr} > 350$ mV

The degree of sensitization criteria is based on the literature (Deng *et al.*, 2010). The passivation criterion is an empirical criterion.

The DL-EPR technique was applied to measure the degree of sensitization (DOS) on the weld regions, and, for that, the electrochemical potential was scanned first in the anodic direction, from -500 mV to $+300$ mV vs. Ag/AgCl/KCl 3 mol L^{-1} , where the polarization scan was reversed, and scanned back to -500 mV vs. Ag/AgCl/KCl 3 mol L^{-1} . A sweep rate of 1.67 mV s^{-1} was used for the tests. The criteria for the degree of sensitization consider the limit value to the DOS ratio of 1%, according to previous study (Deng *et al.*, 2010).

Cyclic potentiodynamic polarization tests were carried out to measure the passivation level integrity in view of ensure the passive film resistance at all over the surface (Guilherme *et al.*, 2019b), and the procedure was performed in 3.5% wt. NaCl solution to evaluate the pitting corrosion resistance. After stabilization of the open circuit potential (OCP) (~ 5 min), an anodic polarization scan was performed at a sweep rate of 1.67 mV s^{-1} . The anodic scan was reversed after it reaches one of the criteria: (i) current density of 1 mA cm^{-2} or (ii) potential of 1 V. Finally, the samples were scanned in the cathodic direction to a potential of -200 mV vs. OCP.

The passive region (or passivation level) takes into consideration the electrochemical parameters from the CPP curves in order to evaluate the resistance of the material to localized corrosion: $E_{corr}, E_{pit}, E_{prot}$. If E_{prot} is nobler than E_{corr} there is a potential range where the passive film is stable and no localized corrosion such as pits, crevice or crack initiation, will initiate or grow. The literature called this region as perfect passivity and the ASME BPE named it as passivation level, and the difference between $E_{prot} - E_{corr}$ indicates the amount of passivation level (ASME BPE, 2019; Esmailzadeh *et al.*, 2018). An empirical criterion for passivation level of 350 mV was determined.

The DL-EPR technique was tested at 90 surface points throughout 270 linear m of weld regions and the CPP technique was tested at 125 surface points on bottom plate and shell related to a total superficial area of 375 m^2 .

Table 1 describes the electrochemical techniques applied to assess the tank welds and surface and the respective performance parameters and criterion of acceptance. It is important to emphasize that DL-EPR technique was applied to assess the metallurgical features of welds and figure out if the weld region has

Cr-depleted zones, whereas CPP technique assessed the resistance of passive film. Bear this in mind, the criterion of acceptance to the DL-EPR was based on the literature (Deng *et al.*, 2010); nevertheless, there was not a established criterion of acceptance to the CPP technique and/or passivation level ($E_{\text{prot}}-E_{\text{corr}}$). Considering that it is important to have a minimum range of passive region in order to obtain a reliable material for engineering applications, it was empirically defined the criterion of acceptance of 350 mV.

3. Results and discussion

Figure 3 presents typical DL-EPR curves of the nonsensitized base metal and sensitized weld heat affected zone (HAZ) and their DOS values that were calculated using two different data: (i) activation and reactivation current densities (i_a and i_r) (Ebrahimi *et al.*, 2011; Hong *et al.*, 2013), and (ii) activation and reactivation charge densities (Q_a and Q_r) (ASTM G108, 2004).

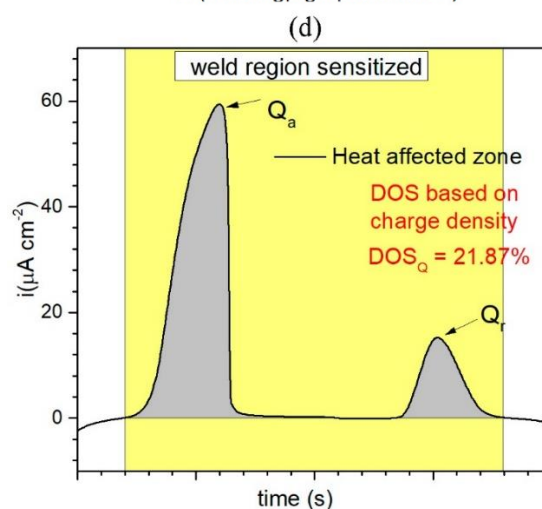
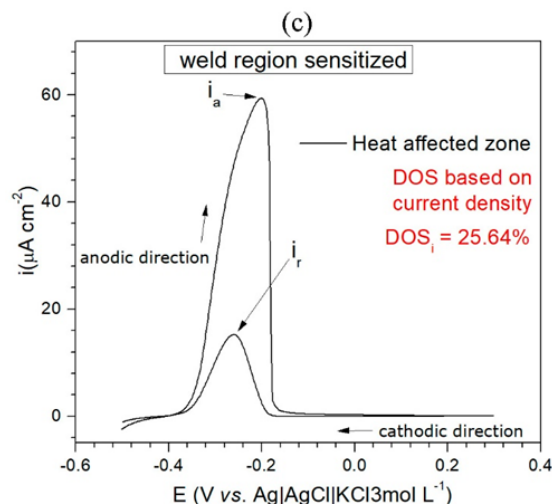
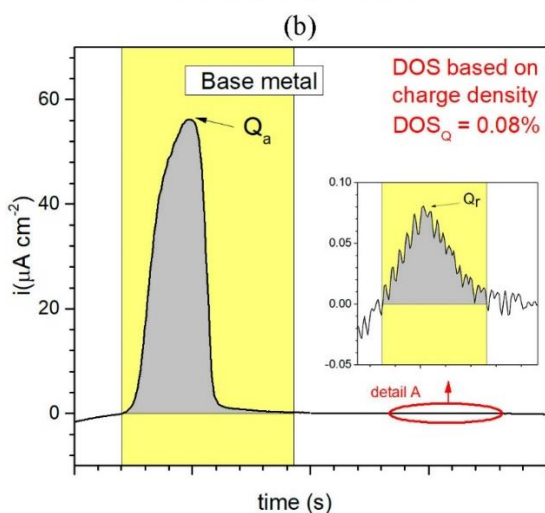
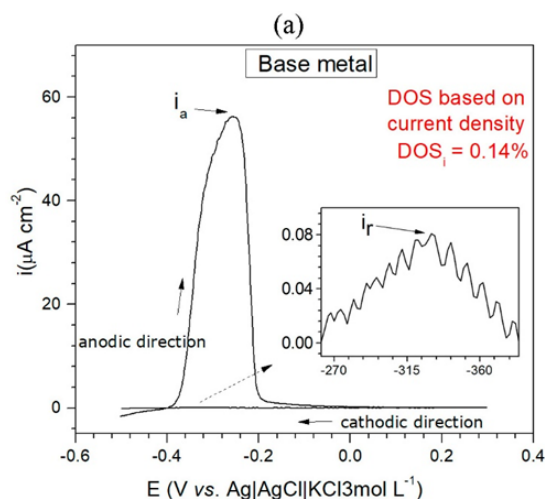


Figure 3. On-site DL-EPR curves calculating DOS based on current density [$(i_r/i_a) \times 100\%$] and charge density [$(Q_r/Q_a) \times 100\%$] to not sensitized base metal (a) $DOS_i = 0.14\%$; (b) $DOS_Q = 0.08\%$; and to heat affected zone of sensitized weld surface; (c) $DOS_i = 25.64\%$; (d) $DOS_Q = 21.87\%$.

First, the current of the reactivation peak (i_r) and the peak activation current density (i_a) were graphically determined using Origin v.9 software and the DOS was figured out as the ratio $(i_r/i_a) \times 100\%$. Second, the typical DOS curve (potential vs. current density) was converted into current density vs. time, following the charge determination by calculating the integrate of the gray area observed in Fig. 3b and d. It was done using integrate tool in Origin v.9 software and then the DOS was measured as the ratio $(Q_r/Q_a) \times 100\%$.

The degree of sensitization is a powerful criterion of acceptance to approve stainless steel tanks in manufacturing phase or maintenance projects, taking into account that it is extremely important to avoid operation fails caused by improper welding processes.

All the same, the DOS might be determined from the current density or the charge density, as shown in Fig. 3, and it was noted a soft difference between the DOS results. For practical applications, it is considered

the higher value in view of reducing the risk to failure. Table 2 illustrates how the results are shown in the metallurgical integrity report.

Table 2. *On-site* DL-EPR tests results.

Welded joint number	Surface site	DOS based in activation and reactivation current density			DOS based in activation and reactivation charge densities		
		i_r ($\mu\text{A cm}^{-2}$)	i_a ($\mu\text{A cm}^{-2}$)	DOS i_r/i_a (%)	Q_r (mC cm^{-2})	Q_a (mC cm^{-2})	DOS Q_r/Q_a (%)
base metal	base metal	0.08	56.23	0.14	3.21	3890.21	0.08
weld-01	weld	0.002	1.50	0.10	0.09	124.45	0.07
	fusion line	0.004	3.00	0.12	0.44	401.56	0.11
	HAZ	0.003	2.10	0.13	0.27	345.47	0.08
weld-18	weld	4.79	45.20	10.60 [#]	233.20	2486.15	9.38 [#]
	fusion line	15.23	59.40	25.64 [#]	874.40	3998.60	21.87 [#]
	HAZ	10.27	55.80	18.40 [#]	507.76	3254.87	15.60 [#]

[#]Inspected surface with DOS > 1 has submitted to the repair protocol.

It is to note that these *on-site* DL-EPR measurements were useful to optimize the parameters of the Welding Procedure Specification (WPS) to produce high-performance welds due to the welding energy control and consequently to obtain a microstructure free of sensitization (DOS < 1) (Hong *et al.*, 2013). After that, while the tanks were assembled, *on-site* DL-EPR tests were made to assess and control the compliance of the metallurgical integrity of the welded joints. Eight inspected areas in a total of 90 were reprovred based on the criteria of DOS ≤ 1, which represent a failed level of 8.9%. Each reprovred area was double-checked by field metallography performed after electrolytic etching using a 10% (w/v) oxalic acid aqueous solution to attack the microstructure. It was also observed the preferential corrosion attack of Cr-depleted regions around Cr-carbides and Cr-nitrides, which promote increased DL-EPR values, corroborating the *on-site* DL-EPR measurements (Guilherme *et al.*, 2019b). Figure 4 shows photomicrographs from sensitized surfaces obtained by field metallography, where the morphology of the Cr-depleted zones was noticed. All reprovred welds in the *on-site* DL-EPR inspection were submitted to the repair protocol.

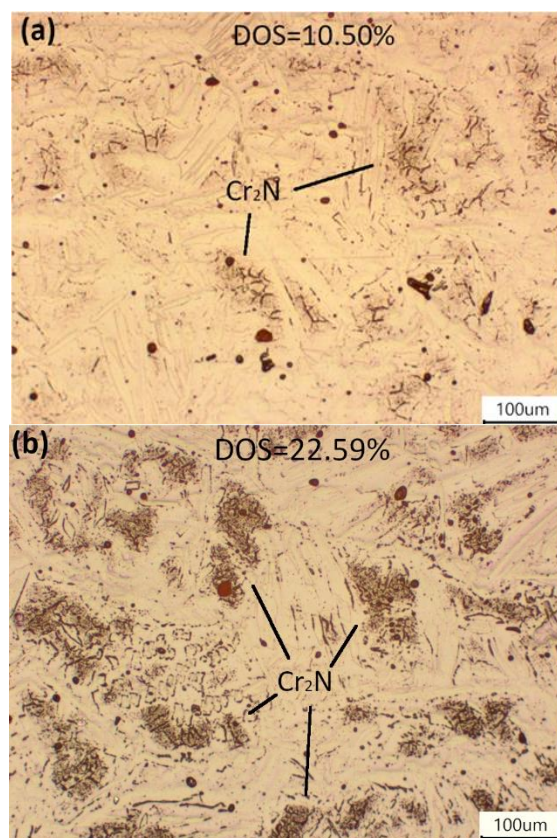


Figure 4. Field metallography of the sensitized surface with (a) DOS = 10.50% and (b) DOS = 22.59%. The Cr₂N regions were responsible for the high level of the degree of sensitization and these regions are highlighted in the figures.

Cyclic potentiodynamic polarization curves in 3.5 wt% NaCl solution are presented in Fig. 5. All CPP curves showed a passive behavior and the electrochemical parameters used to quantify the passivation level were corrosion potential (E_{corr}), pitting potential (E_{pit}), protection potential (E_{prot}), and the passivation level was calculated as $E_{\text{prot}} - E_{\text{corr}}$, which represents the *perfect* passive range (Kelly *et al.*, 2002). Figure 5a shows the CPP curves of the finished surface of as-built conditions (black curve), where a passive level of around 180 mV was obtained, and it is highlighted that the weld metal (blue curve) always had a higher performance due to the chemical composition of filler metal ER2209. In contrast, weld HAZ (red curve) showed the lowest performance due to the metallurgical features of this region. Figure 5b compares the passive film resistance between as-built condition (just mechanically polished) and chemical passivated surface (mechanically polished plus chemical treatment), with the latter achieving 4× superior performance (from 185 to 750 mV). It is important to highlight the passivation level obtained from as-built surfaces registered a pitting potential and presented a positive hysteresis after it, which means that the nucleated pits continued to grow until reaching the protection potential. On the other hand, the CPP measurements after chemical passivation treatment did not register a pitting or breakdown potential and demonstrated a negative hysteresis when the scan current density was reversed, which means that the passive film was not degraded by pitting corrosion in this test condition (Kelly *et al.*, 2002).

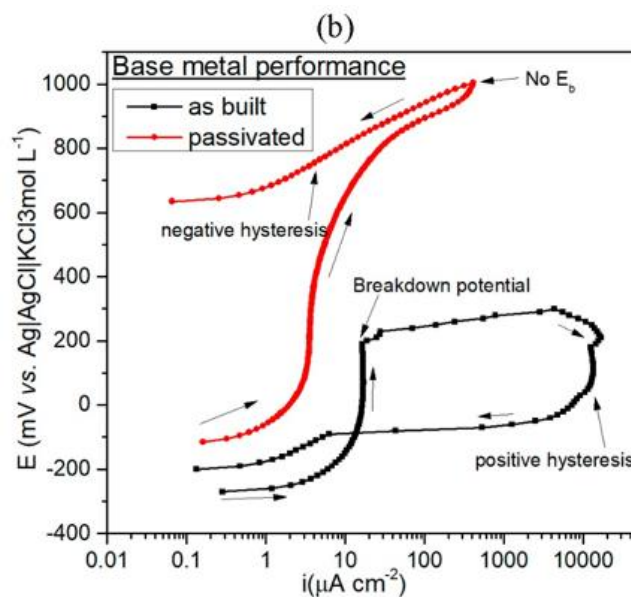
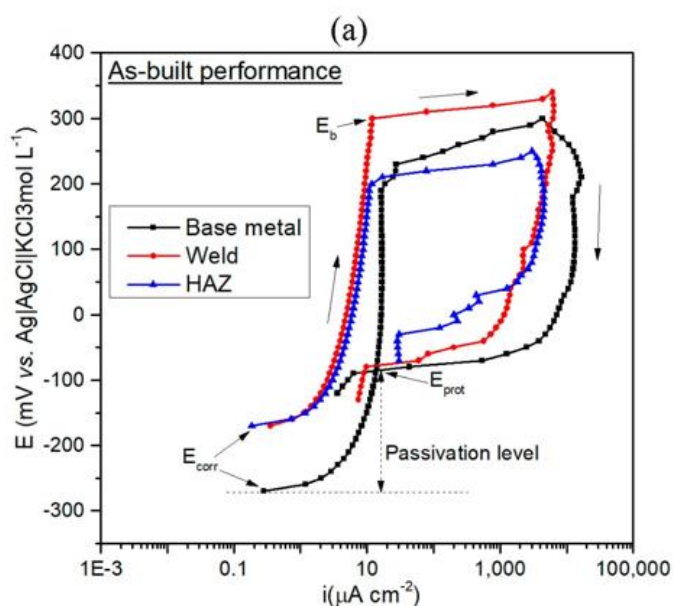


Figure 5. On-site cyclic polarization curves of (a) inspected regions such as base metal, weld metal, and heat affected zone and (b) comparison of performance between chemically passivated and not passivated surfaces.

The electrochemical parameters to assess the surface performance regarding passivation property are shown in Tab. 3 for the three life cycles of the tank: as-built, after chemical passivation treatment and after 12 uninterrupted months of operation. First, it is worth emphasizing that the as-built surfaces did not obtain satisfactory corrosion electrochemical parameters regarding the passivation properties. When compared to the passivated surface, the as-built surfaces demonstrated the lower corrosion potential and a premature pitting potential, which result in a low level of passivation based on the criteria $E_{\text{prot}} - E_{\text{corr}}$. The passivated surfaces shown the best performance in electrochemical corrosion tests with emphasis about the pitting potential: pit was not generated. It means that the passivated surfaces are more resistance than as-built surfaces against localized and pitting corrosion. The hypothesis is related to the complete removal of free iron on the surface after mechanical polishing, and the chemical passivation promotes the richer passive film in chromium (ASME BPE, 2019).

All the same, it is important to point out that in the most cases the manufactured tanks are included in the industrial process without chemical passivation treatment and it is a fault considering that the corrosion resistance and aseptic properties are significant increased by this treatment. In addition, the cost to apply the passivation treatment is inconsiderable when compared to the total investment in a new tank or the

cost to repair corrosion degradation. Finally, it was noted that after 12 months of operation the passivation properties were reduced when compared to the passivated surface, and it may be concerned to the

industrial environment that the tank works in term of cleaning solutions used to sterilize it, corrosive elements present in bioprocessing and biofilm formation.

Table 3. Passivation level assessment in different periods of the tank life cycle as built, after chemical passivation, and after 12 uninterrupted months of operation.

Construction phase	Inspection site	E_{corr} (mV)	E_{prot} (mV)	E_{pit} (mV)	Passivation level (mV)
As-built	base metal	-270	-85	+230	185
	weld metal	-170	-80	+300	90
	HAZ	-180	-30	+198	150
passivated surface (ASTM A-380)	base metal	-115	+635	+1000 ¹	750
	weld metal	+70	+680	+1000 ¹	610
	HAZ	+140	+660	+1000 ¹	520
after 12 months of operation	base metal	-185	91	+345	311
	weld metal	-130	204	+389	334
	HAZ	-169	128	+255	297

¹ $E_{pit}=1000$ mV indicates that stable pit nucleation and grow did not occur.

Looking at Fig. 5a, one may have the impression that different values of current density were used for the reversal of the scanning direction of potentials in the different regions of the weld. To clarify this, the readers are invited to see the Appendix.

4. Conclusions

The results from CPP measurements demonstrated that the surface finishing with $R_a = 0.76 \mu\text{m}$ had a passive behavior, and a low passivation level was obtained after polishing process. The surface chemical passivation treatment significantly increased the passivation level. The surface passivation level was reduced after 12 uninterrupted months of tank operation. The surface chemical passivation, applied according to ASTM A-380 restores the passivation level.

The *on-site* surface advanced inspection can be useful to reliability maintenance of managing the assets and facilities that operate in corrosive or aseptic processes. The application of the welding procedure specification permitted the obtention of a proper weld microstructure to be corrosive resistant and perform the weld quality control during tank manufacture. The CPP measurements gave the surface passivation level of the tank critical parts and qualify the compliance of the surface after chemical passivation treatment. These measurements also supported the assessment of the tank inner surface in contact with food grade product and allow demonstrating the passivation level decreased as a function of time. Bear it in mind, an acceptance criterion to passivation level was

determined for practical application, and this is an important data manage to the reliability maintenance. Based on passivation level parameter is defined the correct moment to restore the tank by chemical passivation treatment.

Authors' contribution

Conceptualization: Guilherme, L. H.; Benedetti, A. V.
Data curation: Guilherme, L. H.
Formal Analysis: Guilherme, L. H.
Funding acquisition: Guilherme, L. H.; Benedetti, A. V.
Investigation: Guilherme, L. H.
Methodology: Guilherme, L. H.; Fugivara, C. S.
Project administration: Guilherme, L. H.; Benedetti, A. V.
Resources: Guilherme, L. H.; Fugivara, C. S.
Software: Not applicable.
Supervision: Benedetti, A. V.
Validation: Guilherme, L. H.; Fugivara, C. S.; Benedetti, A. V.
Visualization: Guilherme, L. H.; Benedetti, A. V.
Writing – original draft: Guilherme, L. H.
Writing – review & editing: Guilherme, L. H.; Fugivara, C. S.; Benedetti, A. V.

Data availability statement

The data will be available upon request.

Funding

Fundação de Amparo à Pesquisa do Estado de São Paulo (FAPESP). Grant No: 2019/23063-4.

Acknowledgments

Not applicable.

References

- ASME BPE. *Bioprocessing Equipment*; 2019. [https://www.asme.org/codes-standards/find-codes-standards/bpe-bioprocessing-equipment-\(1\)](https://www.asme.org/codes-standards/find-codes-standards/bpe-bioprocessing-equipment-(1)) (accessed 2020-05-20).
- ASTM G-108 – 94 (Reapproved 2015): Standard Test Method for Electrochemical Reactivation (EPR) for Detecting Sensitization of AISI Type 304 and 304L Stainless Steels. <https://www.astm.org/g0108-94r15.html> (accessed 2021-10-12).
- Deng, B.; Jiang, Y.; Xu, J.; Sun, T.; Gao, J.; Zhang, L.; Zhang, W.; Li, J. Application of the Modified Electrochemical Potentiodynamic Reactivation Method to Detect Susceptibility to Intergranular Corrosion of a Newly Developed Lean Duplex Stainless Steel LDX2101. *Corros. Sci.* **2010**, *52* (3), 969–977. <https://doi.org/10.1016/j.corsci.2009.11.020>
- Ebrahimi, N.; Momeni M.; Moayed, M. H.; Davoodi, A. Correlation between critical pitting temperature and degree of sensitization on alloy 2205 duplex stainless steel. *Corros. Sci.* **2011**, *53* (2), 637–644. <https://doi.org/10.1016/j.corsci.2010.10.009>
- Esmailzadeh, S.; Aliofkhaezai, M.; Sarlak, H. Interpretation of Cyclic Potentiodynamic Polarization Test Results for Study of Corrosion Behavior of Metals: A Review. *Prot. Met. Phys. Chem. Surf.* **2018**, *54* (5), 976–989. <https://doi.org/10.1134/S207020511805026X>
- Guilherme, L. H.; Benedetti, A. V.; Fugivara, C. S. A Portable Electrochemical Microcell for Weld Inspection of Duplex Stainless Steel Tanks. *Corrosion.* **2019a**, *75* (4), 340–348. <https://doi.org/10.5006/3004>
- Guilherme, L. H.; Reccagni, P.; Benedetti, A. V.; Fugivara, C. S.; Engelberg, D. L. Corrosion Assessment of ASME Qualified Welding Procedures for Grade 2101 Lean Duplex Stainless Steel. *Corrosion.* **2019b**, *75* (10), 1216–1229. <https://doi.org/10.5006/3257>
- Guilherme, L. H.; Benedetti, A. V.; Fugivara, C. S.; Engelberg, D. L. On-Site Passivation Assessment of Type 316L Aseptic Storage Tanks with Electrochemical Techniques Luis Henrique Guilherme. In *21 International Corrosion Congress*; **2021a**. <https://www.proceedings.com/content/062/062828webtoc.pdf> (accessed 2021-05-12).
- Guilherme, L. H.; Benedetti, A. V.; Fugivara, C. S.; Engelberg, D. L. On-Site Cyclic Polarization Measurements to Validate Passivation Treated AISI 316L Stainless Steel in a Bio-Fermentation Tank. In *Eurocorr 2021*; **2021b**. <https://www.acwengenharia.com.br/article-at-the-european-corrosion-congress-eurocorr-onsite-passivation-assessment-by-cyclic-polarization/> (accessed 2021-11-25).
- Guilherme, L. H.; Fugivara, C. S.; Benedetti, A. V. Corrosion Monitoring of Grade 2101 Lean Duplex Stainless Steel ASME BPE Sanitary Tanks by On-Site Cyclic Polarization. In *32nd Canadian Materials Science Conference*; Kingston, Canada, **2021c**. <https://www.acwengenharia.com.br/corrosion-monitoring-of-grade-2101-lean-duplex-stainless-steel-asme-bpe-sanitary-tanks-by-on-site-cyclic-polarization/> (accessed 2021-03-11).
- Guilherme, L. H.; Fugivara, C. S.; Benedetti, A. V. Onsite DL-EPR Measurements and Field Metallography to Investigate the Localized Corrosion of 2101 Lean Duplex Stainless Steel Applied in Storage Tanks. In *32nd Canadian Materials Science Conference*; Kingston, Canada, **2021d**. <https://www.acwengenharia.com.br/onsite-dl-epr-measurements-and-field-metallography-to-investigate-the-localized-corrosion-of-2101-lean-duplex-stainless-steel-applied-in-storage-tanks/> (accessed 2021-10-18).
- Guilherme, L. H.; Benedetti, A. V.; Sadao, C. S.; Engelberg, D. L. Passivation Level of AISI 316L Aseptic Tank Surface Quantified by On-Site Electrochemical Techniques. *Mat. Res.* **2022**, *25* (Suppl 1), e20210623. <https://doi.org/10.1590/1980-5373-mr-2021-0623>
- Hong, J.; Han, D.; Tan, H.; Li, J.; Jiang, Y. Evaluation of aged duplex stainless steel UNS S32750 susceptibility to intergranular corrosion by optimized double loop electrochemical potentiokinetic reactivation method. *Corros. Sci.* **2013**, *68*, 249–255. <https://doi.org/10.1016/j.corsci.2012.11.024>
- Huang, J. X. The Double-sided Synchronous TIG Procedure and Matching Analysis of Corresponding Joint of X7Ni9 Steel. *Procedia Eng.* **2015**, *130*, 517–523. <https://doi.org/10.1016/j.proeng.2015.12.256>
- Kelly, R. G.; Scully, J. R.; Shoesmith, D. W.; Buchheit, R. G. *Electrochemical Techniques in Corrosion Science and Engineering*, Marcel Dekker, 2002. <https://doi.org/10.1201/9780203909133>
- Reccagni, P.; Guilherme, L. H.; Lu, Q.; Gittos, M. F.; Engelberg, D. L. Reduction of Austenite-Ferrite Galvanic Activity in the Heat-Affected Zone of a Gleeble-Simulated Grade 2205 Duplex Stainless Steel Weld. *Corros. Sci.* **2019**, *161*, 108198. <https://doi.org/10.1016/j.corsci.2019.108198>
- Wang, L.; Zhao, P.; Pan, J.; Tan, L.; Zhu, K. Investigation on microstructure and mechanical properties of double-sided synchronous TIP TIG arc butt welded duplex stainless steel. *Int. J. Adv. Manuf. Technol.* **2021**, *112* (1–2), 303–312. <https://doi.org/10.1007/s00170-020-06375-7>

Appendix

To clarify the current limit of 1 mA cm^{-2} , the curves were plotted as line+symbol and each symbol refers to individual measurements during the tests (Fig. A1). It is important to emphasize that the current limit was $1,000 \text{ mA cm}^{-2}$ (it corresponds to limit the current to $8 \text{ }\mu\text{A}$ in the data set of the PalmSens Pstrace software), however, when the sample reached and exceeded this value normally the material performance increased the current density a little bit more before beginning the decrease of current density. The green line represents the limit of the current density, and the circles show the last measurements before exceeding the limit.

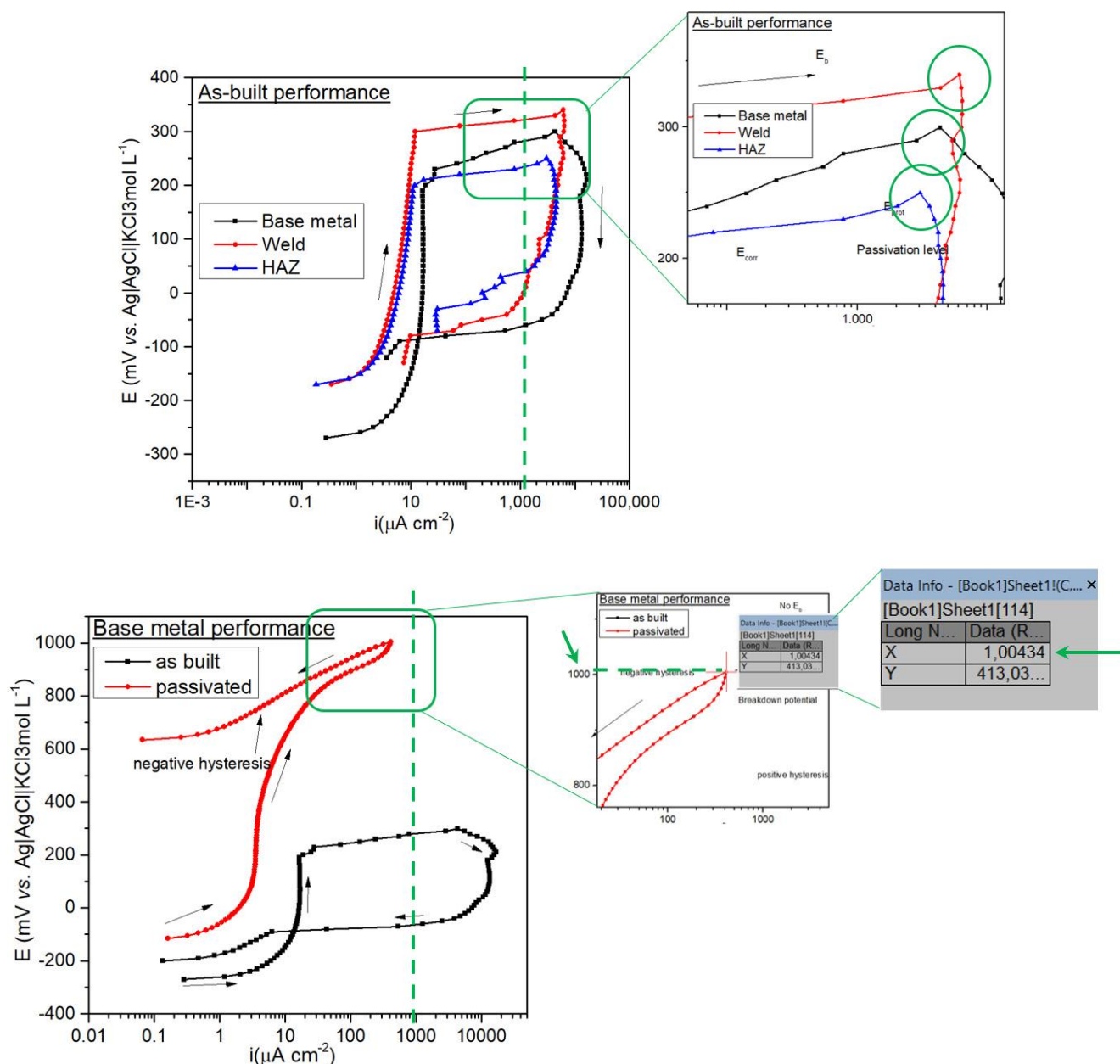


Figure A1. CPP curves showing the limit criterion to reverse the potential scan in current density of 1 mA cm^{-2} (attained before achieving 1 V) or potential of 1 V versus reference electrode (attained before achieving 1 mA cm^{-2}).

In Fig. A2 it is possible to observe the PalmSens Pstrace software screen where it is showed the CPP curve in axis of current vs. potential and in the left it is possible to see the current limit criterion (8 μA).

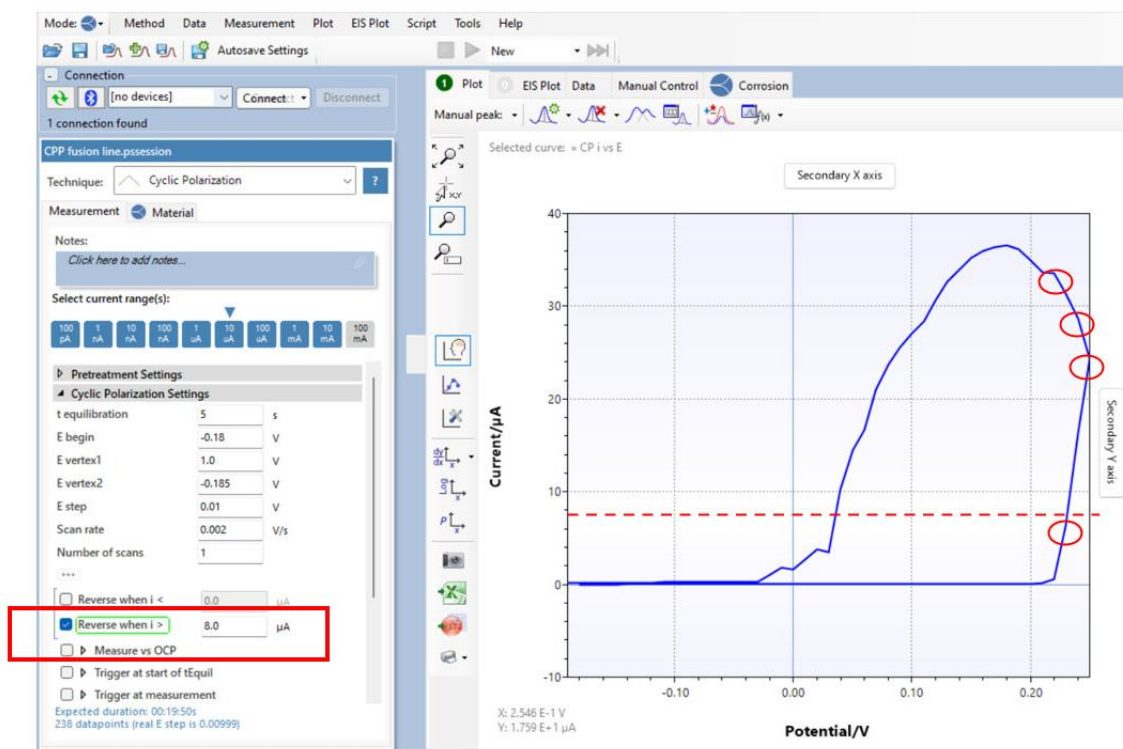


Figure A2. Cyclic polarization curve of fusion line showing a graphic of current (μA) vs. potential (V) where the scan is reversed at the first point exceeding 8 μA .